Spectroscopy and accurate spatial positioning of quantum emitters hosted by two-dimensional semiconductors

Artur Branny

Submitted for the degree of Doctor of Philosophy

Heriot-Watt University

School Engineering and Physical Sciences

Institute of Photonics and Quantum Sciences

January 2018

ABSTRACT

Atomically-thin semiconductors offer intriguing technological advantages for quantum photonic applications. Advantages include a lack of dangling bonds, atomically-precise interfaces, the potential to design novel heterostructures with an absence of nuclear spins, and the ease of integration with photonic integrated chip platforms. These benefits offer a new opportunity to construct a scalable quantum architecture with a coherent light-matter interface, an exciting prospect for future quantum technologies. This thesis takes the first steps in this direction.

Atomically-thin flakes of transition metal dichalcogenides (WSe_2 or $MoSe_2$) are transferred to substrates with smooth and nanopatterned regions. Using cryogenic microphotoluminesce spectroscopy, a correlation between isolated quantum emitters and localised strain 'pockets' is observed. This observation is exploited to fabricate WSe_2 arrays of highly pure single photon ($g^{(2)}(0)$ <0.5%) emitters at deterministic spatial positions (120±30 nm accuracy) with nearly 100% efficiency. The quantum emitters intrinsic optical properties are characterised via magnetic field and temperature dependent spectroscopy. The nanoscale strain engineering approach provides a universal scheme to create spatially and spectrally isolated quantum emitters in other two-dimensional materials. The thesis concludes with a discussion on the origin and dynamics of strain-tuned localized excitons in 2D semiconductors, presenting local disorder and exciton funnelling as important ingredients.

Keywords: two-dimensional semiconductors, spectroscopy, photoluminescence, single quantum emitter, quantum dots, nanoscale local strain engineering, site-control

To Agnes.

Acknowledgments

This work would not be possible without the support of my wife Agnes, my rock and true north. I would like to thank her for teaching me where and how to look for positives; how to best spend my energy; for lifting me up and keeping me on course; for being kind and caring; for being a part of this. You have seen it all. *Thank you* is beyond the scope of your input.

I would like to thank my supervisor Brian Gerardot for the eventful journey we went through together (both scientific and personal). I am grateful for your mentorship, support, honesty, sense of humour, hospitality, open-mindedness, presence and commitment which I never took for granted. Thank you for the opportunity, the challenge and for helping me become a better scientist.

Pals, I am grateful for all the time we have spent together, tough and fun. These moments tested and lifted me, all for a good reason. Thank you for letting me learn from you and be part of your story. Keep lunching, discussing, laughing, getting thirsty on Friday evenings and enjoying making science together. I bet our paths will cross again.

I would like to thank my office mates, especially Jack, for putting up with my constant slapping of doors and for numerous conversations. I will remember them fondly.

I would like to thank the Scottish Doctoral Training Centre in Condensed Matter Physics, especially Ian Galbraith, Patrik Öhberg, Chris Hooley, Julie Massey and Christine, for giving me the opportunity to be a member and providing me with the platform for enhanced experience as a young scientist. I am very grateful for the stimulating face-to-face meetings and events as they helped me connect and interact with other graduate students. I want to thank you for the ease of participating in international conferences, meeting collaborators and undertaking an industrial placement. These added another dimension to my journey, full of new mentors and inspiring people.

I would like to thank Bernhard Urbaszek and Gang Wang for the fruitful collaboration and for an amazing time in Toulouse. I've learnt a lot during my visit. I remember coming back inspired and excited. Thank you for being very supportive.

I would like to thank Andres Castellanos-Gomez for being the most open scientist I've ever met. Thank you for the invitation to Delft and for sharing with me your expertise in preparing 2D samples. The visit was a pivotal moment in my degree. Without it I wouldn't be where I am today.

DECLARATION STATEMENT

(Research Thesis Submission Form should be placed here)

Table of contents

List of Publications

[1] S. Kumar, A. Kaczmarczyk, B.D. Gerardot, Strain-Induced Spatial and Spectral Isolation of Quantum Emitters in Mono- and Bilayer WSe_2, Nano Letters, 15 (2015) 7567-7573.

[2] A. Branny, G. Wang, S. Kumar, C. Robert, B. Lassagne, X. Marie, B.D. Gerardot, B. Urbaszek, Discrete quantum dot like emitters in monolayer $MoSe_2$: Spatial mapping, magneto-optics, and charge tuning, Applied Physics Letters, 108 (2016) 142101.

[3] S. Kumar, M. Brotóns-Gisbert, R. Al-Khuzheyri, A. Branny, G. Ballesteros-Garcia, J.F. Sánchez-Royo, B.D. Gerardot, Resonant laser spectroscopy of localized excitons in monolayer WSe_2, Optica, 3 (2016) 882-886.

[4] A. Branny, S. Kumar, R. Proux, B.D. Gerardot, Deterministic strain-induced arrays of quantum emitters in a two-dimensional semiconductor, Nature Communications, 8 (2017) 15053.

Chapter 1 Introduction

1.1 Quantum light for quantum technologies

In this introductory chapter, I will explain how single photon sources can enable quantum technologies of the future. I will also present rationales behind the importance of seeking perfection in sources of single photons and spin-photon interfaces. Other topical reviews compliment this introduction section, such as those by Aharanovich, Englund and Toth[*1*]; Gao, Imamoglu, Bernien and Hanson[*2*]; and Senellart, Solomon and White[*3*].

Ever since the theoretical foundations of quantum mechanics were established throughout the 20th century, quantum physics has been making a progressive transition from thought experiments to applied science. Now, modern experimental physics is at the stage of harnessing the potential of quantum mechanics to imaging[*4*], sensing[*5*], communication[*6*] and information science[*7*] to develop new quantum technologies.

At the heart of these applications is a coherent superposition of states. For a two-level system such as the ground and excited states of an atom, the superposition is described by the wavefunction $|\Psi\rangle = a|\text{ground}\rangle + b|\text{excited}\rangle$, where $|a|^2$ and $|b|^2$ are the probabilities of measuring the atom in ground and excited state, respectively.

Such simple two-level quantum systems can be used as a bit of information, named a quantum bit (or qubit). While the classical computer stores and processes binary bits, 0 or 1, the quantum computer harnesses the superposition principle to increase the computational power. The principles of quantum mechanics offer another unique feature called quantum entanglement which is an instant correlation between the wave functions of two distinct quantum systems, e.g. $|\Psi_A\rangle$ and $|\Psi_B\rangle$. A famous example of fully entangled state is a Bell state $|\Phi^+\rangle_{AB} = \frac{1}{\sqrt{2}}(|00\rangle_{AB} + |11\rangle_{AB})$. To create an entangled state of two quantum systems, one must find an intrinsic or man-made process through which the correlation is established.

Photons, as undividable, elementary particles and single quanta play an important role in light-based quantum technologies enabling communication, metrology and networking. Traveling at the speed of light, photons are very well suited for these applications. Photons do not interact strongly with the environment in which they travel, maintaining their superposition and quantum correlations over long distances (unless absorbed). An example of this is the recent success in entangling photons over 1200 km using a satellite[*8*]. For the same reason, it is difficult to control photons, but still they can be entangled with a high fidelity using photonic gates[*9*]. When interfaced with another

quantum system (i.e. spin states in single atoms), photons offer a unique opportunity to preserve quantum information (i.e. in a spin coherence of an atom) for much longer times, so the qubit can be stored and processed. For this reason, a realistic quantum infrastructure is very likely to consist of stationary and flying qubits despite the fact that in principle single photons are sufficient for quantum computing. Therefore, the success of quantum infrastructure relies on development of a high quality interface between these two types of qubits[*2*]. While artificially engineered schemes to conduct the transition lack high efficiencies, solid-state SPSs offer unique and best solution for the interfacing spins with photons. In solid-state SPSs, the state of spin and the emitted photon are intrinsically entangled due to the intrinsic process through which photons are created, proving efficient channel for coherent exchange between them[*2*]. Therefore, solid-state SPSs are often referred as single quantum emitters (SQEs). Investigations of newly discovered solid state systems that host SPSs are partly motivated by the uniqueness of efficient and intrinsic spin-photon interface.

1.1.1 Quantum Computing

In the field of information science, quantum information processing (QIP) holds a promise of materialising a quantum computer which outperforms its classical counterpart. This includes the ability of solving problems which belong to the non-polynomial complexity class, such as factorising and searching random databases[*10*]. A quantum computer would also enable simulating systems which are quantum in nature[*11*]. The criteria for realising a quantum computer, (first specified by DiVincenzo)[*12*] are now very well known, yet the challenge of creating one still remains unconquered.

Due to the outstanding promise, there is an abundance of proposed architectures to accomplish quantum computing. Each architecture constitutes a highly technical field but all proposals have a common denominator - they implement a physical system to exploit qubits. Potential physical systems to realise qubits include single photons, quantised states of trapped atoms and ions; charge and flux quanta in superconducting circuits; spins and charges of self-assembled quantum dots and of quantum dots electrostatically-defined in a two-dimensional electron gas; impurities occurring in a wide band-gap solid-state. Each one has advantages but it is still unclear which candidate will solely accomplish the ultimate task. The likely scenario might involve building hybrid systems to accomplish a competitive quantum computer.

One approach to scalable quantum computing requires only photons, beamsplitters, and detectors. Linear optical quantum computing (LOQC), proposed by Knill, Laflamme and

Milburn, exploits photon teleportation to reach quantum gates with unity success rate[*13*]. In the scheme, logical operations are performed on single photons by projective measurements of photo-detection and manipulating optical elements including beam splitters, phase shifters, and half- and quarter-wave plates. While the architecture of LOQC enables the basic building blocks (i.e. CNOT gate), a practical quantum computer heavily depends on the scalability and the efficiencies of individual components. Therefore, in order to realise LOQC, there is an urgent need for developing sufficient quantum memories, photon detectors and single photon sources (SPS). In LOQC, high brightness of SPSs is required to ensure the information processing is done with high bit rates, compensating for practically unavoidable loses and errors introduced by optical components. The coherence time is also crucial for QIP because it limits the number of operations which can be performed on a qubit. To grant meaningful error correction, τ_c should be at least 10^4-10^5 times longer than a single processing task[*12*].

1.1.2 Quantum communication

Quantum communication provides the most secure way to communicate thanks to quantum key distribution (QKD), first proposed in 1984 by Bennett and Brassard[*14*] (the BB84 protocol). In QKD, any unwanted measurement on the state of propagating photon becomes detectable which prevents any eavesdroppers to interfere unnoticed. Photon-based systems utilising QKD are also the first commercially available quantum technology, partly because they do not require entanglement to be implemented. These commercial QKD systems use heavily attenuated laser beams and a decoy-state protocol[*15*].

The state of a single photon appears as a feasible and natural choice for transmitting quantum information over large distances. Optical fibre cables already span the world, allowing fast and high bandwidth communication. However, the finite coherence time of single photons and the non-cloning principle forbidding the construction of a practical quantum amplifier, imply the necessity for quantum repeaters to be used along the path of traveling photon in order to facilitate the communication over long, hundreds of kilometres distances. One of the suitable candidates for such quantum repeater is spin-photon interface, where the photon is absorbed and reemitted with renewed coherence[*16*].

Practical quantum communication shares with quantum computing the requirement for single photon repetition rate exceeding Giga counts per second[*1*]. Communicating over long distances with via optical fibres is always associated with attenuation, which is

minimum near telecom spectral windows at 1310 and 1550 nm. However, the majority of SPSs do not emit at these wavelengths. In order to be compatible with current fibre optics technology, single photons require to undergo a wavelength conversion via nonlinear wave-mixing techniques which in principle can be engineered to be 100% efficient[*17*]. The importance of brightness is prominent in QKD schemes where polarization of a photon is commonly used as a basis for the qubit. Some photon sources might be unpolarised, so 50% of photons are lost by introducing a linear polarizer.

1.2 A perfect single photon source

Because this thesis investigates two-dimensional semiconductors as newly emerging solid-state quantum photonic platform that host single photon sources, this section will describe a perfect single photon source followed by a brief review of other systems to generate single photon emission.

All light-based quantum technologies would benefit from better SPSs, but practical implementation require perfection. An ideal SPS emits a highly pure stream of single photons which are coherent and triggered on-demand with near unity efficiency. Further, in solid-state SPS, deterministic positioning is a key factor for scalability of the system. In the next subsections, the general figures-of-merit will be introduced.

Various systems can be compared against an overall quality factor $Q = \nu\ \eta\ [1 - g^{(2)}(0)] / \Gamma$, where ν is the visibility of two photon interference, η is the extraction efficiency, $[1 - g^{(2)}(0)]$ is the single photon purity, and Γ is the lifetime.

1.2.1 Brightness

The brightness is a combination of intrinsic properties of the SPS, such as quantum yield and lifetime, Γ, and experimental extraction and collection efficiencies, η. While the quantum yield specifies the effectiveness of triggering the single photon emission, the lifetime (Γ) defines the rate at which single photons are generated, which directly translates into the brightness.

The experimental efficiency (η) quantify how many photons in proportion to all generated photons arrive at the detectors after propagating through the optical system (i.e. collected by lenses, guided by optical fibres and waveguides). A common threat to η is the total internal reflection which occurs when a SPS is embedded in a high dielectric solid. To maximise brightness, one should also minimise the mismatch between spatial modes of the emission and the collection.

1.2.2 Purity

The purity of a SPS is defined as the probability of multiphoton emission, as measured by the second-order intensity correlation function, $g^{(2)}(\tau)$, and quantified by its normalized value at zero delay time, $g^{(2)}(0)$. $g^{(2)}(\tau)$ is commonly measured with Hanbury-Brown and Twiss (HBT) interferometer which originated from astronomy in 1956[*18*] but it is commonly used in quantum optics.

The interferometer includes two sensitive detectors separated by a small distance. Originally, the photomultiplier tubes were separated by a small distance and each measured the intensity of light coming from a distant star revealing a positive correlation in intensity between detectors. The correlation effects in intensities gave rise to a modern interpretation of the HBT interferometer, commonly used to determine whether a source of light emits single photons.

As the $g^{(2)}$ measures the correlation of intensity fluctuations, the time histogram also contains the information about the coherence of the correlations – the time beyond which the intensity fluctuations are uncorrelated. The characteristic time, T1 indicates the time it takes the emitter to send the next photon. The effect is widely known as anti-bunching effect and it was firstly demonstrated in 1977 with sodium atoms[*19*].

An HBT is shown in the Figure 1.2.1a. The light from the emitter is incident on a 50/50 beam splitter with a detector (SPAD) in each output arm. The detectors are labelled by a time correlator as "start" and "stop" trigger. The correlator builds a histogram of arrival times τ between the "start" and "stop" triggers. A histogram of the time delays for each correlated trigger represents the second order intensity correlation of the photon source $g^{(2)}(\tau)$, illustrated by Figure 1.2.1b where the curves were simulated using the formula (with fitting parameters specified in the caption):

$$g^{(2)}(\tau) = I_0\left(1 - \rho^2 e^{-\frac{|\tau - T_{delay}|}{T1}}\right)$$

Where I_0 is the background coincident counts, ρ is a fitting parameter related to the single photon purity and SBR = ρ/(1- ρ), T_{delay} is the time delay between "start" and "stop" triggers and T1 is the lifetime.

From the theoretical point of view, for a photon number state, $|n\rangle$ at τ=0, the $g^{(2)}(0)$ = 1-1/n. Therefore, a two photon state will generate $g^{(2)}(0)$ = 0.5, while single photon state $g^{(2)}(0)$ = 0. This implies that if the value of $g^{(2)}(0)$ lies below the 0.5 mark of the normalised histogram, the source emits anti-bunched single photons.

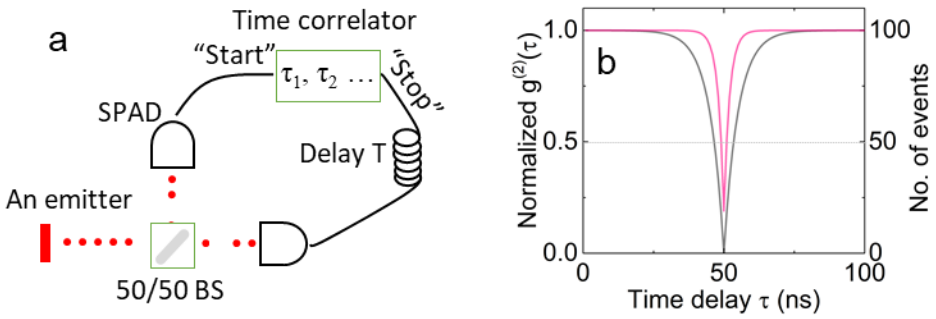

Figure 1.2.1 - **(a)** Schematics of the free-space HBT experiment performed on a SQE in order to confirm its quantum nature. **(b)** A theoretical simulation of $g^{(2)}(\tau)$ expected from a SQE after measuring time correlations with the setup from **a**. Both curves were computed with the formula $g^{(2)}(\tau) = I_0\left(1 - \rho^2 e^{-\frac{|\tau - T_{delay}|}{T1}}\right)$. The black curve represents a perfect single photon emission with T1 = 5 ns with almost background (ρ = 0.999) while the pink curve shows the background corresponding to ρ = 0.9 which has a shorter T1 = 2 ns. Both graphs were plotted with $I_0 = 100$ and $T_{delay} = 50$ ns.

In the literature, the normalized value of $g^{(2)}(0)$ is frequently quoted as the purity of a SPS where the constant uncorrelated background level of $g^{(2)}(\tau)$ is normalised to unity. For example, $g^{(2)}(0) = 0.01$ represents 99% single photon purity that is equal to 100-fold reduction in multiphoton emission. Essential purity levels vary from $g^{(2)}(0) < 0.01$ for QKD[*20*] to $g^{(2)}(0) < 0.001$ for all-optical quantum repeaters and cluster-state computing[*1*].

1.2.3 Indistinguishability and dephasing.

Indistinguishability of photons is commonly determined with a two-photon interferometer. First proposed by Hong-Ou-Mandel (HOM)[*21*]. When two particles meet at a 50/50 BS, there are 4 classical scenarios possible, as shown in Figure 1.2.2. However, if the particles are completely indistinguishable bosons, the scenarios 2 and 3 destructively interfere and only 1 and 4 remain. If, on the other hand, the photons are completely distinguishable, the destructive interference is negative and all 4 scenarios are equally likely. Then, photons bunched in pairs are detected at one BS output or the other with photodetectors and their $g^{(2)}(\tau)$ is measured in exactly same way as in HBT interferometer.

The visibility (ν) of the 2 photon interference characterises how indistinguishable the photons are. Under pulsed laser excitation the visibility, ν is defined as $[g^{(2)}_{\perp}(0) - g^{(2)}_{\parallel}(0)] / g^{(2)}_{\perp}(0)$, where $g^{(2)}_{\perp}(0)$ and $g^{(2)}_{\parallel}(0)$ are the integrated coincident counts of the peak at τ = 0 which is produced by two photons with orthogonal and parallel linear polarizations, respectively.

Unity visibility is a challenging goal to achieve for a SPS, but quantum applications demand almost perfection with indistinguishability as good as 0.99. However, some systems generating single photons do reach this benchmark.

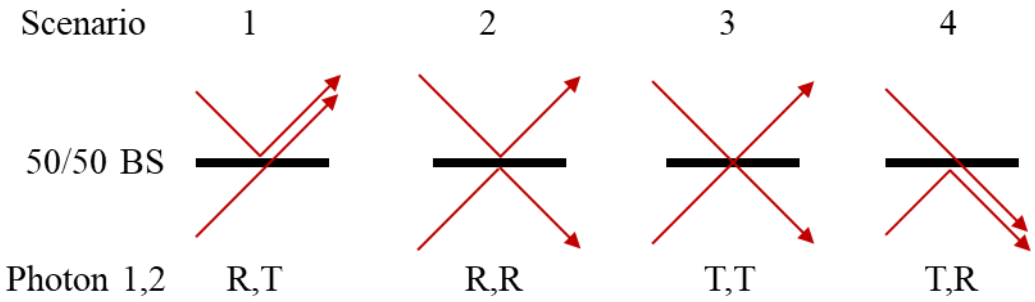

Figure 1.2.2 – Four classical possibilities of two-photon reflection (R) and transmission (T) in the Hong-Ou-Mandel interferometer.

1.3 A brief review on experimental realisation of single photon sources

In this section I will introduce a number approaches to obtain a SPS. For each, I will explain their working principle, the current state-of-the art, and their strengths and shortcomings.

Historically, the first demonstration of a SPS was from an atomic transition of sodium atom[*19*]. Since then the field dramatically progressed, expanded and diversified. Now, single photon sources can be divided into 3 categories. The first group gathers sources based on heralded photons created with a nonlinear medium. The second group consists of isolated single atoms, ions and molecules. The third group includes single quantum emitters (SQEs) from a very wide range of solid-state systems. The family includes fluorescent defects in bulk, colloidal and epitaxial quantum dots, and very recently, 2D materials.

1.3.1 Heralded photons

It was firstly demonstrated in 1988 by Ou and Mandel[*22*] that under high pump laser powers a nonlinear crystal (potassium dihydrogen phosphate, KDP) through spontaneous parametric down-conversion (SPDC) can yield single-pairs of entangled photons. Interestingly, photons generated via a nonlinear process inherit the long coherence from the pump laser.

The generation of heralded photons relies on optically transparent nonlinear crystals with a considerable second-order polarizability coefficient $\chi^{(2)}$, which ultimately is proportional to the single-photon yield. Although these nonlinear sources allow for high 70% collection efficiency (due to the lack of the total internal reflection), they are

intrinsically limited by low single-photon probabilities. Furthermore, in order to keep the levels of double-pairs sufficiently low the chances for single pair should be kept at below 0.1, usually at few per cents (if *p* is probability of single photon then probability of multi-photon scales as ~p^2). Nevertheless, high single-photon purity (up to 91%[*23*]) and HOM visibility (up to 92%[*24*]) are possible at relatively low brightness.

As $\chi^{(2)}$ is an intrinsic property, improvement lies in discovering or engineering new crystals, as has been achieved with periodically poled crystals (i.e. lithium niobate, potassium titanyl phosphate). Periodic polling not only increases the conversion efficiency but also can be optimised for a custom wavelength. However, on-demand generation is still a missing feature of heralded photon sources. Although a temporal and spatial multiplexing provides a nearly-deterministic trigger, this complex scheme provides losses due to switching, photon storage and detection.

1.3.2 Atoms and ions

In 1977, the first ever stream of single photons was demonstrated using resonant fluorescence from sodium atoms[*19*]. Cooled down to sub-Kelvin temperatures and trapped in magnetic-optical fields, atoms can reach their energetic ground state. In such conditions, an atom can be individually excited by absorbed laser energy and make a transition to higher energetic state. After a period of time, the atom spontaneously relaxes back to the ground state and emits a photon. This process is common for all solid-state SPSs where quantisation is an essential requirement. With the aid of a pulsed laser, the creation of single photons is easily achievable.

Trapped atoms have been demonstrated to be highly pure SPSs, with $g^{(2)}(0)$ as low as 0.0019[*25*]. Due to the absence of noise and dephasing mechanisms, the spin coherence times can extend to 0.5s[*26*]. The long coherence, combined with the high purity of single photons with near-identical wavepackets, provides a prominent interface between flying and stationary qubits.

However, it is challenging to collect all photons from a trapped atom, and collection efficiencies are typically ~1%. The issue of accessibility also hinders the possibility of applying external control gates, a crucial tool which is a huge advantage in single emitters immersed in a solid-state matrix.

Although, the experimental apparatus is bulky and complex, the work on trapped atom systems contributed greatly to the fundamental understanding of quantum phenomena. The level of control over the strength and the number of interactions between identical

atoms and long coherence times make this system an unprecedented testing playground of quantum mechanics and a great candidate for QIP to realise stationary qubits (i.e. quantum correction or quantum memory). Up to date, a small processor was built with a chain of single atoms and Shor factorising was successfully performed[*26*]. Although the path towards scalability remains unclear, the recent experiments constitutes another step forward towards quantum applications, reflecting how far the field progressed since its beginning in 1977.

1.3.3 Man-made artificial atoms - semiconductor epitaxial quantum dots

Man-made artificial atoms are microscopic islands of semiconducting material epitaxially grown in ultrahigh-vacuum chambers are self-assembled due to strain. Reducing dimensionality from 3D bulk to a 0D point-like island transforms the density of states, enhances excitonic effects, and increases Coulomb interactions due to the quantum confinement effect. A quantum dot traps electrons and holes, which can then be treated as a particle in a box exhibiting a spectrum of discrete levels like individual atoms. Together with the efficient light-matter interaction of a direct band-gap semiconductor, these well-defined quantised states facilitate the means for single photon generation.

Amongst all available single photon sources, QDs arguably have the best overall performance[*27*]. Indium-Gallium-Arnside QDs embedded in a Bragg mirror cavity and micropillar structure are intense sources with near lifetime-limited linewidths exhibiting near-unity purity and indistinguishability. To date, thanks to post-selection and nanofabrication around the chosen emitter photon extraction can be significantly improved, but the overall system efficiency remains low, at few percent[*28*] due to losses of inefficient detection, polarization extinction, optical coupling and transmission rate of optics. Despite this, QDs are the brightest of all solid-state SQEs providing 10 Mcps measured by the detector[*29*]. Further, the purities of 0.997 [*27*], robust indistinguishability of 0.9956 and on-demand triggering allowed for generating a steam of 1000 identical photons which led to an experimental demonstration of boson sampling[*30*].

To reach to this point from humble beginnings in 2000[*31*], the scientific community had to overcome many disadvantages. As emitters are embedded in a high dielectric environment the host presents challenges to efficient collection via total internal reflection. Fighting this obstacle requires an effort in designing and nanofabricating monolithic photonic structures such as waveguides or cavities around single emitters with

nanoscale precision, and with engineered radiation patterns to match modes of waveguides, optical fibres and objective numerical aperture (NA).

The nanofabrication is further challenged by the random distribution inherent to self-assembly that hinders its scalability and the inhomogeneous spectral broadening which stems from the growth method of QDs. Despite the above, it is entirely achievable to find and select a specific emitter to post-fabricate a customised structure to optimise the emitter's performance.

Another threat caused by the surrounding host is dephasing. The bulk environment contains residual electrons, magnetic isotopes and phonons which contributes to dephasing mechanisms via charge noise, interaction with fluctuating nuclear spin bath and phonon bath. To control and neutralize these effects, QDs are integrated into charge devices, optical cavities[*32*], are excited resonantly[*33*], subjected to magnetic fields[*34*], or the sequence of pulses[*35*]. This degree of tunability is a unique feature of solid-state systems. The level of control over the environment is best reflected by the experimental demonstration of QD emission with transform limited linewidths and coherence times exceeding few μs[*36, 37*].

1.3.4 Fluorescent defects in crystals

Point defects constitute a single or combination of impurities such as a foreign atom, an interstitial or a vacancy. Single impurities create tightly localised potential perturbations and if their energy lies sufficiently deep within the bandgap of the host crystal, they can trap excitons. In such cases, an exciton tapped in a point defect develops quantised levels, the required ingredient for single photon generation.

The library of defects and their hosts is extensive and diverse. It comprises of colour centres in wide-bandgap crystals such as diamond, silicon carbide (SiC), Zinc oxide (ZnO) and rare-earth-ion impurities in yttrium aluminium garnet (YAG). Introducing all defects with their characteristics lies beyond the scope of the thesis, thus this brief overview will focus on the most studied colour centres in diamond because they were first to demonstrate basic building blocks of quantum networks. In particular, the negatively charged nitrogen vacancy (NV^-) has been used to entangle spin and photon, the NV centre and nearby nuclear spins and two remote NV centres. For information on other hosts and their defects the following review is recommended[*1*].

The success of point defects relies on the intrinsic crystallographic and electronic structure, which defines the qubit all optical properties and the susceptibility to

environmental noise. In diamond, the search for new types of defects continues as a defect with the desirable configuration is yet to be found where long spin coherence would co-exist alongside excellent optical properties. For instance, in NV^-, significant spectral diffusion and only a small fraction (4%[*38*]) of light at the zero-phonon line (ZPL) are serious drawbacks. The negatively charged silicon vacancies (SiV^-) with intrinsic inversion symmetry show significant optical improvements with minimal spectral diffusion and 70% of photons emitting into the ZPL. However, its coherence is jeopardized by electron-phonon coupling and limited to 38 ns at 4K, which can be extended to 10 ms only by cooling the sample to extreme 100 mK[*39*], but still it cannot compete with 1.8 ms coherences of NV- seen at room temperature[*40*]. Such long coherences were possible in NV^- only via isotopic purification of the host crystal which controlled the level of decoherence and its sources. Thanks to dynamical decoupling scheme the coherence can be further lengthened to up to 0.6s (at 77 K)[*41*]. On the other hand, introducing impurities engineers and pins the Fermi energy to the artificial level to access other charge states, such as neutral silicon vacancy SiV^0 which was found to combine excellent optical properties of SiV^- and long coherences of NV^- [*42*] reaching coherence times of 250 ms at 15K. Further, on-demand defect implantation enables deterministic positioning that allows for scaling up this quantum photonic platform[*43*].

Amongst all solid-state SQEs, colour centres possess the best spin coherence and generate light with lifetime-limited linewidths. However, even at 5K two-photon interference show dissatisfactory visibilities of 66% and 72% for NV^- and SiV^- respectively. Furthermore, colour centres do not belong to the brightest due to low quantum efficiencies of the defects and the total internal reflection hinders brightness providing maximum count rates of ~2 Mcps for NV^- [*44*], ~6 Mcps for SiV^- [*45*] and 10 kcps for SiV^0 [*42*]. Finally, the single photon purities of colour centres lag behind relative to their quantum counterparts achieving values of $g^{(2)}(0)_{NV^-} = 0.09$ and $g^{(2)}(0)_{SiV^-} = 0.04$ [*46*].

Overall, colour centres offer unique opportunities to exploit the extraordinary long coherence in quantum memory applications. Their shortcomings in optical excellence drive the field to develop ground-breaking techniques to engineer the host composition, to screen adverse environmental influence with complex pulse sequences all of which forges the road map for other quantum photonic platforms. Finally, exploration of entirely new point defects (i.e. germanium or tin vacancy centres) persists to encase all desirable features into a single defect to realise a sufficient SQE for practical QIP applications.

1.3.5 Two-dimensional materials

Since the inauguration of two-dimensional (2D) materials marked by the isolation of graphene in 2004[*47*], the 2D family has been growing in numbers, and now offers a diverse and complete portfolio of materials ranging from metals, superconductors, semiconductors and wide-bandgap insulators. Recently, 2D materials has joined other quantum photonic platforms as a result of hosting SQEs and displaying unique properties. To date, a few 2D crystals were shown to host SQEs. This includes semiconducting tungsten diselenide (WSe_2)[*48-53*], tungsten disulphide (WS_2)[*54*], wide-bandgap hexagonal boron nitride (hBN)[*55-61*], and GaSe[*62, 63*]. $MoSe_2$[*64, 65*] and InSe[*66*] show sharp QD-like emissions, but single photon emission still requires to be confirmed.

Similar to fluorescent defects in crystals, each 2D host presents distinct electronic dispersion which should underpin emitter optical properties. Once again, also in this brief overview, the focus is intentionally limited to the most studied monolayer of WSe_2. In contrary to emitters in hBN which were ascribed to deep states inside the bandgap, the origin of SQEs in other 2D hosts is yet to be explained but it was vaguely associated with localized, weakly bound excitons.

Typical quantum emitters from WSe_2 exhibit sub-100 μeV linewidths with few nanosecond lifetimes. Further research is needed to investigate the mechanisms responsible for the inhomogeneous broadening. These emitters can be found at flake interfaces or edges[*48, 50*] or at local strain pockets due to flake wrinkling, folding or bubbling[*51, 53, 67, 68*]. Despite this, the most frequently found isotopes of W, Mo, S and Se atoms have zero magnetic moment which should be beneficial for preserving long spin coherences. It has been also demonstrated that quantum emitters in WSe_2 can generate count rates of ~3Mcps and have high level of single photon purities with $g^{(2)}(0)$ as low as 0.002[*69*], comparable with the best results of single atoms.

What makes this emerging quantum platform exciting and intriguing are the unique features of the 2D host. First, the fabrication process facilitates an easy manipulation of 2D sheets which paves the way for integration with photonic waveguides, cavities, charge and strain devices. Moreover, the occurrence of SQEs on fully exposed surfaces eliminates total internal reflection (which hinders other solid-state SQEs in bulk) which can lead to very high extraction efficiencies and high tunability thanks to a direct and uninterrupted access to the emitters. High tenability also stems from extraordinary intrinsic properties like high resistance to strain (WSe_2 monolayer can withstand 11% of strain before it fractures[*70*]). Another example of 2D crystals being place of extremes

arises from large 2D confinement which creates very strong Coulomb interactions. This combined with large effective masses and reduced dielectric screening lead to large exciton binding energies of the order of 0.5 eV[*71*] and small Bohr radii (< 1 nm)[*72*]. In addition, the hexagonal Brillouin zone and the large spin-orbit coupling of WSe_2 unique to this material foster optically accessible spin valley degree of freedom which, if preserved in a quantum emitter, would provide a coherent spin-photon interface.

The overall prospects of SQEs hosted by 2D crystals is yet to be fully established. Frequently asked questions concern the nature of SQEs in TMDs and the impact of 3D confinement on the quantum emitter properties (i.e. spin-orbit coupling, valley hybridization), all of which might be linked to the symmetry of the confinement and underlying crystal lattice. For now, the optical properties suffer from relatively large spectral jitter, likely due to environmental noise, and an obvious course of research might involve improving the quality of the 'mother' crystal or encapsulating monolayers in other 2D crystals.

The single emitters in WSe_2 and $MoSe_2$ are in the spotlight of this thesis. Therefore, the next section will describe two-dimensional transition metal dichalcogenides (TMDs) in more detail.

1.4 Introducing 2D TMDs

1.4.1 A brief history

Owing to its extraordinary properties, graphene offered many opportunities for fundamental research, leading to an exponential growth of research articles involving graphene and recognition by the Nobel Prize committee in 2010. What graphene does not offer is an optical bandgap. While efforts to open the bandgap artificially led to limited success, the lack of a fundamental gap forbade graphene to make an impact in optoelectronics.

This encouraged researchers to explore semiconducting layered crystals where optical bandgaps occur naturally. Monolayer molybdenum disulphide (MoS_2) became first atomically thin direct-gapped material[*73*] to show strong absorption and bright photoluminescence, opening the doors of optoelectronics (i.e. diodes, photodetectors, photovoltaic applications) to van der Waals crystals. The discovery also introduced transition metal dichalcogenides (TMDs) as a group within 2D family. Now, the catalogue of 2D semiconductor bandgaps collectively covers very wide spectral range from ultra violet with hBN through visible with InSe-like crystals, infrared with Mo and

W based TMDs, telecom wavelengths with black phosphorus (bP) and reaching few-micrometre region with almost closed bandgaps of silicene and germanene[*74*]. Although the scientific interest of black phosphorus and hBN is growing rapidly, MoS_2 and its close derivatives (i.e. $MoSe_2$, WSe_2, WS_2) remain the most studied 2D semiconductors.

There is hope that 2D semiconductors with such diversity and capacity of being assembled into 2D heterostructures will have a disruptive impact on the current technology, but fundamental questions remain to be addressed. Nevertheless, 2D semiconductors present new physical phenomena which might fulfil technological promises.

The following sections will introduce the fundamental and unique to TMDs physical phenomena that drives an scientific curiosity, which are also gathered in a comprehensive review on the excitons in atomically thin TMDs[*75*]. I will first introduce the crystallographic structure of TMDs as, in line with Neumann's principle, it underpins all properties (including optical) of the material.

"*The symmetry elements of any physical property of a crystal must include the symmetry elements of the point group of the crystal*" Franz Neumann

1.4.2 Crystallographic structure

Transition metal dichalcogenides are described by the formula MX_2, where M is a metal atom from groups IV (Ti,Zr and so on), V (Nb, Ta and so on) or VI (Mo, W and so on) and X is a chalcogen atom (S, Se or Te). Their free electrons facilitate and contribute to chemical bonds which produce layered crystalline structure. The structure of each single layer takes the form of 3 hexagonal sub-lattice planes, where the metal plane is encased between two planes of chalcogen atoms, like X-M-X. All bonds within each single layer are satisfied. This connects atoms by strong covalent bonds and effectively eliminates any out of plane dangling bonds. The bulk crystal is made from stacks of single layers, bonded via weak van der Waals attraction. Without violating the chemical formula, the bulk crystal can have a distinct symmetry due to stacking order and metal-chalcogen coordination. The symmetry defines how many layers fit into a unit cell. Let's consider three structural polytypes:

polytype	overall crystal symmetry	# of layers per unit cell	coordination
1T	tetragonal	1	octahedral
2H prismatic	hexagonal	2	trigonal
3R prismatic	rhombohedral	3	trigonal

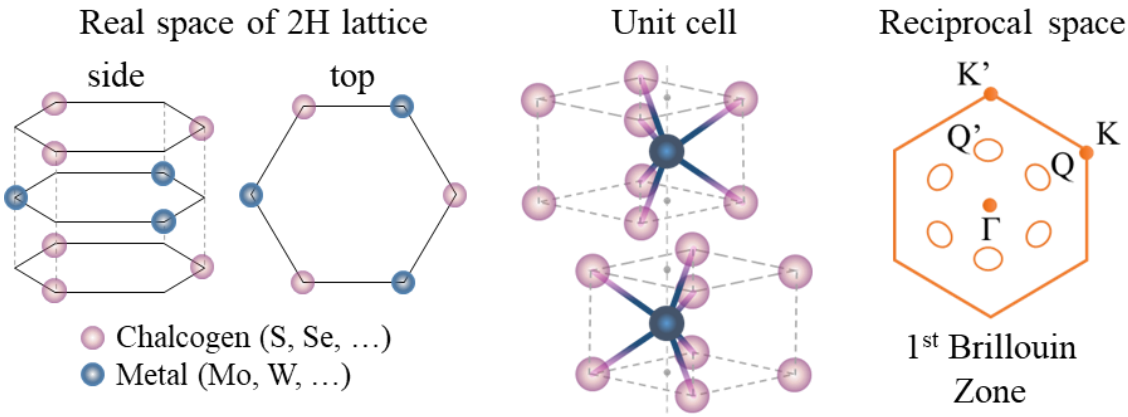

Figure 1.4.1 – As labelled, (left) lattice in 2H phase with hexagonal C_3 symmetry. (middle) Unit cell of 2H phase containing two layers which restore in-plane inversion symmetry while a single layer violates it. (right) Reciprocal lattice showing first Brillouin zone with marked high symmetry points [71].

This thesis presents results on TMDs with the 2H polytype only. This lattice has hexagonal and rotational C_3 in-plane symmetries but it simultaneously breaks the inversion symmetry, as shown in Figure 1.4.1. For the stacking that follows the ABAB sequence, the inversion symmetry, however, is restored for stacks with an even number of layers because ABAB has out-of-plane mirror symmetry (Figure 1.4.1). Adhering to Neumann's principle indicates that violation of the in-plane inversion symmetry opens a path for anisotropic physics. For optical properties this leads to strong nonlinear optics including second harmonic generation (SHG) and two-photon absorption. However, in TMDs, the most unique consequence of breaking the inversion symmetry is the valley dependent optical selection rules. In order to arise, these selection rules also require a few other conditions which in fact are met by intriguing electronic properties of TMDs, which will be described in the next section.

1.4.3 Electronic dispersion and optical properties

The hexagonal lattice of the 2H polytype produces a Brillouin zone with the same hexagonal symmetry which consists of 4 distinct symmetry points noted by K, K', Γ and Q[*76*], conventionally called sigma point, as shown in Figure 1.4.1. For the bulk, the electronic dispersion accommodates a near infrared-wide bandgap at Q symmetry points, between 1.1-1.4 eV for Mo and W based TMDs. As the material gets thinner, the band at

Q is lifted, while at K and K' the bands remain intact. As a result, as Figure 1.4.2 displays, at the single layer limit the difference between bands (Δ_{KQ}) switches its sign so the lowest energy gap changes to K and K', turning the monolayer into a direct semiconductor[*77*]. The transition from indirect to direct semiconductor occurs between bilayer and monolayer which is manifested by 3 order of magnitude increase in PL intensity[*73*, *78*].

Another consequence of reducing the number of layers is the quantum confinement effect which forces excitons to share limited amount of 2D space enhancing the strength of Coulomb interactions. Coulomb interactions are also aided by the heavy effective masses due to the Mo and W *d* orbitals and by significantly reduced dielectric screening from other charges which otherwise would be present in the bulk. As a result, 2D excitons in monolayers increase their PL emission energy to 1.7 - 2.1 eV (for Mo and W based TMDs monolayers) and their binding energy is ~0.5 eV[*79*], which is an order of magnitude larger than in bulk semiconductor quantum wells[*80*] and enables 2D excitons to be seen at room temperatures. Another outcome of large Coulomb interactions is the formation

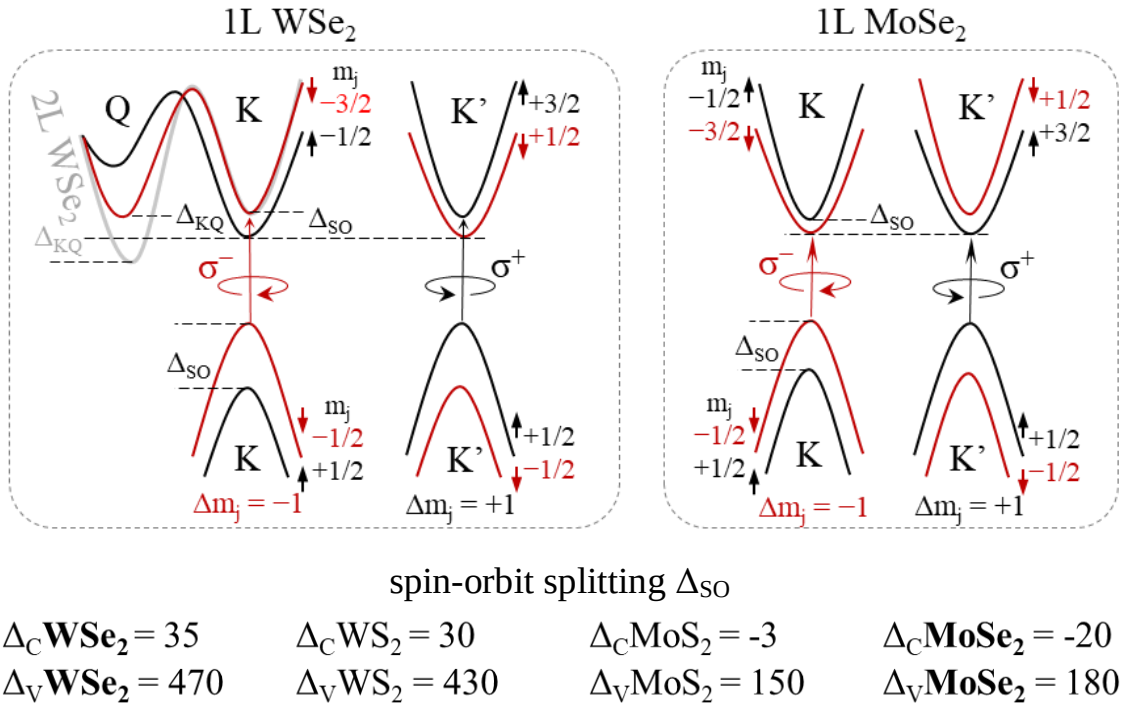

spin-orbit splitting Δ_{SO}

Δ_C**WSe$_2$** = 35	Δ_CWS$_2$ = 30	Δ_CMoS$_2$ = -3	Δ_C**MoSe$_2$** = -20
Δ_V**WSe$_2$** = 470	Δ_VWS$_2$ = 430	Δ_VMoS$_2$ = 150	Δ_V**MoSe$_2$** = 180

Figure 1.4.2 – Illustration represents single particle dispersion (left) of WSe_2 and (right) $MoSe_2$ monolayers. Bands are labelled with high symmetry points (K,K',Q) which correspond to the 1st Brillouin zone, spin-orbit splitting Δ_{SO}, color-coded spin orientation, its vertical projection of total angular momentum, m_j. Optical selection rules for exciting spin-valley degree of freedom ($\Delta m_j = \pm 1$) is also color-coded [83]. Marked in grey is the band of bilayer WSe_2 where the energy minimum is at Q creating indirect bandgap (1L Δ_{KQ} = 0 – 80 meV, 2L Δ_{KQ} = 110 meV). (below) A summary of Δ_{SO} magnitudes for Mo and W based TMDs where all values are in meV and C (V) stands for conduction (valence) band. Pictures were hand-drawn and inspired by [77].

of excited state quasiparticles, trions[*81*] and biexcitons[*82*] which are also tightly bounded with their own binding energies of tens of meV (trion MoS_2 20 meV[*81*], trion $MoSe_2$ 31 meV, trion WSe_2 33 meV and biexciton WSe_2 52 meV[*82*]).

Strong Coulomb interactions and its consequences (i.e. large binding energies) will have a direct impact on the 3D confinement properties of localized excitons and their optical properties, some which remain to be understood. They will be presented in Chapter 4, Properties of WSe_2 SQEs.

In addition to strong Coulomb interactions, the presence of heavy metal atoms (Mo, W) with *d* orbitals leads to strong spin-orbit coupling which splits both the conduction and valence bands into two at K symmetry points. This produces a gap in the conduction (valence) band at a few to tens of meV (few hundred meV) which varies amongst TMDs. Figure 1.4.2 summarises the magnitude of the splitting and marks bands in which degeneracy is lifted with Δ_{SO}. The sign of Δ_{SO} also depends on the material; Mo based TMDs experience negative and small Δ_{SO} while in W-based the sign is positive with relatively large gaps.

As long as the bands are equivalent, the splitting and its sign does not impact the optical properties. However, in monolayer, the broken inversion symmetry forces the bands to become spin-dependent. In this case, the sign of the splitting becomes of great importance because the optical transition is only allowed if its difference of the z-component in the total angular momentum, m_j gives integer number. Therefore, the sign of Δ_{SO} defines whether the monolayer's ground state is allowed (bright in $MoSe_2$) or forbidden (dark in WSe_2) transition [*83*]. Originating as a consequence of numerous, simultaneously and naturally occurring factors, the spin-dependent optical selection rules is a very unique and rather lucky feature of 2D TMDs. This feature is often called the spin-valley degree of freedom which will be explained in more detail in the following section.

1.4.4 Spin-valley degree of freedom

The spin-dependent optical selection rules concern bands at the edges of the Brillouin zone, at K and K' points where the gap is the smallest. Bands at these points are referred to as K and K' valleys which are connected by time-reversal symmetry, are degenerate in energy but unequal in momentum creating three equivalent pairs, as shown in Figure 1.4.1. Momentum is not preserved due to the breaking of in-plane inversion symmetry. Further, the strong spin-orbit coupling coherently binds the spin of the photogenerated carrier with the valley creating spin-valley optical rules which are distinguished by two

colours in Figure 1.4.2. Therefore, in optical terms, as Figure 1.4.2 shows, light with orthogonal (left σ^-, right σ^+) circular polarisations only couples to relevant, K' and K valleys. It has been demonstrated that spin-up (-down) in K (K') valley can be optically addressed with 100% efficiency while coherent superposition of both valleys can be achieved with linearly polarized light[*84-87*].

These optically addressable and coherently manipulated transitions serve as additional degree of freedom and remain relevant for all quasiparticles like the trion of which there is no analogue in conventional semiconductors. There is a theoretical prediction[*88*] that spin-valley degree of freedom becomes hybridised in 3D confined exciton. Despite this the prediction also anticipates a 3-level Λ-type scheme which facilitates a qubit state that can be optically initialised, readout and manipulated. This paving the way for valleytronics to be used in QIP, which is one of the main drivers for investigating SQEs in atomically thin TMDs.

1.4.5 Screening effects

Although screening effects are not directly studied in this thesis they should be always considered as they influence all 2D semiconductor samples. Perhaps the best example supporting the notion that the surroundings of the monolayer directly influence its fundamental properties are the large discrepancies in the values of 2D exciton binding energy even after being measured and calculated a number of times. Discussion about the reasons for these differences is technical but is well captured by Wang *et al.*[*75*]. However, the reason which speaks to me the most is that small Bohr radii (of order of 1nm) of the exciton ground-state produce wavefunctions that exceed several times the lattice constant a_0 (for WSe_2 $a_0 = 0.33$ nm) extending over to the surroundings which can cause the departure of exciton energy ladder from the hydrogenic series. Therefore, this feature offers the opportunity to engineer the properties of monolayers by engineering the screening environment in the proximity[*89*]. For instance, encapsulating semiconducting monolayers in high quality hBN has shown to significantly improve linewidths of exciton emission towards the homogenous limit[*90*] perhaps having analogous effect on SQEs linewidths. Further, one could envisage artificial screening landscape as a lattice of point-like perturbations which introduce another degree of confinement with sufficient magnitude to trap excitons and quantise their energy spectrum.

1.4.6 Mechanical properties

In the context of SQEs, tunebility is a very tangible and desired feature, for example, to modify optical properties of an emitter in order to match the energy between two distinct

emitters to perform measurements that require high degree of indistinguishability. Atomically thin crystals provide a promising avenue for achieving high degree of tuning with the aid of strain. This is because TMDs are intrinsically very flexible and brittle materials. They can be elongated to up to 11% before they fracture[*70*] showing steep slopes of high Young modulus 330 GPa[*91*]. Other 2D crystals, hBN monolayers and graphene, exceed these values reaching up to 25% strain limit[*92*] while conventional bulk GaAs fractures after 2% of strain and has a Young modulus of 80 GPa.

To date, the strain tuning of TMDs has been only concentrated on the emissions of delocalized 2D excitons and a recent review summarises these efforts very well[*93*]. These experiments provide knowledge about techniques of applying high strains to 2D crystals and calibration coefficient between the applied strain and bandgap modulation manifested by the spectral shift which will be used in this thesis to estimate the strain. Further, the work of Desai *et al.*[*94*] shows the power of strain tuning. With 2% strain, the PL emission of WSe_2 bilayer was amplified by 35 times. Although the impact of strain tuning on SQEs in TMDs has never been reported, it has great prospects due to extraordinary flexibility and tunability of the host material and the ability of engineering the optical properties, as was demonstrated in self-assembled QDs with the strain tuning of emission energy, magnitude and the phase of fine-structure spitting[*95*].

1.5 Summary

This introductory chapter started with a description of quantum technologies and their imprint on the current technologies in the fields of information science and beyond. It has been recognised that the photon plays an important role of a flying qubit in the quantum infrastructure. Also, when required the photon can be solely used to perform protocols within the framework of linear optical quantum computing that harnesses assets of quantum mechanics such as nonlocality and superposition.

As the previous section motivated the need for a perfect single photon source, the next section defined its main figure-of-merits as brightness, purity, indistinguishability, efficiency, lifetime, interface of stationary-flying qubit and spin coherence. The requirements for each quantity were specified, standardised ways of measuring them were noted and the specific examples were mentioned.

The next section briefly reviewed approaches (nonlinear processes, single atoms, epitaxial quantum dots, defects in solids and two-dimensional materials) to obtain streams of single photons and presented their strengths and shortcomings in relation to the

requirements necessary for enabling quantum applications. While none of the quantum photonic platforms met all requirements, the label of the best overall single photon source was given to man-made artificial atoms, self-assembled quantum dots. The section concluded by introducing the recently discovered quantum photonic platform of two-dimensional materials. Although very little is known about this type of SQE, features unique to 2D crystals were identified, some of which are likely to have a beneficial imprint for SQEs (i.e. fabrication procedure, assembly of 2D heterostructures, direct access, high tunability, valley-spin physics).

The chapter then described features of 2D semiconductors, in particular transition metal dichalcogenides (TMDs). The section briefly covered the genesis and pointed out the experimental immaturity of applications based on TMDs. Next, the focus shifted to the crystallographic structure where a number of polytypes were listed. While each polytype represents a distinct symmetry that underpins physical properties of the material, the focus narrowed to the 2H phase. Shortly after, it was appreciated that lattice symmetry shaped electronic dispersion and greatly influenced optical properties. As a result, TMDs monolayers accommodate two sets of bands at the edge of the Brillouin zone that exhibit an intriguing property: optically addressable selection rules that coherently link spin and valley together. It also became clear that, large Coulomb interactions is another decisive feature determining the physical phenomena in TMDs, leading to large binding energies of 2D excitons, trions and biexcitons. Finally, the overview of TMDs properties was completed with the prospect of high tenability, where strain is shown to be a favourable tuning knob due to high limits of elastic response of 2D semiconductors.

1.6 Organization of the thesis

The main results presented in this thesis are the fabrication and optical characterisation of SQEs and quantum-dot like emissions hosted by atomically thin WSe_2 and $MoSe_2$ and their relation to local strain.

Isaac Newton once said that "*techniques are the ways of seeing things*". So the first step towards understanding *things* is to understand *how things* were *seen*. The *things* in the context of this thesis would refer to the optical properties of 2D semiconductors. Hence, the aim is to induce light-matter interaction and measure the light to provide new insights about the physics. Chapter 2 will cover the *ways*, which are the experimental methods and techniques (i.e. lasers, confocal microscopy, spectrometer, spectral filtering, intensity interferometry, and photodetectors) enabling the optical characterisation. As the topic of this thesis lies in between fields of nanotechnology, material science and quantum optics,

there are additional *ways* essential for *seeing things*. These are nanopositioners for precise, nanometre-scale navigation, a cryostat for achieving low temperatures, an avalanche photodiode for fast and sensitive acquisition of single photons and a photon correlator with fast electronics for gathering statistics at the single photon level.

Chapter 3 will begin with an overview of commonly used fabrication methods that aim to produce high-yield of high-quality TMDs monolayers. Then, the chapter will describe the mechanical exfoliation with step-by-step procedures. Further, identification techniques used to confirm the thickness of the samples will be presented. Then, the all-dry transfer technique which provides a great degree of flexibility in assembling samples will be introduced and described

While the above is essential to *see*, Chapters 4-6 present what was *seen*: the optical properties of WSe_2 SQEs in Chapter 4, the impact of local strain on WSe_2 SQEs in Chapter 5 and the observation of quantum-dot like emissions in $MoSe_2$ in Chapter 6. The last Chapter 7 will broadly discuss and summarise the novelty of the work and include an open discussion on the nature of SQEs. Finally, the thesis will be concluded with an outlook and the future prospects arising from the presented results.

1.7 References

1. I. Aharonovich, D. Englund, M. Toth, Solid-state single-photon emitters. *Nature Photonics* **10**, 631-641 (2016).

2. W. B. Gao, A. Imamoglu, H. Bernien, R. Hanson, Coherent manipulation, measurement and entanglement of individual solid-state spins using optical fields. *Nat Photon* **9**, 363-373 (2015).

3. P. Senellart, G. Solomon, A. White, High-performance semiconductor quantum-dot single-photon sources. *Nature Nanotechnology* **12**, 1026 (2017).

4. M.-J. Sun *et al.*, Single-pixel three-dimensional imaging with time-based depth resolution. *Nature Communications* **7**, 12010 (2016).

5. B. Barrett, A. Bertoldi, P. Bouyer, Inertial quantum sensors using light and matter. *Physica Scripta* **91**, 053006 (2016).

6. R. J. Donaldson *et al.*, Experimental demonstration of kilometer-range quantum digital signatures. *Physical Review A* **93**, 012329 (2016).

7. X. D. Cai *et al.*, Experimental Quantum Computing to Solve Systems of Linear Equations. *Physical Review Letters* **110**, 230501 (2013).

8. J. Yin *et al.*, Satellite-based entanglement distribution over 1200 kilometers. *Science* **356**, 1140-1144 (2017).

9. B. P. Lanyon *et al.*, Simplifying quantum logic using higher-dimensional Hilbert spaces. *Nature Physics* **5**, 134 (2008).

10. P. W. Shor, paper presented at the Proceedings of the 35th Annual Symposium on Foundations of Computer Science, 1994.

11. R. P. Feynman, Simulating physics with computers. *International Journal of Theoretical Physics* **21**, 467-488 (1982).

12. D. P. DiVincenzo, The Physical Implementation of Quantum Computation. *Fortschritte der Physik* **48**, 771-783 (2000).

13. E. Knill, R. Laflamme, G. J. Milburn, A scheme for efficient quantum computation with linear optics. *Nature* **409**, 46-52 (2001).

14. G. B. C. H. Bennett, S. Breidbart and S. Wiesner, Quantum cryptography, or Unforgeable subway tokens. *Advances in Cryptology: Proceedings of Crypto '82*, 267 – 275 (1982).

15. H.-K. Lo, X. Ma, K. Chen, Decoy State Quantum Key Distribution. *Physical Review Letters* **94**, 230504 (2005).

16. P. L. McMahon, K. De Greve, in *Engineering the Atom-Photon Interaction: Controlling Fundamental Processes with Photons, Atoms and Solids*, A. Predojević, M. W. Mitchell, Eds. (Springer International Publishing, Cham, 2015), pp. 365-402.

17. M. M. Fejer, G. A. Magel, D. H. Jundt, R. L. Byer, Quasi-phase-matched second harmonic generation: tuning and tolerances. *IEEE Journal of Quantum Electronics* **28**, 2631-2654 (1992).

18. R. Hanbury Brown, R. Q. Twiss, A Test of a New Type of Stellar Interferometer on Sirius. *Nature* **178**, 1046-1048 (1956).

19. H. J. Kimble, M. Dagenais, L. Mandel, Photon Antibunching in Resonance Fluorescence. *Physical Review Letters* **39**, 691-695 (1977).

20. E. Waks, C. Santori, Y. Yamamoto, Security aspects of quantum key distribution with sub-Poisson light. *Physical Review A* **66**, 042315 (2002).

21. C. K. Hong, Z. Y. Ou, L. Mandel, Measurement of subpicosecond time intervals between two photons by interference. *Physical Review Letters* **59**, 2044-2046 (1987).

22. Z. Y. Ou, L. Mandel, Violation of Bell's Inequality and Classical Probability in a Two-Photon Correlation Experiment. *Physical Review Letters* **61**, 50-53 (1988).

23. F. Kaneda, K. Garay-Palmett, A. B. U'Ren, P. G. Kwiat, Heralded single-photon source utilizing highly nondegenerate, spectrally factorable spontaneous parametric downconversion. *Opt. Express* **24**, 10733-10747 (2016).

24. X.-L. Wang *et al.*, Experimental Ten-Photon Entanglement. *Physical Review Letters* **117**, 210502 (2016).

25. D. B. Higginbottom *et al.*, Pure single photons from a trapped atom source. *New Journal of Physics* **18**, 093038 (2016).

26. S. Debnath *et al.*, Demonstration of a small programmable quantum computer with atomic qubits. *Nature* **536**, 63-66 (2016).

27. N. Somaschi *et al.*, Near-optimal single-photon sources in the solid state. *Nature Photonics* **10**, 340 (2016).

28. X. Ding *et al.*, On-Demand Single Photons with High Extraction Efficiency and Near-Unity Indistinguishability from a Resonantly Driven Quantum Dot in a Micropillar. *Physical Review Letters* **116**, 020401 (2016).

29. L. Sapienza, M. Davanço, A. Badolato, K. Srinivasan, Nanoscale optical positioning of single quantum dots for bright and pure single-photon emission. **6**, 7833 (2015).

30. Y. He *et al.*, Time-Bin-Encoded Boson Sampling with a Single-Photon Device. *Physical Review Letters* **118**, 190501 (2017).

31. P. Michler *et al.*, A Quantum Dot Single-Photon Turnstile Device. *Science* **290**, 2282-2285 (2000).

32. T. Grange *et al.*, Reducing Phonon-Induced Decoherence in Solid-State Single-Photon Sources with Cavity Quantum Electrodynamics. *Physical Review Letters* **118**, 253602 (2017).

33. A. Nick Vamivakas, Y. Zhao, C.-Y. Lu, M. Atatüre, Spin-resolved quantum-dot resonance fluorescence. **5**, 198 (2009).

34. R. N. E. Malein *et al.*, Screening Nuclear Field Fluctuations in Quantum Dots for Indistinguishable Photon Generation. *Physical Review Letters* **116**, 257401 (2016).

35. G. Éthier-Majcher *et al.*, Improving a Solid-State Qubit through an Engineered Mesoscopic Environment. *Physical Review Letters* **119**, 130503 (2017).

36. D. Brunner *et al.*, A Coherent Single-Hole Spin in a Semiconductor. *Science* **325**, 70-72 (2009).

37. D. Press *et al.*, Ultrafast optical spin echo in a single quantum dot. *Nature Photonics* **4**, 367 (2010).

38. J. Wolters *et al.*, Enhancement of the zero phonon line emission from a single nitrogen vacancy center in a nanodiamond via coupling to a photonic crystal cavity. *Applied Physics Letters* **97**, 141108 (2010).

39. A. S. Denis D. Sukachev, Christian T. Nguyen, Mihir K. Bhaskar, Ruffin E. Evans, Fedor Jelezko, Mikhail D. Lukin, The silicon-vacancy spin qubit in diamond: quantum memory exceeding ten milliseconds and single-shot state readout. *arXiv:1708.08852*, (2017).

40. G. Balasubramanian *et al.*, Ultralong spin coherence time in isotopically engineered diamond. **8**, 383 (2009).

41. N. Bar-Gill, L. M. Pham, A. Jarmola, D. Budker, R. L. Walsworth, Solid-state electronic spin coherence time approaching one second. **4**, 1743 (2013).

42. D. H. Brendon C. Rose, Zi-Huai Zhang, Alexei M. Tyryshkin, Sorawis Sangtawesin, Srikanth Srinivasan, Lorne Loudin, Matthew L. Markham, Andrew M. Edmonds, Daniel J. Twitchen, Stephen A. Lyon, Nathalie P. de Leon, Observation of an environmentally insensitive solid state spin defect in diamond. *arXiv:1706.01555*, (2017).

43. T. Schröder *et al.*, Scalable focused ion beam creation of nearly lifetime-limited single quantum emitters in diamond nanostructures. **8**, 15376 (2017).

44. S. Tim, G. Friedemann, B. Moritz Julian, B. Oliver, Ultrabright and efficient single-photon generation based on nitrogen-vacancy centres in nanodiamonds on a solid immersion lens. *New Journal of Physics* **13**, 055017 (2011).

45. E. Neu, M. Agio, C. Becher, Photophysics of single silicon vacancy centers in diamond: implications for single photon emission. *Opt. Express* **20**, 19956-19971 (2012).

46. L. Matthias *et al.*, Evaluation of nitrogen- and silicon-vacancy defect centres as single photon sources in quantum key distribution. *New Journal of Physics* **16**, 023021 (2014).

47. K. S. Novoselov *et al.*, Electric Field Effect in Atomically Thin Carbon Films. *Science* **306**, 666-669 (2004).

48. C. Chakraborty, L. Kinnischtzke, K. M. Goodfellow, R. Beams, A. N. Vamivakas, Voltage-controlled quantum light from an atomically thin semiconductor. *Nat Nano* **10**, 507-511 (2015).

49. Y.-M. He *et al.*, Single quantum emitters in monolayer semiconductors. *Nat Nano* **10**, 497-502 (2015).

50. KoperskiM *et al.*, Single photon emitters in exfoliated WSe2 structures. *Nat Nano* **10**, 503-506 (2015).

51. S. Kumar, A. Kaczmarczyk, B. D. Gerardot, Strain-Induced Spatial and Spectral Isolation of Quantum Emitters in Mono- and Bilayer WSe2. *Nano Letters* **15**, 7567-7573 (2015).

52. A. Srivastava *et al.*, Optically active quantum dots in monolayer WSe2. *Nat Nano* **10**, 491-496 (2015).

53. P. Tonndorf *et al.*, Single-photon emission from localized excitons in an atomically thin semiconductor. *Optica* **2**, 347-352 (2015).

54. C. Palacios-Berraquero *et al.*, Atomically thin quantum light-emitting diodes. *Nature Communications* **7**, 12978 (2016).

55. T. T. Tran, K. Bray, M. J. Ford, M. Toth, I. Aharonovich, Quantum emission from hexagonal boron nitride monolayers. *Nat Nano* **11**, 37-41 (2016).

56. R. Bourrellier *et al.*, Bright UV Single Photon Emission at Point Defects in h-BN. *Nano Letters* **16**, 4317-4321 (2016).

57. N. Chejanovsky *et al.*, Structural Attributes and Photodynamics of Visible Spectrum Quantum Emitters in Hexagonal Boron Nitride. *Nano Letters* **16**, 7037-7045 (2016).

58. N. R. Jungwirth *et al.*, Temperature Dependence of Wavelength Selectable Zero-Phonon Emission from Single Defects in Hexagonal Boron Nitride. *Nano Letters* **16**, 6052-6057 (2016).

59. L. J. Martínez *et al.*, Efficient single photon emission from a high-purity hexagonal boron nitride crystal. *Physical Review B* **94**, 121405 (2016).

60. A. L. Exarhos, D. A. Hopper, R. R. Grote, A. Alkauskas, L. C. Bassett, Optical Signatures of Quantum Emitters in Suspended Hexagonal Boron Nitride. *ACS Nano* **11**, 3328-3336 (2017).

61. G. Grosso *et al.*, Tunable and high-purity room temperature single-photon emission from atomic defects in hexagonal boron nitride. *Nature Communications* **8**, 705 (2017).

62. T. Philipp *et al.*, Single-photon emitters in GaSe. *2D Materials* **4**, 021010 (2017).

63. P. Tonndorf *et al.*, On-Chip Waveguide Coupling of a Layered Semiconductor Single-Photon Source. *Nano Letters* **17**, 5446-5451 (2017).

64. A. Branny *et al.*, Discrete quantum dot like emitters in monolayer MoSe2: Spatial mapping, magneto-optics, and charge tuning. *Applied Physics Letters* **108**, 142101 (2016).

65. C. Chakraborty, K. M. Goodfellow, A. Nick Vamivakas, Localized emission from defects in MoSe2 layers. *Opt. Mater. Express* **6**, 2081-2087 (2016).

66. G. W. Mudd *et al.*, The direct-to-indirect band gap crossover in two-dimensional van der Waals Indium Selenide crystals. **6**, 39619 (2016).

67. J. Kern *et al.*, Nanoscale Positioning of Single-Photon Emitters in Atomically Thin WSe2. *Advanced Materials* **28**, 7101-7105 (2016).

68. D. S. Gabriella *et al.*, Nanobubble induced formation of quantum emitters in monolayer semiconductors. *2D Materials* **4**, 021019 (2017).

69. S. Kumar *et al.*, Resonant laser spectroscopy of localized excitons in monolayer WSe2. *Optica* **3**, 882-886 (2016).

70. S. Bertolazzi, J. Brivio, A. Kis, Stretching and Breaking of Ultrathin MoS2. *ACS Nano* **5**, 9703-9709 (2011).

71. G. Wang *et al.*, Giant Enhancement of the Optical Second-Harmonic Emission of ${\mathrm{WSe}}_{2}$ Monolayers by Laser Excitation at Exciton Resonances. *Physical Review Letters* **114**, 097403 (2015).

72. G. Moody *et al.*, Intrinsic homogeneous linewidth and broadening mechanisms of excitons in monolayer transition metal dichalcogenides. *Nature Communications* **6**, 8315 (2015).

73. K. F. Mak, C. Lee, J. Hone, J. Shan, T. F. Heinz, Atomically Thin MoS2: A New Direct-Gap Semiconductor. *Physical Review Letters* **105**, 136805 (2010).

74. A. Castellanos-Gomez, Why all the fuss about 2D semiconductors? **10**, 202 (2016).

75. A. C. Gang Wang, Mikhail M. Glazov, Tony F. Heinz, Xavier Marie, Thierry Amand, Bernhard Urbaszek, Excitons in atomically thin transition metal dichalcogenides. *Arxiv:1707.05863*, (2017).

76. J. M. Riley *et al.*, Negative electronic compressibility and tunable spin splitting in WSe2. *Nature Nanotechnology* **10**, 1043 (2015).

77. J. Lindlau *et al.*, The role of momentum-dark excitons in the elementary optical response of bilayer WSe2. *ArXiv e-prints*. 2017.

78. A. Splendiani *et al.*, Emerging Photoluminescence in Monolayer MoS2. *Nano Letters* **10**, 1271-1275 (2010).

79. K. F. Mak, J. Shan, Photonics and optoelectronics of 2D semiconductor transition metal dichalcogenides. *Nat Photon* **10**, 216-226 (2016).

80. K. He *et al.*, Tightly Bound Excitons in Monolayer WSe2. *Physical Review Letters* **113**, 026803 (2014).

81. K. F. Mak *et al.*, Tightly bound trions in monolayer MoS2. **12**, 207 (2012).

82. Y. You *et al.*, Observation of biexcitons in monolayer WSe2. *Nat Phys* **11**, 477-481 (2015).

83. E. J. Sie, *Coherent Light-Matter Interactions in Monolayer Transition-Metal Dichalcogenides*. (Springer International Publishing, 2017).

84. T. Cao *et al.*, Valley-selective circular dichroism of monolayer molybdenum disulphide. **3**, 887 (2012).

85. K. F. Mak, K. He, J. Shan, T. F. Heinz, Control of valley polarization in monolayer MoS2 by optical helicity. **7**, 494 (2012).

86. D. Xiao, G.-B. Liu, W. Feng, X. Xu, W. Yao, Coupled Spin and Valley Physics in Monolayers of MoS2 and Other Group-VI Dichalcogenides. *Physical Review Letters* **108**, 196802 (2012).

87. H. Zeng, J. Dai, W. Yao, D. Xiao, X. Cui, Valley polarization in MoS2 monolayers by optical pumping. **7**, 490 (2012).

88. Y. Wu, Q. Tong, G.-B. Liu, H. Yu, W. Yao, Spin-valley qubit in nanostructures of monolayer semiconductors: Optical control and hyperfine interaction. *Physical Review B* **93**, 045313 (2016).

89. A. Raja *et al.*, Coulomb engineering of the bandgap and excitons in two-dimensional materials. **8**, 15251 (2017).

90. F. Cadiz *et al.*, Excitonic Linewidth Approaching the Homogeneous Limit in MoS2-Based van der Waals Heterostructures. *Physical Review X* **7**, 021026 (2017).

91. A. Castellanos-Gomez *et al.*, Elastic Properties of Freely Suspended MoS2 Nanosheets. *Advanced Materials* **24**, 772-775 (2012).

92. C. Lee, X. Wei, J. W. Kysar, J. Hone, Measurement of the Elastic Properties and Intrinsic Strength of Monolayer Graphene. *Science* **321**, 385-388 (2008).

93. R. C.-G. Roldán, André;, Cappelluti, Emmanuele; Guinea, Francisco, Strain engineering in semiconducting two-dimensional crystals. *Journal of Physics: Condensed Matter* **27**, 313201 (2015).

94. S. B. Desai *et al.*, Strain-Induced Indirect to Direct Bandgap Transition in Multilayer WSe2. *Nano Letters* **14**, 4592-4597 (2014).

95. R. Trotta *et al.*, Wavelength-tunable sources of entangled photons interfaced with atomic vapours. **7**, 10375 (2016).

Chapter 2 Optics and spectroscopy: Methods and techniques

This chapter describes the methods and techniques to optically characterize the samples which were frequently implemented during my PhD. The purpose of this section is to explain working principles, key procedures and parameters of used apparatus. Ultimately, it will shine light on the equipment's capabilities and limitations.

2.1 The overall system

The overall system is displayed in the Figure 2.1.1 to show the equipment in a wider perspective. It is important to realise how each element influences and frequently limits each other. Understanding these limitations opens routes for potential improvements or developing more suitable alternatives.

The system is designed to perform cryogenic spectroscopy of any low dimensional semiconducting structure, for instance III-V self-assembled QDs, quantum wells, 2D semiconductors and their SQEs.

The interfaces between the subsystems are critical: between sample and cryostat, cryostat and confocal microscope, microscope and the optical table and more general between free space and fibres. Figure 2.1.1 shows a confocal microscope connected to each subsystem on the optical table via optical fibres which pose instant limitations (i.e. single mode coupling efficiencies, thermal intensity fluctuations due to fibre birefringence, limited freedom of adding optical elements to the confocal microscope). On the other hand, a solution involving free space optics requires replacing the confocal microscope with an additional platform which includes all optical subsystems and placed on the top of the

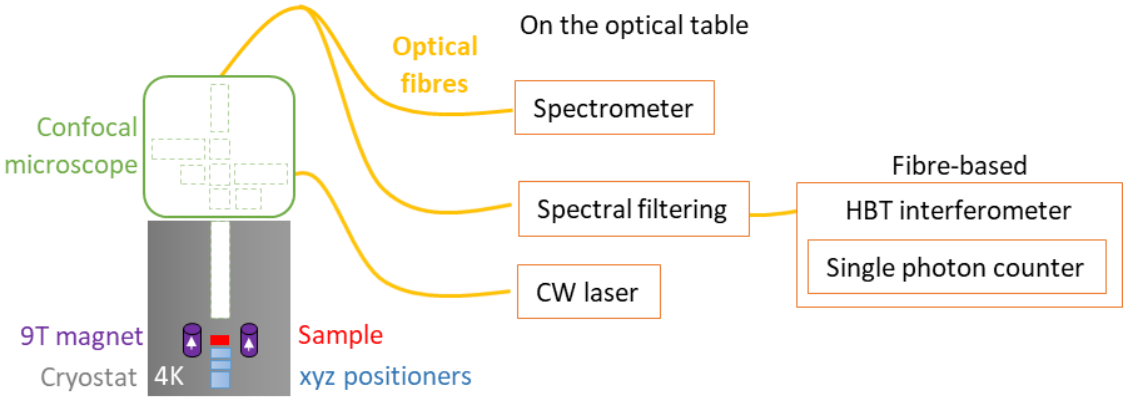

Figure 2.1.1 – The schematics of overall system used for optical characterization of the sample (in red), consisting of a cryostat (in grey) with 9T magnet (in purple), xyz positioners (in blue), confocal microscope (in green), optical fibres (in yellow) connecting the microscope with spectrometer, spectral filtering setup and fibre-based Hanbury-Brown Twiss interferometer with single photon counter.

cryostat. In any case, the optical fibres are present in the system and their limitations involve relatively low efficiencies of coupling laser light to fibres (typically ~70%) and collecting light from the sample (up to ~1%). Therefore, it is costly to switch between free space and the fibre. The loss of intensity also affects each fibre-to-fibre connection, practically essential in order to avoid the repetition of mundane alignments. Other drawbacks involve the high cost of polarisation maintaining fibres or birefringence and its dependence on temperature fluctuations in nonpolarisation-maintaining fibres. While working with fibres sometimes demanding, but manageable. However, there are significant advantages. In particular, in the confocal microscope and spectral filtering setups, the core of the fibre serves as a pinhole. In general, fibres are very easy to use and to handle, an example of which could be fibre-based Hanbury-Brown and Twiss interferometer which does not require any alignment.

Of all subsystems, the cryostat plays a key role because everything else is adapted to it. For instance, our cryostat limits the size of optics and the sample to 1 inch, restrains the maximum travel distance of the positioners, stretches the length of the microscope and challenges the objective with cryogenic compatibility that arises from high stresses due to different thermal expansion coefficients and thermal cycling. It is worth mentioning here that worktop cryostats are widely available but they do not allow large magnetic fields.

Taken as whole, the system has proven to be robust, performing well over the years of my research. Its modularity and flexibility allowed execution of a number of different measurements without major investments in time and money.

2.2 Scanning confocal microscope

2.2.1 Working principle

The scanning confocal microscope (SCM) is designed and built in-house. In its inventor's words, its main purpose is to "*take an image of the specimen with point by point examination of its optical properties*". Interestingly, the confocal microscope we build and use resembles very closely the first invention from 1955[*1*]. The striking similarities are illustrated by Figure 2.2.1a,b. In the lab, the modern microscope delivers laser light to the sample to induce light-matter interaction, then it collects the light emitted reflected, or scattered by the sample. This light is then sent to the spectrometer or photodetectors for analysis.

The confocal microscope differs from an ordinary optical microscope with its spatial selectivity achieved by “double focusing”. The confocal microscope illuminates and collects light from a single, diffraction limited spot that is pre-defined by the optical resolution of the system. The first pinhole on the illumination side makes sure that the light source can be treated as a point source. The second pinhole before the collection blocks undesirable light from scattered and out-of-focus locations which significantly improves the contrast. The diffraction limited performance is defined by the pinhole at the collection and the numerical aperture of the system.

2.2.2 The microscope design

The microscope used in the lab was assembled solely from individual components based on 30 mm Thorlabs cage system. All part numbers of optical components (purchased from Thorlabs or otherwise specified) which will be mentioned in this section are listed in a table in the Figure 2.2.1c. The microscope’s schematic is shown by the Figure 2.2.1b. The optical system comprises of the central part where beam splitters (BS) are placed and three arms are attached: excitation, collection, and imaging arms.

The design requires a collimated beam to propagate within the system. Therefore, the collection and excitation arms have collimating lenses for the light arriving at and coming out of a single mode (SM) fibre. These lenses were chosen such that (i) they have greater numerical aperture (NA) than the fibres which is 0.12-0.14 and (ii) they match the clear aperture of the objective lens for the maximum collection. In line with the principle of confocal microscopy, at both ends the core of the SM fibre act effectively as the pinhole. For example, a single mode fibre operating at wavelengths between 633 - 780 nm (SM600 Thorlabs) has a 4.3 µm core (giving mode field diameter between 3.6 – 5.3 µm).

The remaining imaging arm holds a CCD camera and a 1-inch lens with a 150 mm long focal length. This arm has two functions. It is used to align spatially the collection and excitation spots ensuring their collinear propagation. Under a white light illumination, the arm takes magnified images of the sample where flakes are located with the aid of nanopositioners. The white light illumination is done by attaching a white LED to a cube with a glass slide. Glass slide is easily removable and only present during the imaging because it introduces a beam shift that hinders the quality of alignment hence the collection efficiency.

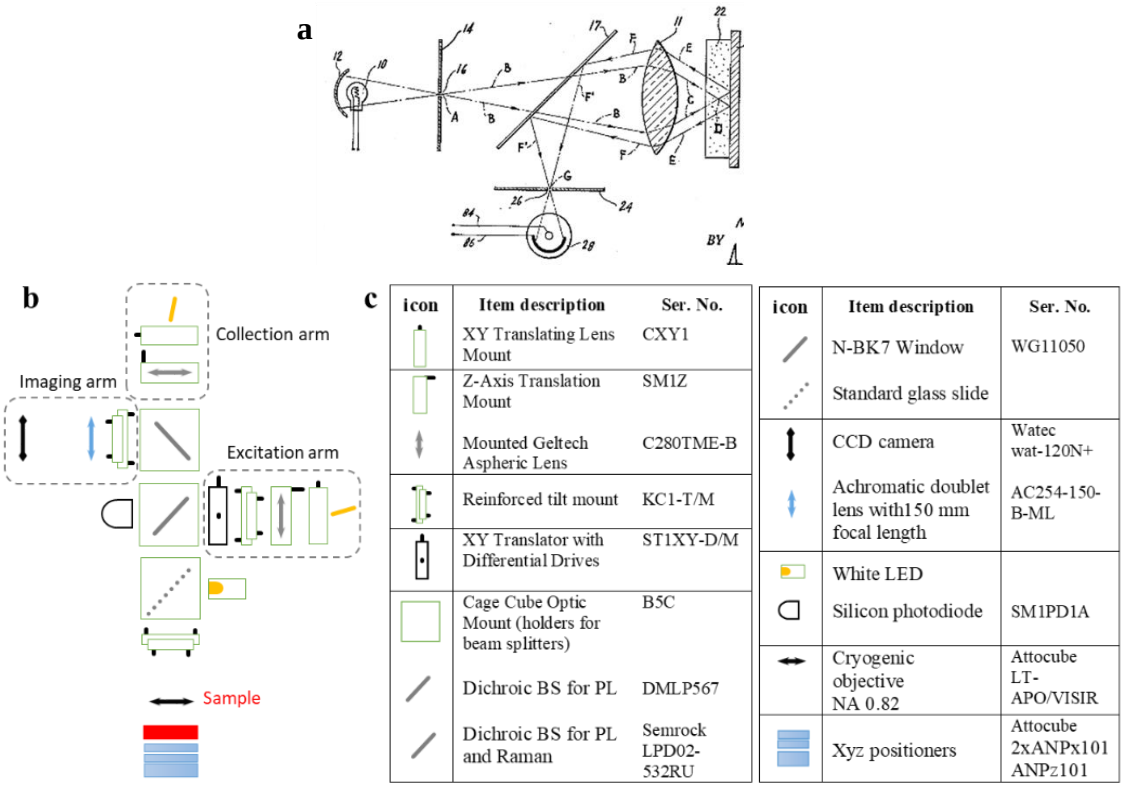

icon	Item description	Ser. No.
	XY Translating Lens Mount	CXY1
	Z-Axis Translation Mount	SM1Z
	Mounted Geltech Aspheric Lens	C280TME-B
	Reinforced tilt mount	KC1-T/M
	XY Translator with Differential Drives	ST1XY-D/M
	Cage Cube Optic Mount (holders for beam splitters)	B5C
	Dichroic BS for PL	DMLP567
	Dichroic BS for PL and Raman	Semrock LPD02-532RU

icon	Item description	Ser. No.
	N-BK7 Window	WG11050
	Standard glass slide	
	CCD camera	Watec wat-120N+
	Achromatic doublet lens with150 mm focal length	AC254-150-B-ML
	White LED	
	Silicon photodiode	SM1PD1A
	Cryogenic objective NA 0.82	Attocube LT-APO/VISIR
	Xyz positioners	Attocube 2xANPx101 ANPz101

Figure 2.2.1 – **(a)** The original drawing of the scanning confocal microscope by its inventor, Marvin Minsky [1], featuring a light source (no.10), objective lens (no.11), beam splitter (no. 17), pinholes (no. 14, 24) and detector (no. 28). **(b)** The schematics of the scanning confocal microscope used in the lab, is based on optical fibres and propagation of the collimated beam throughout the system. Collection, excitation and imaging arms are labelled while the table in **(c)** displays the legend of all components present in **b** with their serial numbers (all from Thorlabs unless otherwise specified).

The light propagating from and towards any arm and the sample is directed by a set of beam splitters situated inside the central part of the microscope. They need to be placed at 45 degrees and ideally help with separating excitation and collection wavelengths.

Whether the mode of the measurement is to collect photoluminescence (PL), Raman modes or resonant fluorescence (RF), the beam splitters need to be carefully chosen. The BS for each mode with their transmission ratios between signal (at 750 nm) and the non-resonant excitation laser (at 532 nm) are listed in Figure 2.2.1c. For instance, the dichroic BS (from Semrock) with the signal transmission ratio of 99:1 allows the majority of the PL signal to be transmitted and collected while the majority of the pump laser is reflected towards the sample and effectively filtered before the collection. The small fraction of transmitted excitation power is measured by a photodiode placed opposite to the excitation arm (as shown in Figure 2.1.1b). The thickness of the BS is worth to consider because it shifts the beam away from the centre of optical axis by refraction. The presence

of two BSs cancels out the shift in the collection path given that they are 90 degrees to each other and have the same thicknesses.

2.2.3 Collection efficiency

The collection efficiency of the non-resonant PL signal is defined by the NA of the objective, the quality of fibre coupling and the total transmission of all optics in the optical path (i.e. BS, objective lens). A cryogenic-suitable objective with a high NA of 0.82 collects the light within a 110-degree cone, representing ~61% of light emitted within the upper hemisphere. The intensity loss from optics (i.e. collimating lens) coated with anti-reflection dielectric layer is negligible (0.25% at 750 nm). However, the total transmittance of BS pairs are 98% or 63% for optics from Semrock and Thorlabs respectively (as listed in Figure 2.1.1c). Finally, after considering a moderate coupling efficiency of 50% the fraction of intensity collected by the confocal microscope is estimated to be of the order of 14%.

As the NA of the objective is already high (0.82), a gain in efficiency can be earned by using solid immersion lenses or fabricating nanostructures around the emitter such as micropillars, planar antennas, cavities or microlenses. These structures engineer the direction and the mode of the emission such that nearly 100% is collected even within a moderate NA (i.e. 0.68)[*2*]. This aspect is not the covered in this thesis but it remains relevant for any SQE.

2.2.4 Spatial Resolution

Apart from the collection efficiency the key specification of the scanning confocal microscope is the spatial resolution. In theory, adhering to the Rayleigh criterion, $\Delta x = 0.61\lambda / NA$, the spatial resolution of the microscope with the NA = 0.82 at $\lambda = 750$ nm gives the lateral resolution $\Delta x = 560$ nm, provided that the entire pupil of the objective lens is filled. The spatial resolution can be measured by collecting the reflected laser light from a sample with a pattern of high and low reflectivity surfaces with sharp edges or by measuring a cross-section of the integrated intensity from a spatial map of PL from a sample.

Scanning is achieved with moving nanopositioners which will be introduced in the following section. The first derivative of the step function relates directly to the spatial resolution Δx. Figure 2.2.2 demonstrates this approach with the optical image of a sample, the PL map with 270 nm step size, a cross section of the raw integrated intensity and its 1st derivative. The mean obtained from fitting Gaussian peaks to 6 steps from 3 different

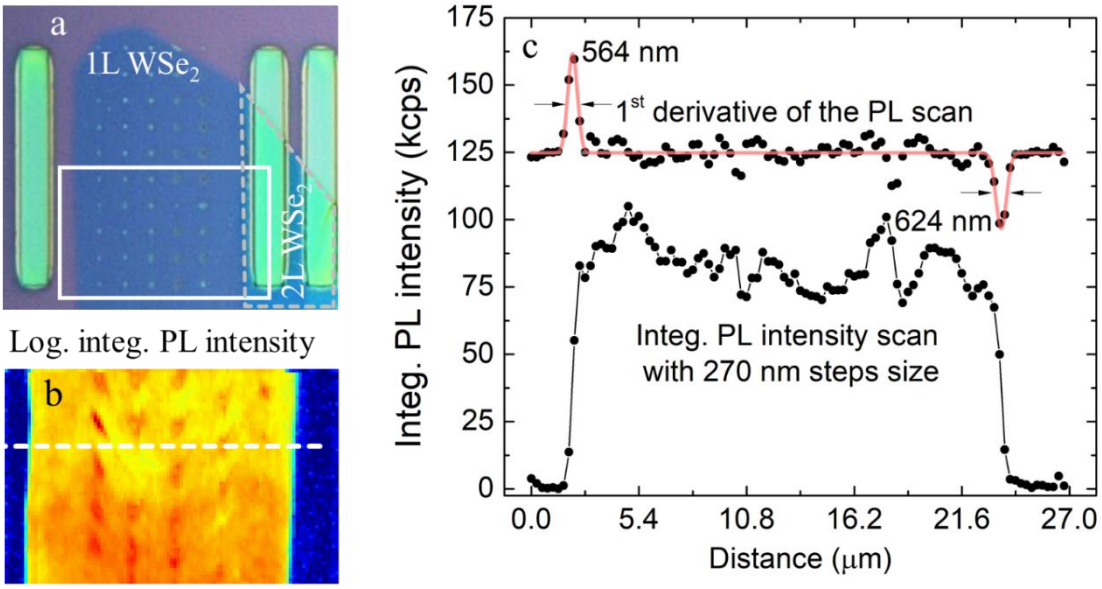

Figure 2.2.2 – **(a)** The optical micrograph of a 1L WSe_2 flake on a SiO2 substrate where region covered by a bilayer is marked by a gray box. **(b)** The PL spatial map of the region highlighted by the white frame in **a**. The map which was done with 270 nm step size reveals bright monolayer region and dark areas with bilayer and empty substrate. **(c)** The bottom trace, the intensity cross-section along the white line marked in **b**. Two steps indicate the monolayer-substrate and monolayer-bilayer boundaries. Above, the 1st derivative of the PL intensity trace (with 125k offset) with Gaussian fits giving FWHM of 564 nm and 624 nm respectively (Δx = 560 nm theoretically).

cross sections gives the spatial resolution Δx equal to 580 ± 70 nm, matching the theoretical value of 560 nm.

Mapping of the PL signal from a single emitter, can also localise the emitter spatial position beyond the microscope's resolution. In such a limit, the emitter is seen as a point source. The measured intensity profile of the point source directly corresponds to the point spread function (Airy disk) convoluted with the microscope, hence the spatial resolution. Figure 2.2.3 illustrates this method. Figure 2.2.3a shows emitter at 760 nm and its inset shows the integrated intensity map with 110 nm step size for a 1 nm spectral window. Fitting Airy disk lineshapes to horizontal and vertical cross sections yields to the spatial resolution, of 600 and 560 nm respectively as shown in the Figure 2.2.3c.

Note that due to achromatic aberrations in the objective and other lenses, the spatial resolution of the scanning confocal microscope will be optimised only for a limited spectral range for any fixed focal plane. In order to achieve the diffraction limited performance, the focal plane should be maintained.

Fitting peak functions to the intensity profiles of localised emitters allows one to determine their position with accuracy beyond the diffraction limit of the confocal

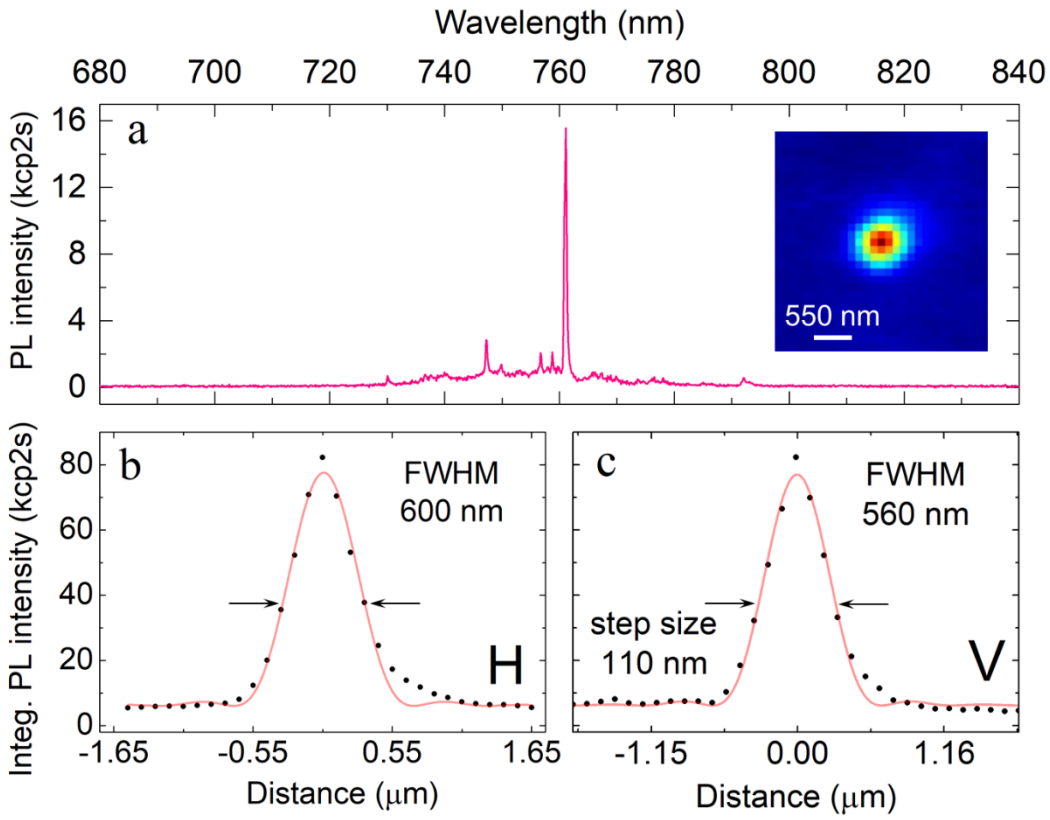

Figure 2.2.3 – **(a)** The PL emission from a localised SQE hosted by 1L WSe2 exhibits a single, dominant line at 760 nm. The inset shows the PL map of the central emission within 1 nm bandwidth where each pixel represents a 110 nm step. **(b)** Horizontal and **(c)** vertical cross sections of the PL map in a with Airy disk fits in red showing mean FWHM of 600 and 560 nm, respectively, which agrees with theoretical 565 nm (for $\lambda = 760$ nm).

microscope (Δx). This can be achieved when the step size of scanning is much smaller than the optical spatial resolution and with a large signal to noise ratio. For instance, the scanning step size of the PL intensity map in Figure 2.2.3 is ~5 times smaller than the spatial resolution, and the fit provides a positioning accuracy on the order of few nm (± 3 nm for both cross-sections in Figure 2.2.3).

2.3 Nano-positioners

The previous section showed that the nanopositioners allow for precise determination of a SQE localization. Besides a very fine, few nanometre step size, the positioners also provide movement over a millimetre range. This is a desirable feature because exfoliated monolayer flakes of 2D materials typically appear in sizes of the order of tens of μms (see Chapter 3). Therefore, searching for a relatively small region in the sea of empty wafer requires long distance navigation.

The stepper's working principle reflects how simple and elegant ideas can enable powerful and reliable technology. The movement is driven by the inertia. The inertia is

afforded by a carefully achieved balance between friction at interfaces of a moveable table and the force impulse launched by the sawtooth signal. At the peak of the pulse, the piezoelectric element is fully expanded, proportionally to the peak's height. Because the pulse retreats very fast, the inertia of the movable table overcomes friction which leaves the table at extended position whereas the piezoelectric comes back to its nearly original position. It is like moving a coin on a sheet of paper towards the edge by only moving the paper slowly forward and quickly backward.

As highlighted in section 2.1, other demands and constraints on the nanopositioners involve, a compact design due to limited space inside the 30 mm cage system for optics, the capability of working at cryogenic temperatures, a high vacuum of 10^{-5} mbar, and a high magnetic field up to 9T. All these requirements can be met thanks to piezo-based, stepper positioners (manufactured by Attocube Systems). Made from titanium, these modular positioners provide three independent axes of movement that extend to up to 5 mm with few nanometre resolution (product no. ANPz101, ANPx101). Moreover, the fine PL spatial mapping which will be seen throughout this thesis was done by distinct scanner (product no. ANSxy101lr). The scanner has a higher degree of accuracy and reproducibility than positioners but relatively small (i.e. 30×30 μm^2) scan area.

Each positioner, hence each axis is independently controlled by a branded unit. This allows adjusting speed and the step size of the movement with tuning the frequency and the amplitude of the sawtooth signal that is sent to the steppers. On the other hand, the scanner moves by receiving a constant DC voltage and requires its own controller. While using any of them, it is important to bear in mind about the polarity and the amplitude of the applied voltage. If inappropriately used both, polarity and amplitude can damage the driving piezoelectric element. It is worth mentioning that these steppers also work at room temperature just with slightly different specifications.

In summary, the Attocube's motion control solutions proved to be extremely useful and in many aspects essential for the measurements to take place. Withstanding extreme conditions, they enabled cryogenic magneto-optics. They could locate the device and then finely scan the sample with 10 nm step size, which is much smaller than the optical resolution of the confocal microscope - 600 nm. Thanks to this, the positioners enable pinpointing a SQE with high spatial resolution. They can also stay at that precise location for hours enabling long overnight measurements (such as HBT interferometry) to be performed without any special effort.

Every characterisation procedure of 2D semiconducting flakes starts with a spatial PL map to search for SQEs, meaning that the speed of scanning is an important experimental parameter. Most of the time, it is necessary to utilise the maximum scanning range due to the flake dimensions. Moreover, due to the brightness of the sample and the collection efficiency of the optical setup, 1 second of acquisition time per spectrum is frequently used. Therefore, scanning the total area of 900 μm^2 with a moderate 200 nm step size requires 6 hrs and 20 min, a considerable amount of time. The acquisition time of 1 sec guarantees error-free communication between the apparatus, ensures sufficient signal to background ratio (SBR), and minimises spatial blur.

The long scan time is also partly caused by the in efficiencies associated with the spectrometer. Therefore, the outgoing fibre could be connected to the avalanche photodetector (APD) for much faster read out. Although this approach loses the spectral information, it could speed up scans significantly thanks to much larger SBR and could replace the first step of characterisation procedure which is to find locations of SPE. This scheme still needs to be tested by looking at how fast the scanner can be driven without inducing major artefacts due to reduced stability.

The scanning time could be further and significantly reduced by implementing a wide-field imaging approach[*3*] which captures instantly the same amount of data within its field of view as scanning. Another solution is to use a multimode fibre at the collection and exploit the imaging capabilities of the spectrometer (Isoplane 320). These techniques will start to be competitive when the sizes of flakes start exceeding 50×50 μm^2, however until now the nanopositioners and scanners were heavily used as they were well-suited for this purpose.

2.4 Cryostat

Monolayers of WSe_2 are direct semiconductors that luminesce at room temperatures. On the other hand, the SQEs found in WSe_2 are not strongly bound and most of them disassociate before the temperatures reach a few tens of Kelvin. Therefore, cryogenic temperatures are essential.

The cryostat, an Attodry1000 was purchased as a complete, plug-and-play system from the Attocube Systems. This model keeps the inner tube at the temperature below 4K with 25 mK peak-to-peak stability. Thermal insulation of the coldhead is attained by placing it in high vacuum environment (at least 1E-4 mbar) and by transferring the cold to sizeable copper stages. While allowing cooling by direct contact to the copper heat sinks, the

design makes sure that the vibrations coming from the pulse-tube (coldhead) are decoupled from the sample. The vibrations are further minimised by placing the cryostat on 8 floating legs sandwiched by 2 wooden platforms. The vibration stability is outstanding which enables long, unattended measurements. The specification sheet quotes that vibration amplitudes of 0.15 nm root mean squared is routinely measured by atomic force microscope (AFM).

The coldhead operates on the basis of closed dry cycle where an amount of high purity helium constantly travels between a compressor and the coldhead. Helium goes through decompressing and compressing stages removing a fraction of the heat after each cycle. Therefore, the system effectively does not handle a cryogen, instead the sample is mounted in a microscope insert inside a tube and it is cooled by a controlled exchange gas atmosphere, for which helium gas is typically used.

Before the sample can be loaded into the cryostat, the tube is pumped until its vacuum reaches at least 5E-4 mbar and subsequently filled with 100 mbar of helium exchange gas. In certain circumstances, such as applying large electric voltages, this helium pressure becomes dangerous because it can discharge and explode. With a different type of insert tube, where the temperature exchange is supported by a copper coupling with the bottom of the tube, the exchange gas is not required or kept at low 5E-2 mbar level. Nevertheless, once the cryostat is already cold and operational, it takes very little time, around 1.5 hrs to cool down the sample from 300 to 4 K. This cannot be said about the entire system. For the cryostat including a superconducting magnet it takes up to 15 hrs to cool down.

Once cold and loaded, the sample can be kept cold for months at a time. It can be put under the influence of vertical magnetic field as strong as 9 T, and can be heated up to tens of Kelvins using a sample heater. Heating presents a threat for the superconducting magnet: if the temperature is too high the magnet can quench. A safe and convenient way of heating the sample to an arbitrary temperature is to use variable temperature insert (VTI) which is supported by the Attodry 1100. There, an additional chamber between the tube and the cold sink (where the coldhead and the magnet are) is kept under the vacuum to decouple the cold from the sample. This prevents quenching magnet.

Although the cryostat can run constantly uninterrupted, the compressor does require maintenance. Its static helium pressure needs to be maintained at 250 ± 5 PSI. While working, the low and high dynamic pressures should be maintained at 150 and 350 PSI,

respectively. When the pressure is out of the range, the compressor needs to be refilled with high purity CP grade helium gas.

In short, the Attodry1000 is a sophisticated cryogenic solution which offers thermal stability below 4K, low-vibration, low-maintenance, short cooling times, uninterrupted use, variable temperature and out-of-plane magnetic field, and single optical access. All these features merged in a single place constitute a powerful tool for studying SQEs in 2D semiconductors.

2.5 Spectrometer

Once the PL signal emitted by the sample leaves the confocal microscope, its properties such as intensity, wavelength and linewidth can be analysed by an optical spectrometer. The spectrometer used in the lab is based on a common design of Czerny–Turner spectrograph (Princeton Instr. SpectraPro 500).

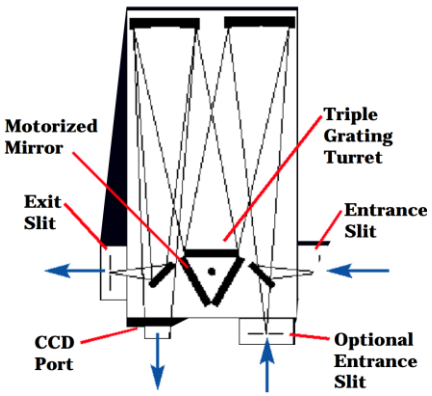

Figure 2.5.1 The diagram of the Czerny–Turner spectrograph where all components are named. The image taken from the SpectraPro 500 manual.

The principle of working of Czerny–Turner spectrograph is displayed in the Figure 2.5.1. The incoming light is focused at an entrance slit at the angle which matches the f-number (f/6.5) of the spectrograph (SpectraPro 500). After the slit, the light is collimated by a mirror and aimed at a square, 68×68 mm grating where the light is diffracted towards another concave mirror. The mirror focuses the dispersed light on the face of a nitrogen-cooled charge-coupled device (CCD, product no. Pylon:100 Excelon, 1340×100 pixels from Princeton Instr.). The pixel number on the CCD camera corresponds to the wavelength of diffracted light. The smallest detectable portion of the spectrum is determined by the pixel size (i.e. 20 μm) which acts as the exit slit in a monochromator and the linear dispersion of the entire optical system. The dispersion depends on the number of lines in the grating (i.e. 300, 1200, 1800 lines per millimetre), the focal length of the spectrometer (i.e. 0.5 m) and the variable width of the entrance slit (the minimum

size of 2 pixels, 40 μm). Having these factors in mind together with optical aberrations, the maximum spectral resolution was measured to be around 45 μeV for λ = 750 nm.

The spectral resolution implies that any emission linewidth larger than the resolution will be fully resolved. Otherwise, the analysed emission will be limited by the spectrometer. In such case, other instruments like a Fabry-Pérot interferometer could be used to measure the intrinsic homogenous linewidths of very sharp emissions reaching limits of tens of MHz.

2.6 Spectral filtering

For practical reasons, the HBT interferometer is almost always preceded by spectral filtering. This is a necessity due to spectral proximity of other SQEs, broadband and weak PL background, and stray light from the pump laser. Two filtering systems were built and implemented accordingly to the circumstances. As the SQEs hosted by WSe_2 occur randomly within a wide spectral range, tune-ability was the key factor in designing the filters.

One filtering solution, illustrated in the Figure 2.6.1a, was achieved using two angle-sensitive bandpass filters (Semrock product no. TBP01-790/12). The inset of the Figure 2.6.1a illustrates the working principle of the setup: the angles of both bandpass filters (blue and red) are selected to tune the transmitted wavelengths and allow for a narrow window where both transmissions coincide. Two mirrors in the path after the filters are to correct for the optical axis shift caused by tilting the filters. The Figure 2.6.1b shows that each bandpass filter transmits ~20 nm wide spectral window with 10E4 attenuation. The spectral tunability and resolution are presented in Figure 2.6.1c. Thanks to tilting the filter covers the spectral range between 690 – 810 nm. The spectral resolution is defined by the sharpness of the step in the spectrum. In Figure 2.6.1c, the 1st derivatives of the spectrum directly relates to the filtering resolution which gives values of 2 meV.

A second filter system, displayed in the Figure 2.6.1, was based on a transparent volume phase holographic grating (1200 lines/mm, 50.8 mm in diameter, 6 mm thick) which was custom made by Wasatch Photonics. Here, the filtering range spanned 720 – 820 nm with high (85% at 770 nm) and almost constant diffraction efficiency. This system works the same as a single-pixel spectrometer, where the size of the exit pixel, here the diameter of the fibre core, decides the transmitted bandwidth.

Both the fibre core diameter has and the total illuminated area on the grating influence the resolution. When the beam is collimated, the clear aperture of the lens accounts for

the illuminated area while the lens' NA should be matched with the NA of the fibre. If

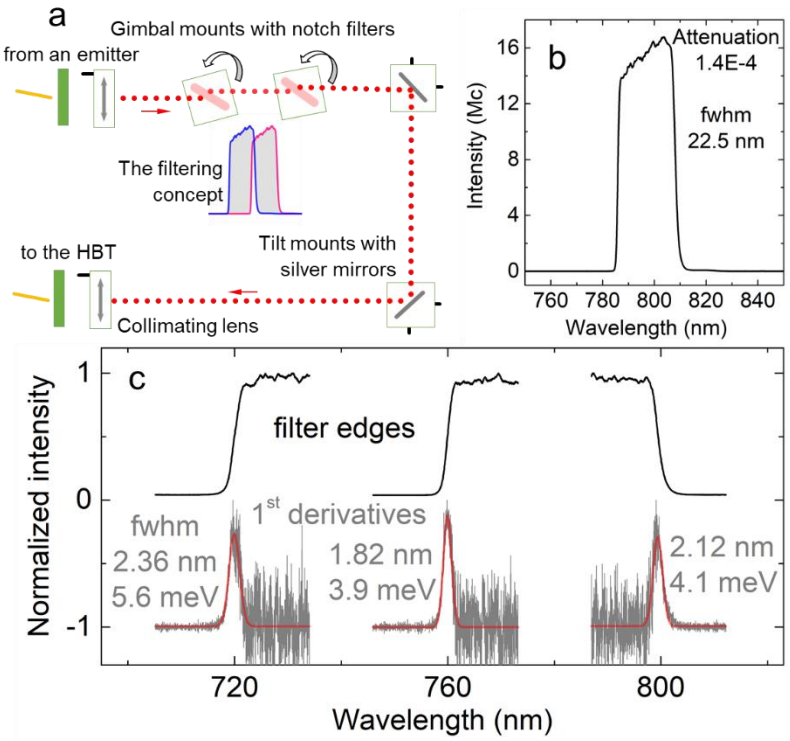

Figure 2.6.1 – **(a)** Schematics of filtering system based on two ~20 nm wide, angle-sensitive bandpass filters where two silver mirrors correct the beam shift due to filter tilt. The inset, in the middle explains the filtering concept where the narrow white part is transmitted. **(b)** A spectrum showing white light illumination transmitted by the bandpass filter at 0 degree angle of incident which gives the attenuation of 1.4E-4 and the spectral width of 22 nm. **(c)** Above, in black, normalised high resolution spectra of filter edge at different tilt angles showing its full tenability range (720 – 810 nm). Below, in grey, the 1st derivatives of the edge which define the filter resolution by fitting with Gaussian lineshape.

the NA is too high, the lens will be under filled, reduces the effective clear aperture and the sharpness of the filter. If too low, only a fraction of the light will be collected by the lens. Therefore, for the narrowest filtering, the goal is to find a lens with the largest clear aperture possible which satisfies the proportionality ratio given by the NA of the fibre, $2*NA_{fibre} = D_{lens} / f_{lens}$, where f is the focal length, D is the clear aperture and $D_{lens} < D_{grating}$. For this setup lenses with f = 16 mm, D = 4.48 mm, NA = 0.14 were used. For instance, a single mode fibre with 5.5 μm core granted 0.414 meV (0.20 nm) bandwidth and a multimode fibre with 50 μm core 2.5 meV (1.23 nm), both tested at 780 nm.

Finally, the gimbal mirror mounts facilitated precise on-the-optical-axis rotation so the overall system efficiency could reach 71%, which includes the 15% loss from diffraction.

Spectral filtering is an essential step in characterising individual SQEs with a HBT interferometer. The home-built filters presented in this section offered a desirable balance

between the high efficiency (up to 71%), the flexible tune-ability over a wide spectral

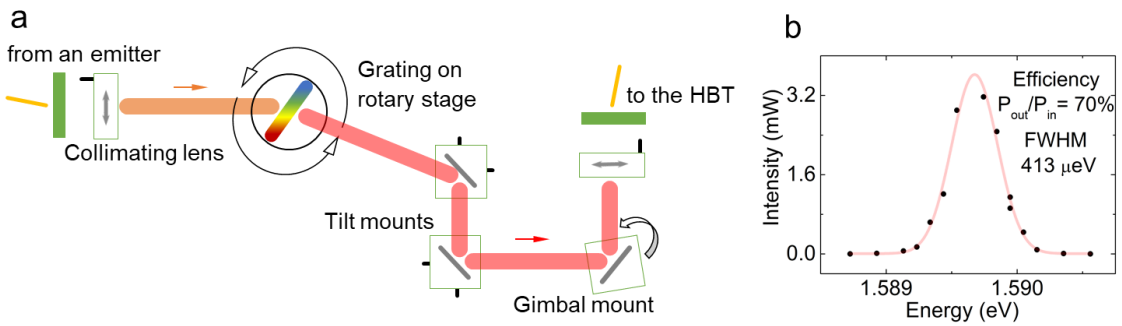

Figure 2.6.1 - **(a)** Schematics of a filtering system based on a diffraction grating. **(b)** The characterization of filter transmission measured at fixed position with tuneable laser emission energy, collimating lens illuminating the grating with a circular area, 4.5 mm in diameter and a single mode fibre at the collection (with 5.5 μm core diameter).

range (720 – 820 nm) and narrow filtering bandwidth (down ~400 μeV) allowing for efficient acquisition of low noise, high quality data.

2.7 Single photon counting module

A single photon avalanche diode (SPAD) is a semiconductor device made of reverse biased pn junction designed to measure very low fluxes of light, down to single photon level, by multiplying photo-generated current. In SPAD technology, the single-photon sensitivity is achieved by working at voltages beyond the breakdown voltage (the Geiger-mode). The SPAD module used in the lab (product no. SPCM-AQRH-15-FC) from Excelitas utilises silicon as the active photodiode with an exposed circular area with 180 μm in diameter. Responsivity of silicon gives rise to high, 67% peak photon detection efficiency at 750 nm and the in-built fibre flat ended coupler (FC-PC) ensures even elimination providing the ease of plug-and-play use.

Although the working conditions of the SPAD makes it challenging to suppress dark counts from thermally-generated electrons within the device, the module with 50 counts per second (cps) of dark counts are available. Another artefact is afterpulsing, which arises from the carriers released from trap states after the primary pulse is detected. Interestingly, the degree of afterpulsing can be measured by looking at the outcome of auto-correlating the dark counts. There, one should see clear distinction between Poissonian statistics of the thermal generation and non-Poissionian nature of the afterpulsing.

The SPAD has 350 ps single photon resolution, but its dead time disables the device for 22 ns. The dynamic range of the counting module saturates at 35 Mcps and directly correlates the number of counts to the number of photons. The output pulse is 10 ns long

with an amplitude of 2.2V, useful for electronic timing modules used to correlate photon arrival times.

In summary, SPADs are trigger devices capable of meeting demands of lab's everyday low light spectroscopy of WSe_2 SQEs.

2.8 Hanbury-Brown and Twiss interferometer

The working principle of Hanbury-Brown and Twiss interferometer was described in the previous chapter and can be found in Section 1.2.2. This section goes more in-depth by explaining experimental practicalities of using HBT interferometer and introducing the equipment in use.

From the practical point of view, the value of $g^{(2)}(0)$, previously defined as purity of SQE, can be compromised due to two reasons. First, nonsufficient filtering leads to collecting uncorrelated stray light. Second, the full depth of the dip is not resolved when the time resolution of the correlating system is slower than or comparable to the exciton lifetime. The correlator (product no. PicoHarp 300) does not jeopardise the dip of $g^{(2)}(\tau)$ as it can tag times as fast as 4 ps between subsequent photons, but SPAD jitter limits the time resolution to ~300 ps.

In order to extract correct lifetime and the purity from the $g^{(2)}(\tau)$ curve, the fitting should include deconvolution step of the SPAD time resolution to decouple the SPAD's response from the $g^{(2)}(\tau)$. Another discrepancy might relate to the decay time. When a single exponential properly represents the raw data, the $g^{(2)}(\tau)$ signifies a two level system. The deviation from this rule would entail fitting multiple exponentials with multiple lifetimes and hint at the presence of dark, metastable states which are involved in the process of creating a photon. All of the above need to be taken into account when characterising novel SQEs.

A fiber-based Hanbury-Brown and Twiss interferometer suitable for 750 nm (single mode fibre 50/50 splitter product no. FC-632-50B-APC) was used for second-order correlation measurements. Coincidence events from two silicon SPADs were recorded electronically and synchronized by two input channels on the PicoHarp300 with a time delay between start and stop triggers. The delay was achieved by a BNC cable leading to the start channel with a length of several tens of meters (the signal travels with 2/3 speed of light in BNC cables). The overall timing jitter of the system (of 350 ps) and high efficiency of SPADs (65% at 750 nm) were suitable for investigating WSe_2 SQEs as their lifetimes vary between 2 and 10 ns.

2.9 References

1. M. Minsky, confocal microscope. *Patent US 3013467 A,* (1957).

2. M. Brotons-Gisbert, P. Martínez-Pastor Juan, C. Ballesteros Guillem, D. Gerardot Brian, F. Sánchez-Royo Juan, in *Nanophotonics*. (2018), vol. 7, pp. 253.

3. A. Neumann *et al.*, Opto-valleytronic imaging of atomically thin semiconductors. *Nature Nanotechnology* **12**, 329 (2017).

Chapter 3 Fabrication of 2D Materials

3.1 A brief overview

The fabrication of 2D crystals has been on the frontier of the scientific efforts ever since they were discovered and their extraordinary properties became known. The development of a method which would supply high volume, high quality monolayers is already in sight for graphene [*1*].

This chapter will cover how monolayers are produced and how to integrate them into devices. Only with devices can scientists gain the control over the properties of 2D crystals and benefit from features arising from their 2D nature.

To begin, I will overview the commonly used approaches which are compatible with any 2D crystal, with an emphasis on semiconducting monolayers like WSe_2. Thereafter, the focus will change to a single technique in constant use throughout my thesis: mechanical exfoliation and all-dry transfer.

Any fabrication technique obeys one of two distinct approaches: bottom-up or top-down. In the context of 2D materials, a top-down technique derives monolayers from a bulk crystal. The bottom-up approach builds layer-by-layer from the elements. In 2004, the first 2D material (made of a single sheet of carbon atoms) was isolated from the bulk using mechanical exfoliation - simply achieved with scotch tape. Since that discovery, many different techniques emerged from other well-established fields and were implemented on the entire family of 2D crystals. A comprehensive review on the recent advances in fabrication can be found in references [*2*, *3*].

3.1.1 Bottom – up

The starting point for the bottom-up approach is the purified elements which constitute the crystal. These elements are individually heated and kept in the same container. In a vapour form, they travel by diffusion towards the target substrate where they mix and interact. Obeying the chemistry and tuned by controlled conditions (e.g. temperature gradient), the elements self-assemble and form the final desired product. One well-established technique to achieve this is chemical vapour deposition (CVD).

In CVD, as illustrated in Figure 3.1.1, the precursor elements are individually heated beyond their sublimation point. In the vapour form, they travel by diffusion towards the target where they condense. This condensation drives the crystal forming process. The rate of crystal growth can be controlled by adjusting the pressure and the temperature difference between the source and the growth substrate.

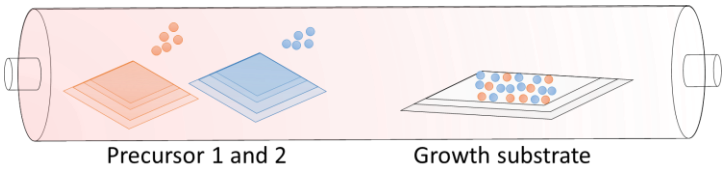

Figure 3.1.1 – Schematic of solid-precursor chemical vapour deposition (CVD), which involves two precursors. In this case to grow layered WSe_2, on one end of the tube the precursors would be pure selenium and WO_3. Other types of CVD include chalcogenization of pre-deposited precursor or physical vapour deposition, which uses already assembled TMD as a precursor for the regrowth.

This process has been successful in growing uniform, large-area single sheets of graphene [*4*]. Therefore, it also aspires to deliver the same results for TMDs such as WSe_2. The quality of CVD grown TMDs is improving, and begins to provide the desirable quality and the level of control. However, the uniformity across a large wafer and control over the number of layers remains challenging [*2*].

Growing high quality monolayers is just the first step in the process of fabricating a device. Each device requires a customised substrate that is compatible with post processing steps, for instance electron beam lithography for making metal contacts or transfer techniques for assembling a heterostructure. CVD provides a few options to synthesize 2D crystals directly on different substrates or 2D crystals, but the list of choices is not very extensive [*2*]. Otherwise, the CVD relies on a liquid lift-off or pick and place techniques in order to integrate monolayers into useful devices. The liquid transfer is an intrusive step in attempting to fabricate devices of pristine quality. Despite this, CVD has a unique capacity of fabricating lateral heterostructures[*5*] which is not available option for top-down methods. Equally, the CVD is well-suited to produce alloys of any concentration for instance in $W_xMo_{1-x}S_xSe_{1-x}$[*6*].

In conclusion, bottom-up synthesis requires substantial time investment to optimise the growth parameters, but remains relatively inexpensive technology. Despite the high price tag of running and maintaining, the bottom-up is probably the only scalable and feasible scheme for providing a large scale ultraclean, uniform, wafer-sized and encapsulated 2D crystals of high quality. All of these aspects are necessary to satisfy demands of optoelectronic and photonic applications of the future.

Another approach which also obeys the bottom-up philosophy is epitaxial growth[*7*] and pulsed-laser deposition[*8*]. Their early age makes it difficult to predict their success, but as any new technique they have their unique advantages but only modest differences because the global principle of the bottom-up is preserved.

3.1.2 Top – down

The top-down approach of producing 2D crystals utilises a number of techniques which isolate single layers from the host bulk crystal. As we learnt from the introduction Chapter 1 and Section 1.4.2, the adjacent layers in the bulk are connected via a weak, out-of-plane van der Waals force, which makes isolating monolayers possible.

The main rational driving the top-down approach is the high crystallinity of monolayers derived from man-made bulk crystals. Therefore, top-down monolayers are in general of better quality than those fabricated with bottom-up techniques. To date, bottom-up techniques include mechanical exfoliation[*9*], liquid exfoliation[*10*] - intercalation and sonication, and layer by layer thinning via laser[*11*] and plasma etching[*12*], as illustrated in Figure 3.1.2.

The first demonstration of breaking the attractive interactions between layers was done with adhesive forces of "scotch" tape. This technique is known as a mechanical exfoliation and a mechanical cleavage. In brief, the bulk crystal is sandwiched between two stripes of sticky tape which are pulled apart. The bulk separates into two thinner pieces that break at random locations. After repeating this intrinsically stochastic process, the bulk becomes thin enough to be exfoliated one last time onto a target substrate. The

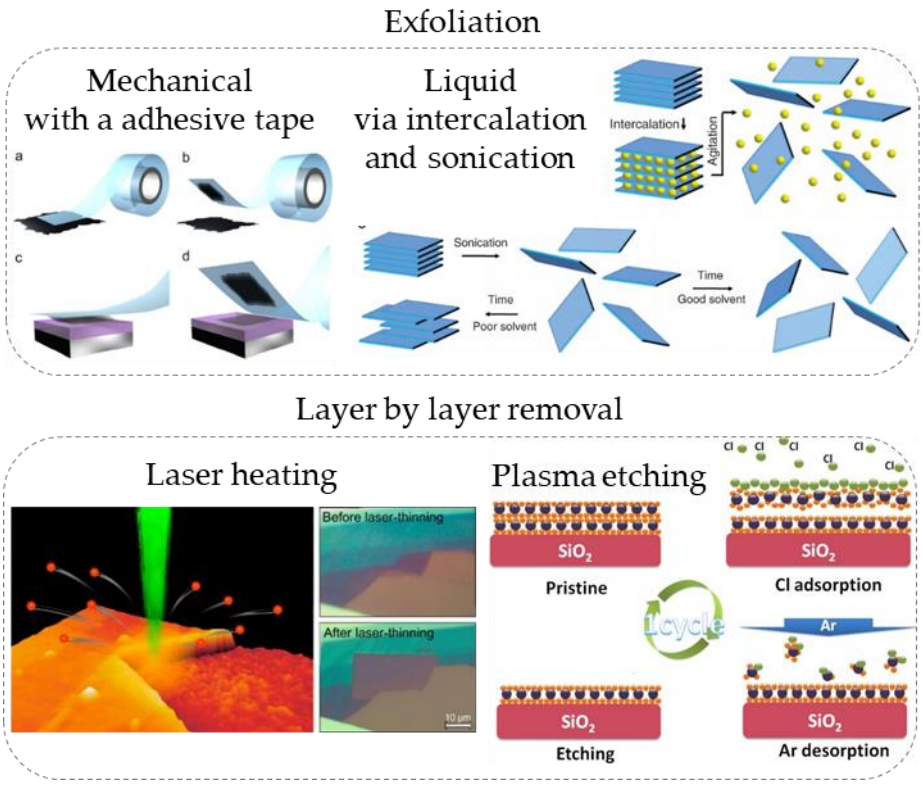

Figure 3.1.2 - Top-down fabrication methods for obtaining monolayers of 2D crystals which include mechanical and liquid exfoliations and layer by layer thinning aided by the laser and plasma etching. Figures were adapted from ref. [9-12], respectively.

thicknesses of exfoliated flakes are then examined. The easiest and the quickest way to find monolayers and distinguish them from thicker flakes is to use an ordinary optical microscope and measure their contrast against the substrate where the intuition holds - the smaller the contrast the thinner the flake. The principle of optical identification depends on Fresnel interference which is explained in depth in Section 3.3.1.

Remarkably, 13 years after introducing graphene, the original scotch tape technique prevails and still finds a wide audience. Mechanical exfoliation owes its popularity to its low cost, the simplicity of the procedure, and the availability of resources.

Because it is impossible to control how the bulk crystal separates under the adhesive forces, the embedded randomness of this technique likely blocks a path towards scalable manufacturing. The area of achievable monolayers is typically limited to few thousands of μm^2. It is difficult to imagine a factory implementing the scotch tape technique. On the up side, the mechanical exfoliation can operate entirely in ambient conditions. It is a fast and efficient scheme for producing small scale single-crystal samples which are sufficiently large, more than 5×5 μm, with relatively good optical and electronic quality for studying their fundamental properties and making one-of devices.

The mechanical exfoliation is fully compatible with an all-dry transfer procedure which does not involve solvents, enabling stacking monolayers one by one on top of each other and placing them at deterministic locations on arbitrary substrates. However, this comes with a cost of introducing unintentional strain and sometimes structural damage to the flake.

Another top-down approach originates from a chemistry lab. Extracting monolayers from the bulk is done by immersing the crystal is solution containing Lithium atoms[*10*]. Lithium atoms are small enough to penetrate the space between TMDs layers, therefore the bulk crystal becomes intercalated with ionic lithium species. Once heated, the solution expands and forces layers to disconnect overcoming the attractive, van der Waals force. As a result, the bulk explodes into thinner crystals, often monolayers, which can be extracted. Although the yield of monolayers is relatively high, the extraction of monolayers does not favour applications. Instead, Lithium intercalation becomes favourable when large amounts of monolayers are needed to be placed on an arbitrary substrate. Similar to the mechanical exfoliation, intercalation does not provide control over size and thickness. It is also expensive due to the high price of pure Lithium and the requirement of working in protected environment as Lithium reacts in ambient conditions.

This brief review of the top-down fabrication methods of 2D crystals would be incomplete without mentioning the concept of layer by layer removal. While the principle is straight forward its implementation is rather contrary to that. In layer-by-layer removal, the aim is to deliver localised amount of energy to the top most layer of the crystal which is high enough to break in-plane atomic bonds so that individual atoms and molecules disassociate from the bulk. The difficulty is in keeping the energy localised and low enough to avoid affecting the layer beneath which is the next in the queue. This was first achieved in 2012, with the heat generated by the scanning and focused spot of green laser[*11*]. Soon after, another way of reaching the same deterministic, layer-by-layer removal emerged using Chlorine assisted Argon plasma etching[*12*], as illustrated in Figure 3.1.2. This thinning method, although deterministic and capable of producing large monolayers, their optical quality requires further investigation. However, its impact on optical characteristics have not been investigated. This approach is likely to stay in the periphery of fabrication activities but perhaps might become popular as the concept is very attractive.

3.1.3 Direct comparison and summary of fabrication techniques

The previous sections demonstrated that the range of solutions for fabricating 2D crystals is very diverse, perhaps because so far there is not a one-size-fits-all scheme. Each fabrication technique has its strong and weak sides. The appropriate approach for producing 2D crystals is likely to be chosen according to a particular application and relevant constraints unique to the user such as time, price, equipment, quality, yield and control over size and thickness.

Despite its size limitations, mechanical exfoliation remains the cheapest and the easiest way to produce high quality monolayers. The order of favourite fabrication techniques might shuffle when research shifts from fundamental to applied physics. This shift is likely to favour the bottom-up fabrication schemes.

A good way to grasp the differences and limitations of the fabrication methods is via direct and comparison, as captured by Table 3.1.1.

	Bottom-up ↑	**Top-down ↓**
Scalable	Yes, technically possible Limited to ~100 μm equal-sided triangles ML crystals [*13*]	No, stochastic process hence intrinsically limited
Size of 1L	1 inch in diameter	3 - 100 μm
Uniform	multi domain crystal	Highly crystalline

Control over no. of layers	Yes	Generally no, but yes with post selection.
	Bottom-up ↑	**Top-down ↓**
Complexity	High	Low
Why complex and why not?	Ultrahigh vacuum, fine temperature control, long calibration period, requires highly skilled personnel.	Moderate resourced optical microscope and scotch tape, one-day training period. Ambient conditions, but for pristine sample inert environment and encapsulation is required [*14*].
Cost	Relatively expensive technology.	Cheap - ordinary microscope and scotch tape are enough.
Time	Slow	Fast for small samples, the larger the flake the longer it takes.
Suitable applications	All, but quality hindered by wet transfer techniques.	All, but limited by size and quantity.
Quality	Prone to defects and small domain size. Not as high as mechanically exfoliated.	Good enough for fundamental research and simple devices but not for commercial purposes.
Strain / roughness	Transfer technique, whether liquid or dry, is never perfect and it induces local strain. Flakes break, bend, fold, form wrinkles, and follow the roughness of the substrate.	
How easy and flexible to integrate?	Limited to the precursor substrate. Liquid lift-off and transfer techniques are essential to integrate flakes to devices which diminish the quality.	Suitable for all-dry, solvent-free transfer which is clean, precise, and flexible to where a monolayer can be placed.
Limitations	Not intrinsically limited. It requires sophisticated chemistry and engineering and is still challenged by defect control, uniformity and domain size.	Intrinsically limited by its stochastic principle, which means that larger samples (> 100 μm) become very time-consuming and impractical to fabricate.

Table 3.1.1 – A direct comparison between two leading approaches of fabricating monolayers of 2D crystals, bottom-up CVD and top-down mechanical exfoliation.

3.2 Mechanical exfoliation in-depth

In this section, I present a detailed description of mechanical exfoliation. This will show the ease of producing monolayers and the flexibility of integrating them into custom devices as well the intrinsic limitations and searching for possible ways to bypass them.

In the previous section, we learnt that mechanical exfoliation separates the bulk with the aid of mechanical forces due to the adhesive force of an adhesive tape which overcomes the van der Waals attraction between layers.

Mechanical exfoliation starts with commercially available bulk crystal. Its quality directly affects the yield of monolayers, their size and eventually the optical quality. Intuitively,

more defects mean the flakes are more prone to fracture due to lowered energy for dislocation to occur. The concentration of defects influences the optical quality of the semiconducting monolayers. Therefore, the source crystal needs to be chosen carefully.

There are several suppliers, making the choice difficult and ambiguous. It is often the case that conclusions about the crystal quality can only be drawn after the purchase by evaluating the exfoliation and PL characterisation. This is partly why some groups around the world shifted away from commercial crystals and instead producing their own bulk crystals, enabling feedback between the growth and the quality. Notably, the defect concentration of home-grown monolayers can be order of magnitude lower than those commercially available[*15*].

In this thesis, bulk crystal was purchased from three suppliers: nanoScience Instruments (product NS00182), HQgraphene and 2D Semiconductors. During the process of mechanical exfoliation, monolayers of WSe_2 from nanoSurf Intr. bulk happened to be rarer and smaller, up to 5×5 μm, than those from other companies which reached areas of up to 50×100 μm. Interestingly, all monolayers showed similar PL signal featuring delocalised two-dimensional neutral exciton (2D-X0), charged exciton (2D-XT) and broadband 'defect' band (see Appendix A).

Once one chooses the 'mother' bulk crystal, the next step is to reduce its thickness with the adhesive tape. The ordinary scotch tape, originally used for graphite, leaves behind large amounts of residues (i.e. glue) on the flake and on the substrate. Therefore, a weaker tape with low residue was used: Nitto tape (Nitto Denko Co., SPV 224P). The exfoliation procedure follows the steps outlined in the supplementary information of the all-dry transfer technique[*16*]. However, before thinning, the bulk crystal is transferred onto the Nitto tape with the following method. With tweezers, a small piece, around 3×3×0.1 mm is picked from the bigger bulk crystal and placed flat onto a strong scotch tape, the sticky part facing upwards. The scotch tape is anchored to the worktop by placing another stripe of the same tape across it. This is done to cover the sticky parts of the tape and to expose only the crystal. The crystal is then ready to be thinned down and picked up by the Nitto tape. This process can be repeated a number of times until there is nothing left behind. The Nitto tape is then brought into contact with the crystal. Using a cotton bud, a slight uniform pressure is applied. Finally, the tape is removed from the crystal by quickly pulling both ends of the Nitto tape upwards.

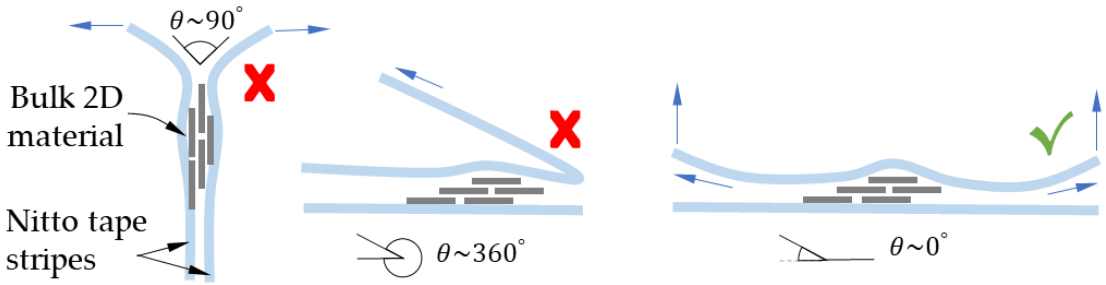

Figure 3.2.1 – Three geometries of exfoliating a 2D material using a Nitto tape. They differ from each other by the angle the tape creates with the respect to the bulk's plane. **(a)** In-the-air two-hands exfoliation and **(b)** worktop peeling create too large angle resulting in more fractured domains than **(c)** worktop vertical lifting where the angle is minimised promoting large domains.

The manner with which the tape is pulled proves to be important for the size of the bulk domains and therefore the size of monolayers. As shown in Figure 3.2.1, it is recommended that the angle between the crystal and the tape is kept to minimum. This can be achieved by moving both hands vertically upwards and keeping them close to the worktop surface. This prevents fracturing of the crystal into smaller pieces with each exfoliation attempt (eventually turning it into a powder). For example, if the Nitto tape is withdrawn by pulling it by only one end, the crystal gets exfoliated but it also bends and breaks along the perpendicular direction to the pulling. Intuitively, the aim is to keep the exfoliating force as vertical as possible minimising the shear forces which leads to big and flat domains. This practice became a global routine and it was implemented at any time when the exfoliation step took place whether onto a substrate or a viscoelastic polymer.

At this stage, it is worth considering what area of the tape will be taken by the crystal. From the practical point of view, the area of 1×1 cm square is sufficient to fully cover most substrates and viscoelastic stamps. From the statistical point of view, the more densely populated the Nitto tape, the more likely it is to attain the monolayer. After many exfoliations and many stripes of Nitto tape the original piece of the 'mother' crystal disappears from the worktop. It has been exfoliated onto the Nitto tape awaiting to be thinned down further.

The exfoliation process then continues with new and clean stipe of Nitto tape. As mentioned before, the same routine of bringing two stripes together and pulling them apart is employed – as fast and vertical as possible.

To decide how many times one should exfoliate and to know when to stop, the flakes on the Nitto are inspected by the optical microscope. The inspection step helps to optimise the flake thicknesses for the final exfoliation step before the searching for monolayers

begins. In the transmission mode, the microscope images indicate how thick the flakes are by looking at their colour. Large domains are recognised by large and uniform areas with the same colour. This is shown in Figure 3.2.2. As the flakes get thinner, the colours under the transmission progress from black to dark and light brown, green to dark and light grey. Although the colour code depends on the details of substrate and microscope due to interference effects. However, as long as the substrate has refractive index ~1.5 (of Nitto tape, Poly(vinylchloride) PVC), is homogenous and thicker than the wavelength of illumining light (> 0.8 μm) the colour code should not deviate much from what is presented here.

When the majority of the flakes on the Nitto tape show large domains in a bright brown colour and in any shade of green and grey, the tape is ready to be finally exfoliated onto the target substrate or the viscoelastic stamp. This prevents very thick flakes, which are unlikely to have monolayers attached to them to be transferred. Instead, if the initial conditions are right one should expect to find monolayers after first few, no later than after six attempts. Otherwise, the tape requires to be further exfoliated and thinned down.

The final exfoliation can be done on a Silicon substrate at which point the fabrication ends here and identification of monolayers takes over. The fabrication process continues

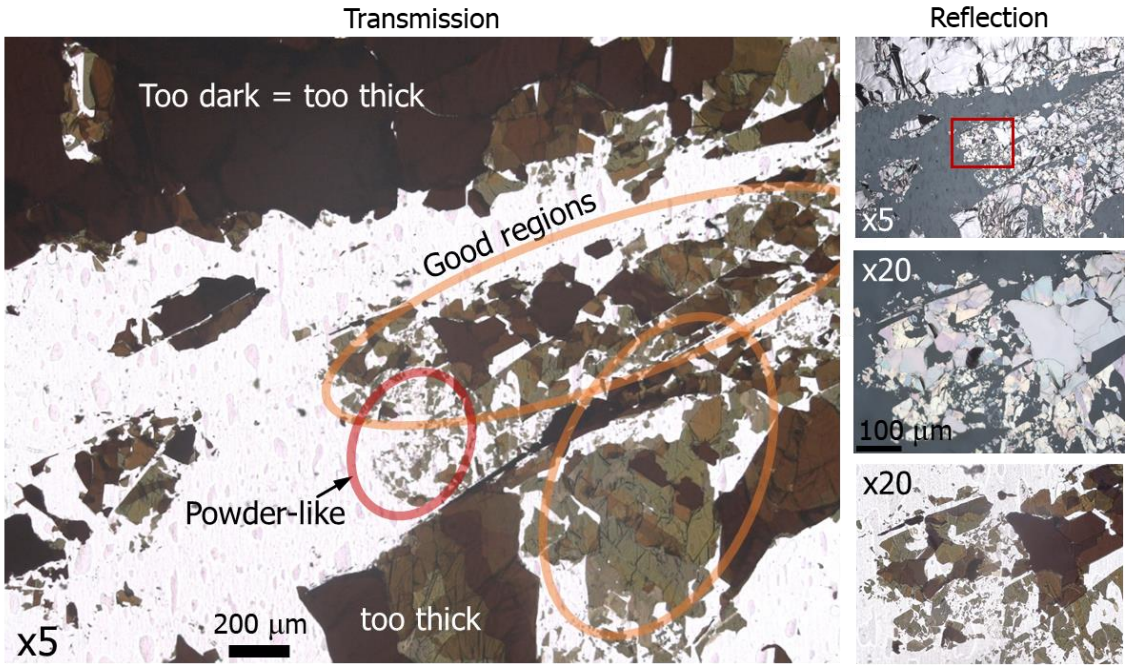

Figure 3.2.2 – An example of optical inspection of the thickness and size of pre-exfoliated flakes of MoS_2 on Nitto tape. The comparison between transmission and reflection modes show striking differences and the thickness can be much easier assessed in transmission mode. The images reveal regions of flakes that are too thick, sufficiently thinned down flakes, with big domains, and destroyed powder-like material.

for those who heat up the substrate in order to pick up the monolayers with a polymer to build heterostructures[*17, 18*], known as hot pick-up method.

Alternatively, if working with the all-dry transfer technique, the final exfoliation is done onto the viscoelastic stamp on which monolayers are identified. The use of stamps speeds up the process of fabrication by eliminating the step of cleaning the Silicon wafers after unsuccessful search for monolayers. It also enables deterministic positioning of the monolayer onto an arbitrary substrate or onto other previously transferred monolayer if a heterostructure is of an interest.

Either way, at this stage, the mechanical exfoliation is completed and the identification of monolayers is the next step in the fabrication process. The methods used to identify the thickness of 2D crystals will follow after the next section. In the next section, the statistical nature of the mechanical exfoliation is quantified with the aim to fabricate the largest monolayer possible in 3 days (21 hours).

3.2.1 Statistics of monolayer yield: number vs size and time

As it was mentioned short time ago, the mechanical exfoliation is an intrinsically stochastic process. This implies that the more exfoliating attempts the higher yield, more and bigger monolayers. This was put to the test by setting an aim to fabricate a 50×50 μm (2500 μm^2) monolayer of MoS_2. In order to arrive at statistical representation of the exfoliation process, each monolayer with at least 4×4 μm (16 μm^2) area was counted as it is sufficiently big area for confocal spectroscopy. Figure 3.2.3 displays the results from

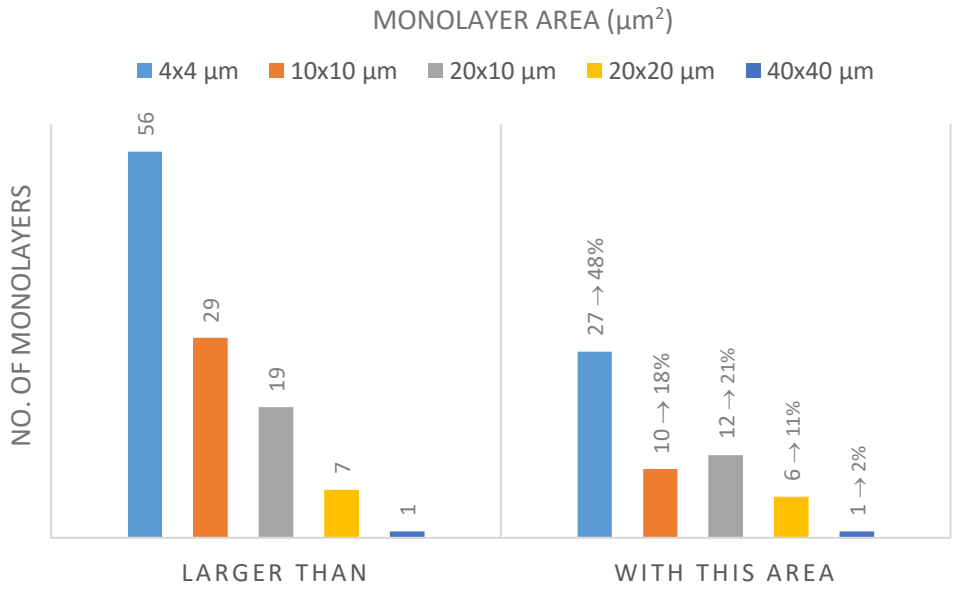

Figure 3.2.3 – The number of monolayers obtained after 21-hour exfoliation process using Nitto tape and viscoelastic polymer stamps. The height of the columns represents the number of monolayers and the colours their size accordingly to the legend.

a 21-hour exfoliation process during which the optical inspection was done on viscoelastic stamps.

As expected, the number of monolayers decreases dramatically with the monolayer area and the statistical analysis holds several interesting facts about the process. For instance, on average, it would take 22.5 min to fabricate a single flake with the area at least 16 μm^2 but only 2 out of 100 were larger than 1600 μm^2. It also took 1260 min to fabricate monolayers with the total area of around 9k μm^2, equivalent to a square with 0.095 mm sides, which also translates into the speed of fabrication of 7 μm^2 per min.

These results confirm that the mechanical exfoliation cannot possibly compete with any bottom-up fabrication method in a long run because it is slower and unpredictable. However, in the literature there are reported examples showing a significant improvement in the monolayer yield which extends much beyond to what is presented here.

Gold-assisted exfoliation comfortably reaches flake areas of 1000 μm^2, equivalent to 40×25 μm[*19*]. This method relies on the strong affinity of gold to chalcogen atoms. When in contact, gold atoms form a layer and bond covalently to the topmost layer of TMDs bulk. The strength of the covalent bonding can easily overcome the weak van der Waals interlayer attraction and separate exactly a single layer from the bulk. Overall, the method is attractive but also involves many fabrication steps (i.e. evaporating gold, a number of wet etching steps) which are likely to affect the quality. Although the quantum yield does not differ between gold-assisted and traditionally exfoliated samples suggesting that the new process is not intrusive hence there is no need to be concerned about the quality. However, it would be still insightful to perform comparison between PL emission between the two types of samples at cryogenic temperatures.

3.3 Getting the thickness right

Before the flake can be transferred and used for the optical characterisation and building heterostructures, its thickness needs to be confirmed. This can be checked in a number of ways. Broadly available methods include optical inspection, atomic force microscopy (AFM), Raman, and PL spectroscopies, and ellipsometry.

3.3.1 Optical inspection – contrast derived from Fresnel equations

The quickest of all identification techniques is optical inspection, which employs the absorption of the 2D crystals. The absorption increases which each additional layer. By looking at the difference between the light reflected or transmitted by the flake and the substrate, it becomes clear how many layers the flake consists of. This difference can be

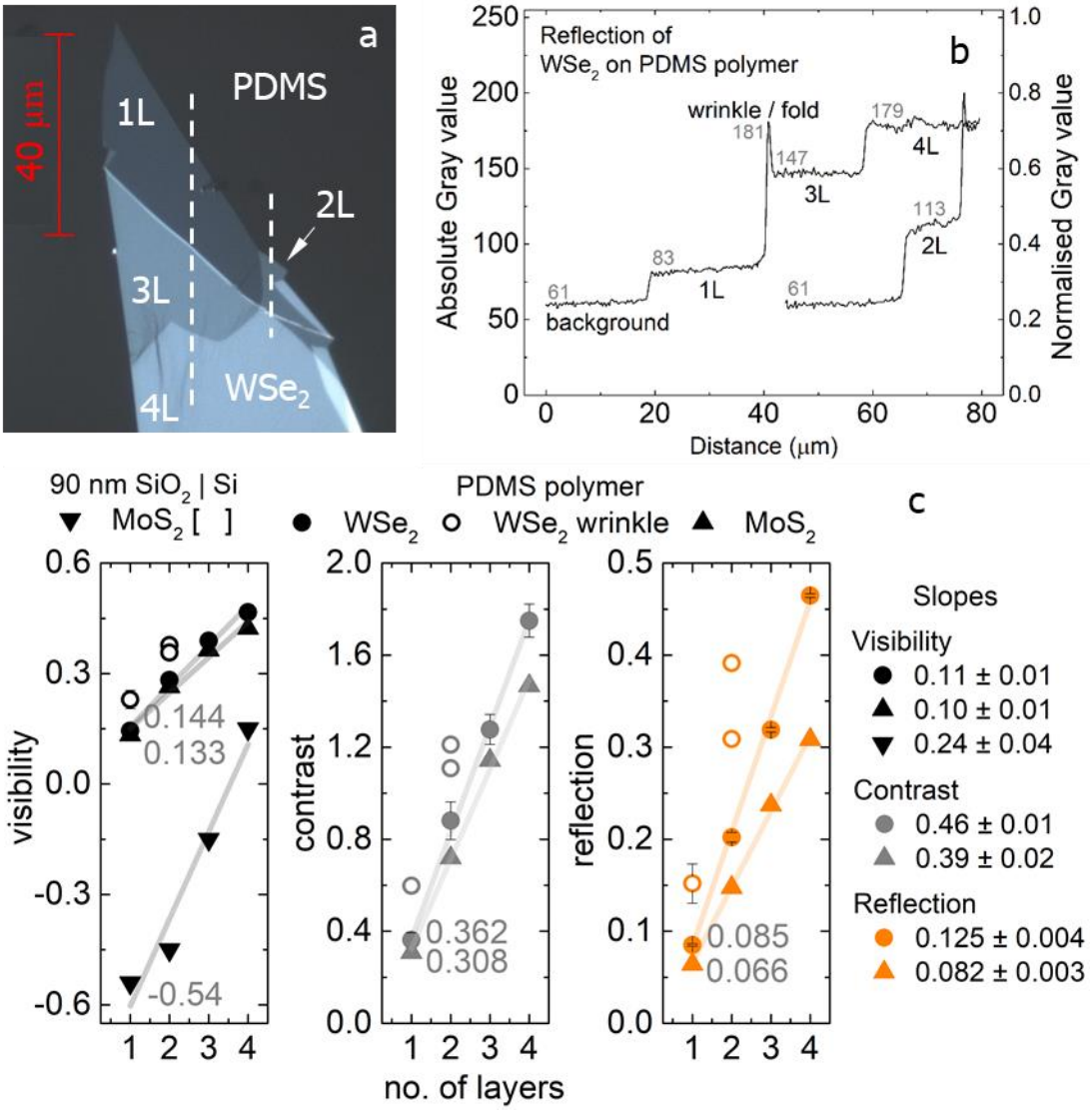

Figure 3.3.1 – **(a)** Optical image of reflected WSe_2 flake on PDMS polymer shown as an example of thickness identification using optical inspection. The image is white-light balanced and records all colour channels of the camera. Dashed lines indicate the sections used for the analysis. **(b)** Cross-sections marked in **a** where intensity is represented as grey value = $(G^2+R^2+B^2)^{0.5}$. Grey numbers are the mean values of each level. **(c)** Trends of three indicators – visibility, contrast and reflection relative to the PDMS polymer for WSe_2 and MoS_2. For the comparison, the graph includes the values for MoS_2 on Si substrate with 90 nm of SiO_2 layer for optimised visibility under monochromatic illumination of 450 nm [22]. Grey numbers are the extracted values for monolayers.

quantified as contrast, visibility or reflection (absorption). Unfortunately, in the literature these definitions tend to be used interchangeably. In this work, the following definition are used: Contrast = $(I_{substrate} - I_{flake}) / I_{substrate}$; Visibility = $(I_{substrate} - I_{flake}) / (I_{flake} + I_{substrate})$; Reflection = Normalised[I_{flake}] – Normalised[$I_{substrate}$], where *I* stands for intensity. All indicators should show a linear increase as a function of increasing number of layers. The identification process is shown in Figure 3.3.1. It starts with white-balanced optical image of reflected light from the flake acquired with an optical microscope (Leica type 301-

371.010). In this instance, the WSe_2 flake features layers from 1 to 4. As shown in Figure 3.3.1b, cross-sections reveal the values of intensity for each discrete thickness from which all indicators can be computed. These are displayed in Figure 3.3.1c for WSe_2 and MoS_2. Note there is no filter, the result is the integrated intensity over the entire range of the CCD. The intensity values are displayed as a grey value: a length of a vector with 3 colour coordinates (Green, Red and Blue) equal to $(G^2+R^2+B^2)^{0.5}$. Each channel can be extracted individually to seek enhanced contrast. For WSe_2 on PDMS, (with a 1.4 refractive index), this is not required in order to recognise monolayers because they show contrast of 0.36 and reflect up to 8.5% of light. However, this is not the case for other 2D crystals. For example, hexagonal boron nitride (hBN) reflects very little light and is virtually invisible to the human eye even when using the optimised substrate[*20*]. Improvement in the contrast can be further gained if the flakes are searched with a filter which selects a narrow bandwidth of light. For hBN, the best conditions are for 590 ± 5 nm where the monolayer shows 3% contrast.

As expected, all indicators (visibility, contrast and reflection) show linear trends in Figure 3.3.1c. The slope and the initial intercept for the monolayer are extracted. The values can be optimised further by utilising Fresnel equations. This set of equations describes how the light reflects and interferes with itself due to changes in the refractive indices in the substrate, which are smaller than the wavelength of light. An example of such optimisation is MoS_2 on Silicon wafer with the thickness of the oxide layer as a parameter. In this instance, the optimised thickness is 90 nm as shown in Figure 3.3.1c. Given the dielectric constants present in the stack, the most frequently used thicknesses of SiO_2 for MoS_2 and WSe_2 flakes are 90 nm and 270 nm[*21*]. With the right thickness of SiO_2 and sharply filtered illumination, the visibility of a monolayer can be improved more than 4 times, from 0.13 to -0.54[*22*].

Apart from uniform planes of constant colour and thickness, sometimes flakes feature wrinkles which appear as propagating lines. Undergoing the same analysis, as shown in Figure 3.3.1c, wrinkles score higher in all indicators than the planar regions, making it appear with a lighter colour which almost imitate the next thickness. Therefore, optical inspection is also a good indicator of the topography of 2D crystals.

The optical inspection is a very quick method which is solely sufficient to identify monolayers. However, this is only true when having the prior knowledge about how much light is reflected (absorbed) by the monolayer as one could not exclude finding flake with even lower contrast. When working with a new 2D material, other complementary

techniques are used to determine the number of layers. This is to 'calibrate' the microscope and the human eye with the contrast and colour of the particular monolayer. After other instruments confirm the thickness, optical inspection then can become the dominant tool in identifying the monolayers.

3.3.2 Raman resonances

Since the beginning, the Raman spectroscopy has been successfully and extensively used for indicating the quality and the thickness of 2D materials. The Raman spectrometer is designed to measure vibrational modes of atoms locked in the lattice. The flake absorbs light, usually green at 514 nm, which very quickly gets reemitted via a virtual, short-lived state at a slightly shifted wavelength. The difference between absorbed and emitted light gives rise to the Raman frequency (mode). Its energy signifies the manner with which atoms vibrate in the lattice. The Raman fingerprint is unique for each TMDs as it responds to the change in the thickness due to the difference in atomic masses between metal and calchogen atoms. However, all show two fundamental modes, out-of-plane A_{1g} and in-plane E^1_{2g}. Regardless of the material (i.e. WSe_2, WS_2, MoS_2, $MoSe_2$), when decreasing the number of layers the Raman modes shift in the same directions just with distinct slopes - A_{1g} towards lower and E^1_{2g} towards higher energies[*23*]. Therefore, the smaller energy separation between the modes the thinner the flake. As an example, Raman spectrum from a few layer MoS_2 flake is displayed in the Figure 3.3.2a. It features two modes with the separation of 24 cm^{-1} which confirms its multilayer thickness. The arrows above each peak indicate the direction and the relative strength (large vs small) of the trend while reducing the number of layers and the presence of the tensile strain (the compressive strain would shift modes in the opposite direction).

In order to determine the thickness using Raman spectroscopy, the literature provides that the mode separation of 18 cm^{-1} belongs to the monolayer MoS_2 and 21 cm^{-1} to the bilayer which is summarised in the table in Figure 3.3.2b. In practice, the distinction between monolayer and bilayer is not always clear. Figure 3.3.2c shows the Raman signal as the laser spot was scanned across the flake (acquired with Ranishaw inVia Reflex at 514 nm). At location no. 1, the separation between modes gives 19.18 cm^{-1} which is somewhere between single- and bi-layer fingerprints. This ambiguity it is likely to originate from the strain present in the sample influencing the measurement.

Raman modes show a different degree of susceptibility to strain[*24*]. Intuitively, the in-plane E^1_{2g} mode will be more susceptible to strain (-2.2 cm^{-1} per % strain) than the out-of-plane A_{1g} (negligible response to strain) simply due to the vector quality of strain

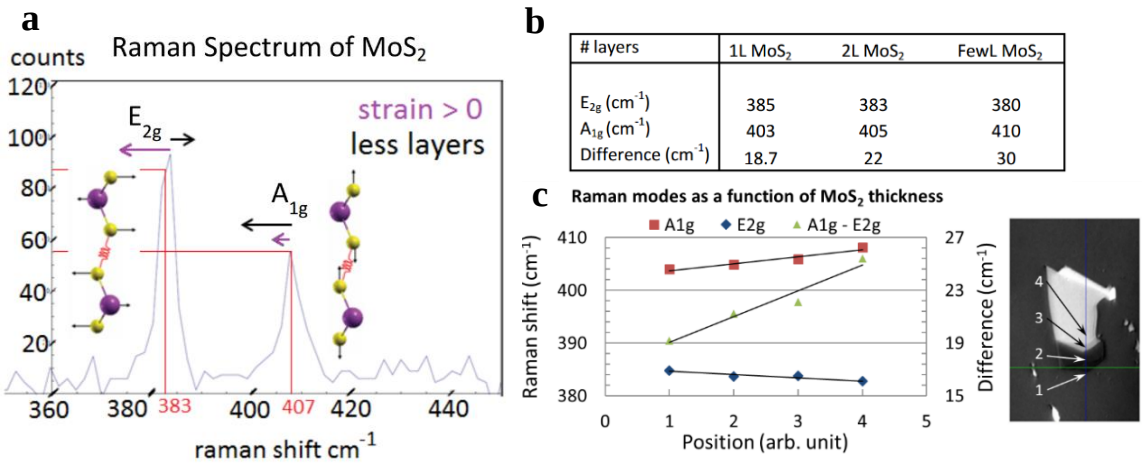

Figure 3.3.2 – **(a)** Raman spectrum from few-layer MoS_2 with arrows indicating shifts due to the layer number and strain. **(b)** Table featuring energies of modes for 1L and 2L MoS_2 from [24]. **(c)** Energies of modes acquired from 4 different positions from the flake displayed in the insert. The graph also plots the difference between modes.

which in addition is more likely to act in the directions within a horizontal plane of the flake than vertical. This means that the in-plane E^1_{2g} mode is not fit for indicating the number of layers and should not be considered at all. Therefore, instead of looking at the separation between the modes as literature suggests, a better indicator would be the position of the out-of-plane A_{1g} mode. This is because it exhibits larger sensitivity to the number of layers and smaller to the strain. Taking this into account, it is clear now that the flake at location 1 with A_{1g} = ~ 405 cm^{-1} is likely to be a bilayer, as was later confirmed by PL spectroscopy.

Overall, the Raman spectroscopy does not require sophisticated equipment neither large financial investments and can be built using cage-based optics mounts and components (i.e. Thorlabs). Furthermore, the high laser intensities in mW range make it an intrusive identification tool for non-encapsulated monolayers[*25*]. The results produced by this apparatus become clear and useful only if the inspection includes the complete data set with the trend from thicker parts of the flake. Similar to optical inspection, on its own, the Raman spectroscopy is not sufficient to provide the ultimate confidence in diagnosing the thickness of the samples.

3.3.3 Atomic force microscope (AFM)

The atomic force microscope is a scanning probe which measures the topography of the surface with sub-nanometre vertical resolution via detecting short-range attractive van der Waals forces. These forces are detected by a very sharp tip, 10 nm in radius of curvature, fabricated on a cantilever which is brought very close to the surface of the specimen. In the tapping mode, the entire cantilever is driven at the cantilever resonant

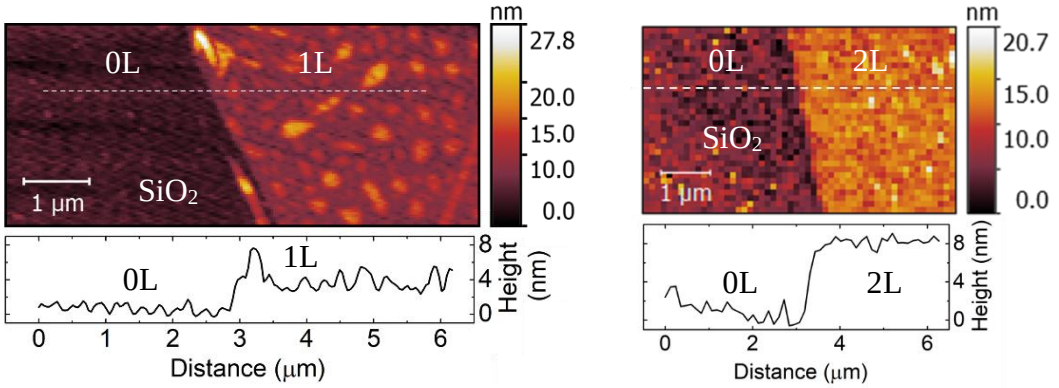

Figure 3.3.3 – Tapping mode AFM scans of monolayer and bilayer WSe_2 on SiO_2 substrate where each white dashed line represents the place of the cross section. The cross sections are displayed below each map and read 4 nm for monolayer and 8 nm for bilayer WSe_2.

frequency. To record the position of the oscillating cantilever, laser light is sent on the top of the cantilever where it reflects towards the face of a photodiode which measures the displacement. While maintaining the constant attractive force between the tip and the surface, the topography of the specimen determines the position of the laser light on the detector, hence generating 3D data. With sub-nanometre vertical resolution, AFM is well-equipped for measuring the thickness of 2D materials down to the single layer limit which is around 0.7 nm for 3-atom thick TMDs. However, working with AFM is nontrivial. The readings of the cantilever are highly influenced by the predefined parameters of the apparatus, in particular the peak force setpoint[*26*] and the free amplitude[*27*]. For instance, in the case of peak force setpoint that is too small, the measured height is much greater than the actual size because of too little pressure applied by the cantilever. Without the adjustment, the heights of pre-identified monolayer and bilayer of WSe_2 are around 4 nm and 8 nm as shown in Figure 3.3.3. Although this effect can be accounted for, the AFM also requires the prior knowledge from other apparatus to fully and without unambiguity characterise the 2D monolayers. However, once calibrated, the AFM is very powerful and non-intrusive tool which can be effectively used not only to identify the number of layers but also to measure very fine topographies revealing structures such as nanobubbles and wrinkles which are commonly found in mechanically exfoliated flakes, as shown in the same figure.

3.3.4 Photoluminescence (PL)

Photoluminescence (PL) occurs when a semiconducting specimen absorbs the energy of incident light and, as result of light-matter interaction, the specimen emits photons. The dynamics of this process involve an electron being promoted from the valence to the conduction band, creating a positively charged particle in the valence band called a hole.

The promotion of electron (and the creation of hole) occurs when the energy of light exceeds the optical bandgap of the material for which the absorption is the strongest. Subsequently, both particles undergo relaxation mechanisms during which they interact with the lattice for example via scattering events, until they reach their lowest energies available. The electron-hole pair can be bound together by the Coulomb force, creating a new quasi-particle with renormalized energy called an exciton. Subsequently, a spontaneous and radiative electron-hole recombination takes place, producing a photon with the energy equal to the size of the bandgap, renormalized by the exciton binding energy. This recombination is favourable in direct bandgap semiconductors, where the global minima of electron and hole dispersions align in momentum. This is not true for indirect bandgap semiconductors, where the bands are not aligned and for recombination to occur an extra momentum input from phonons (which happens to be very inefficient process) is required. The distinction between indirect and direct semiconductor makes the PL the most reliable indicator of the thickness. This is because the dispersion of W and Mo based TMDs goes through this exact transition between mono and bilayer. Therefore, the PL intensity from MoS_2 monolayer was measured to be 1000 times brighter than from the bilayer[*28*].

Figure 3.3.4a,b show unmistakable difference in PL response from mono- and bi-layer WSe_2 at room temperature and at 4K, respectively where the intensity difference is significant. Due to quantum confinement and Coulomb effects, PL both samples emit at distinct wavelengths, as indicated in Figure 3.3.4a,b. These differences become very useful when mapping few micron sized multi-layered samples to confirm the regions of mono- or bilayer flakes like one shown in Figure 3.3.4c. While at room temperature there

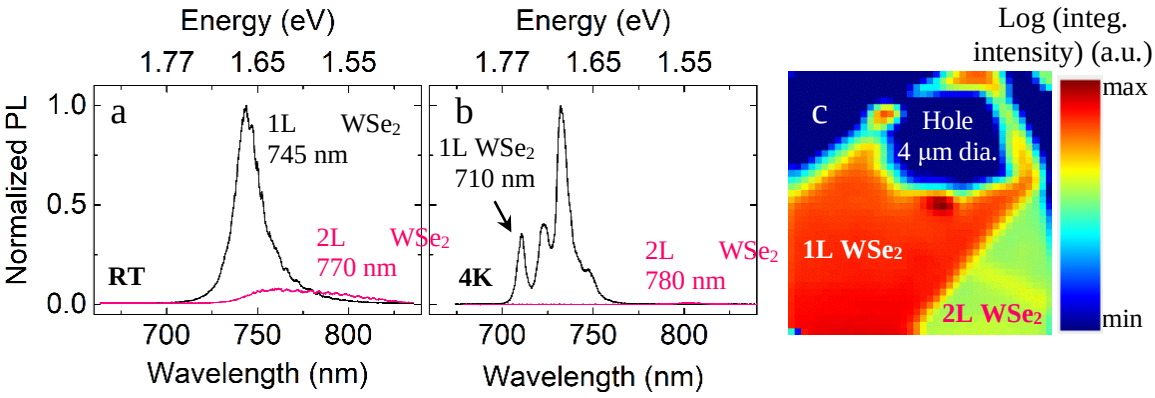

Figure 3.3.4 – PL spectra of 1L and 2L WSe_2 at **(a)** room temperature and **(b)** 4K. **(c)** Spatial map of PL integrated intensity shown in logarithmic scale, taken at room temperature revealing locations of bright 1L and dim 2L WSe_2. The dark circle is the location of an etched hole where the flake buckled altering the focal plane of the sample.

is a single peak observed, spectrum at 4K exhibits multiple-peak emission which will be described in Chapter 4.

The difference is the energy and the intensity between mono and bilayer is so large that it could not be possibly shifted by the strain even when deliberately applied. The strain variations in samples on the flat is negligible with the respect to the spectral separation between the emissions. Only very large strains, more than 1% can shift the emissions so they start to mimic one another [*29*].

In essence, when it comes to confirming the number of layers of semiconducting 2D materials, PL spectroscopy is the most trusted tool. However, its power is limited to semiconducting samples, so other 2D materials like graphene or hBN require support from other complementary techniques in determining the number of layers.

3.3.5 Ellipsometry

Although ellipsometry was not used in the context of this thesis and is not widely mentioned in literature, it may soon become a widely used tool because it provides an approach to characterise devices such as complicated multi-layered heterostructures without prior knowledge apart from refractive indices of the 2D materials.

The reason for the modest interest in ellipsometry is probably due to the lack of a commercially available, easy-and-ready-to-use apparatus with sufficient resolution to work with 2D flakes of modest size. Traditional versions of ellipsometers lack imaging capabilities and are designed to work with laterally infinite thin films of dielectric materials, very different to the localised nature of exfoliated flakes with only tens of microns across in size.

The reason for optimism is that ellipsometry has been used in the context of 2D crystals[*30*] and it shown to be a very powerful and versatile tool which does not restrict the choice of the crystals. This is because it utilises fundamental properties of light expressed by Fresnel equations - the same set of equations which drives the optical identification and is used to optimise the contrast against the substrate. Ellipsometry measures the change in intensity and polarisation of reflected light as a function of wavelength and the angle of reflection. Given only the dielectric constant of the thin material, the ellipsometer provides a value of the thickness with angstrom precision. With increased lateral resolution to the order of 1 μm and imaging capabilities, ellipsometry can be well suited for 2D identification. One such system currently available is Accurion's imaging ellipsometer (product no. nanofilm_ep4). Imaging ellipsometry

provides unique and far-reaching advantages which can fill in gaps and perhaps become more reliable than other identification methods.

3.4 The principle of all-dry viscoelastic transfer - fast vs slow.

The all-dry viscoelastic transfer technique enables placing monolayers on arbitrary substrates at deterministic locations with arbitrary orientation. It has been developed to eliminate the sacrificial layer required in wet chemistry techniques. Eliminating the solvent broadens the range of applications for the transfer. For example, a wet transfer on a substrate with holes becomes very challenging due to capillary forces associated with the solvent. Moreover, the solvent can introduce contamination. On the other hand, such transfer onto the holes is not an issue for the all-dry viscoelastic transfer because it solely relies on mechanical forces of the viscoelastic polymer and the relative adhesive forces.

The working principle of all-dry transfer is based on the properties of the viscoelastic polymer. Once in contact with the substrate, the aim of the polymer is to regulate adhesive forces between all interfaces within the 3-layer system comprising of the substrate, the monolayer and the polymer itself. The type of polymer is carefully chosen so that the adhesive forces can be altered and controlled when switching between pick-up and printing regimes. If the polymer is viscoelastic, these regimes can be accessed by adjusting the speed of withdrawing the polymer from the surface of the substrate - slow for printing, fast for the pick-up, as shown in Figure 3.4.1. Viscoelasticity describes the unusual rheological behaviour of a non-Newtonian matter which reacts like a solid under quick force impulses and more like a liquid under slowly acting forces[*31*]. The viscoelastic polymers used in the transfer were made of polydimethylsiloxane (PDMS)

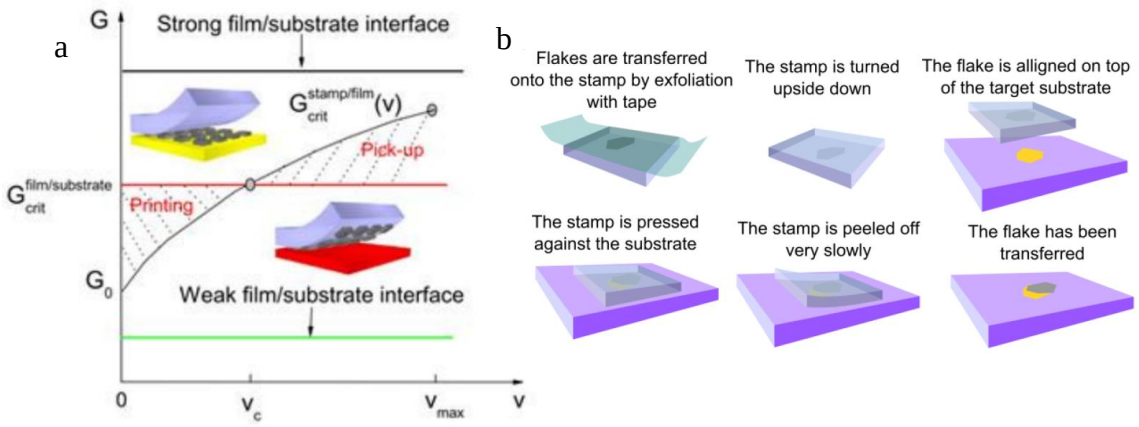

Figure 3.4.1 – **(a)** The principle of soft lithography - speed selective pick and place scheme. Energy release rates (G) are shown as a function of stamp velocity (v). Vc marks the intersection of energies and the boundary between printing and pick-up. **(b)** Illustration representing each step of the all-dry transfer technique. Figure **a** was adapted [29] and **b** from [16].

and sourced from Gelpak (product no. Gel-Film® WF ×4 6.0mil). They are thin films which are easy to handle and come with different adhesive strengths so they are strong enough to get well-attached to a glass slide which is used for the transfer.

Figure 3.4.1 illustrates the principle of the transfer. It plots the surface energy, *G*, between flake-substrate and polymer-flake as a function of speed of the polymer withdrawal, *v*. Given both contrasts in the surface energy, the speed invariant *G*(flake-substrate) and the speed dependent *G*(polymer-flake)(*v*), the graph features their intersection which defines two distinct regimes – printing and pick-up. The choice of substrate and polymer engineers the adhesion by effectively moving the red line up and down the graph and changing the slope of the speed dependent surface energy. This shows that the role of the polymer is not absolute in controlling the transfer. In two contrasting scenarios the balance in the surface energies between the interfaces can be swayed to one or other extreme by the substrate. With too strong flake-substrate interface, the flake always gets printed; with too weak, the flake always stays on the polymer. While changing the substrate in order to influence the relative surface energy is not an option, surface functionalization could become useful. This is when the surface is subjected to a chemical treatment which aims to increase its adhesion, for example, by populating the surface with single molecules which will bond covalently to the flake and the substrate simultaneously. The Figure 3.4.1b shows the step-by-step procedure which realizes the working principle of the viscoelastic transfer. It starts from the mechanical exfoliation on the PDMS stamp and identification of monolayers. Then the monolayer is flipped, aligned with the target, and brought in contact with the substrate. By peeling the polymer slowly, the monolayer is released and adheres to the target completing the transfer. Furthermore, although not implemented during this thesis, the temperature of the substrate can be easily used as another tuning knob which alters the balance to favour the printing or pick-up regime. Similar to the speed of peeling of the polymer, the elevated temperature helps to lower the surface energy of the substrate and promote the pick-up. Repeated a number of times, the heating control allows assembling heterostructures on the polymer, instead on the substrate[*32*].

3.4.1 The apparatus

In the lab, the experimental setup transferring monolayers from the viscoelastic polymer onto a substrate contains a microscope and two separate holders, one for the substrate and one for the glass slide which holds the monolayer on the polymer. The Figure 3.4.2

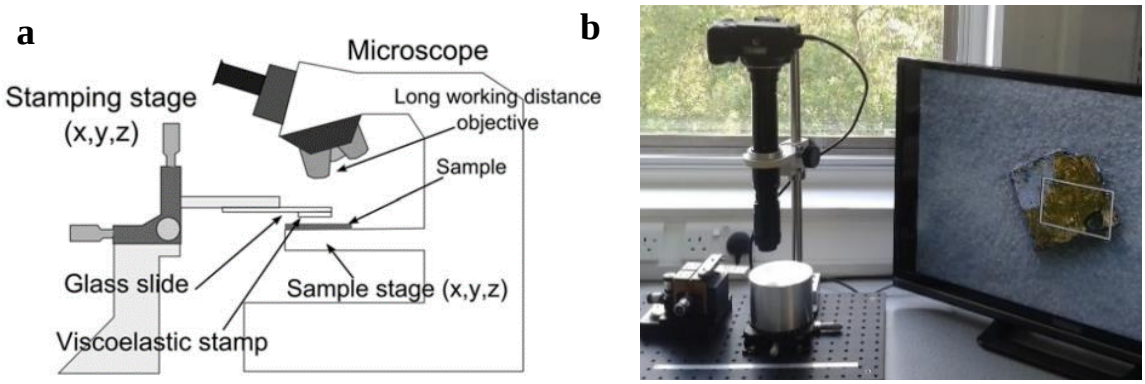

Figure 3.4.2 – **(a)** Illustration showing the schematics of all-dry transfer consisting of an optical microscope, sample and substrate holders where each can be moved in all 3 directions. **(b)** The all-dry transfer setup in the lab which mirrors the all components from **a**. Figure **a** was adapted from [16].

displays the apparatus and its simplified representation. A complete list of components can be found in the supplementary information of [*16*].

The microscope was assembled from components purchased from Thorlabs and Edmunds Optics. Apart from essential elements of any microscope such as white light source, imaging camera, screen and adjustable focal plane the key feature of this microscope is the smoothly adjustable magnification. The magnification starts at X2.3 and ends at X28. This gives the range of resolution of imaging between 9 μm and 1.66 μm and diagonal field of view between 4.75 mm and 0.4 mm (with 4:3 screen ratio). The working distance of 3.7 cm is long enough to accommodate for the imaging of the substrate through the glass slide and the polymer which is the crucial feature in deterministic positioning of monolayers.

Owing to the large field of view, imaging with small magnifications becomes very helpful in locating the monolayer which are previously identified by the contrast using more suited optical microscope. The large field of view is also essential in assessing the velocity (the direction and the speed) with which the polymer touches the substrate. The behaviour of the polymer during the transfer will be explained in detail in the following section.

On the other hand, the large magnification is particularly needed for aligning the monolayer to the substrate's topography or to another flakes. Because exfoliated monolayer regions occur over micrometre sizes, a microscope resolution of few microns is sufficient to assemble heterostructures. To align the substrate with the sample with high precision, both holders are free to independently move but each in a slightly different way. The substrate is anchored to the table, but can move in the xy plane with micromanipulators and manually rotated. The specimen holder can move freely and coarsely by hand and fine displacement in all three (xyz) directions is also provided by

micromanipulators. The micromanipulators have a travelling range of 13 mm, can be coarsely moved by 500 μm per revolution and ultimately provide resolution of 5 μm. The substrate is attached to aluminium cylinder with a double-sided sticky tape. Its height is fixed to the height of the glass slide holder. The specimen holder is designed to hold one end of the glass slide in-between two sliding cage plates. Another end with the polymer faces downwards and is positioned above the substrate with the micromanipulators. The holder can also control the tilt angle. The tilt is gauged by a small, air bubble leveller placed on the glass slide.

Next, I will describe the transfer process.

3.4.2 The procedure

Before the transfer begins, flakes are exfoliated onto the PDMS stamp which rests on the glass slide. Next, the PDMS stamp is scanned for monolayers with a suitable optical microscope to record their locations. Finally, the monolayer is ready for the transfer by flipping it to face the substrate and loading it to the holder with its tilt minimised using the air bubble level. The substrate is attached with a double-sided tape. The microscope camera takes live images of the substrate surface and the target location is selected with micromanipulators.

Now the monolayer is brought above the substrate and under the microscope light. The focal plane is adjusted at the flake on the PDMS stamp. The monolayer is located and roughly aligned with the target location using a marker on the screen. Because the glass slide and the polymer are transparent, the substrate can be imaged by changing the focus plane. The glass slide is lowered while the monolayer comes towards the focus until the polymer touches the substrate. As it happens, the position of the monolayer with respect to the substrate can be fine-tuned. While the PDMS is in contact, the fine-tuning generates the shear, which, if too large might fracture the monolayer during the withdrawal of the polymer. Furthermore, the tilt, although minimised, is never practically zero and it is very unlikely that the monolayer will be the first to touch the substrate. Again, if the tilt is too large it becomes a significant source of unwanted shear.

If the polymer approaches the target monolayer too slowly, the angle between the polymer and the substrate is too large. In this circumstances the transfer is significantly influenced by large in-plane, shear forces that lead to wrinkling and even the fracturing of the sample. Although, in most cases the shear is unwanted effect, in some it could be rather seen as a

tool to create locally strained regions and termination which in fact induces single quantum emitters in 2D semiconductors [*33*, *34*].

In order to minimise the tilt, the speed at which the PDMS film approaches the monolayer is monitored and, if necessary, altered. Each alteration involves an attempt peeling off the PDMS and changing the angle of approach with the tilt stage. This procedure is not only used to minimise the tilt (hence the shear) but also it is a good moment to change the direction from which the PDMS approaches the monolayer altogether.

The direction is a significant factor in the success rate of the transfer because monolayers tend to be attached to thicker parts of the flake and these are more hesitant to adhere to the substrate. Therefore, as illustrated in the Figure 3.4.3, it is recommended that the thicker part is printed first because if it is transferred than it is likely that the attached monolayer will do the same. However, this rule becomes disputable and even irrelevant when the thicker part is uniformly flat, thin (up to 20 layers), compact and comparable in lateral size to the monolayer. Then slowly peeling off the PDMS (in any direction) should lead to the successful transfer.

This implies that in the all-dry transfer technique, the shape and the thickness of the flake containing the monolayer becomes a deciding parameter on how challenging it is to transfer it. Therefore, to select an easy-to-transfer flake and increase the success rate, the optical identification not only involves recognising protruding monolayers but also judging the circumstance of the monolayer.

Figure 3.4.3 illustrates factors, recommendations, and signs of a successful and unsuccessful transfer. The important qualities are monolayer geometry, colour behind the polymer, shape of the polymer and the relative size and thickness. The Figure 3.4.3 also shows examples of flakes successfully transferred with the direction of polymer withdrawal marked on the picture. It also includes monolayers not suitable for the transfer due to severe corrugations, which can prevent the transfer or create extensive wrinkling which can fracture the monolayer.

After selecting the direction of PDMS approach and after few iterations towards minimising the tilt, it is decided that the “front” of the PDMS stamp eventually goes through the monolayer, forcing it to make its first contact with the substrate. The further the PDMS front travels beyond the flake, the larger the pressure on the flake. Intuitively, keeping the pressure to a minimum is less intrusive for the monolayer. Practically, the pressure generated by few hundreds of micrometres overrun are sufficient for most

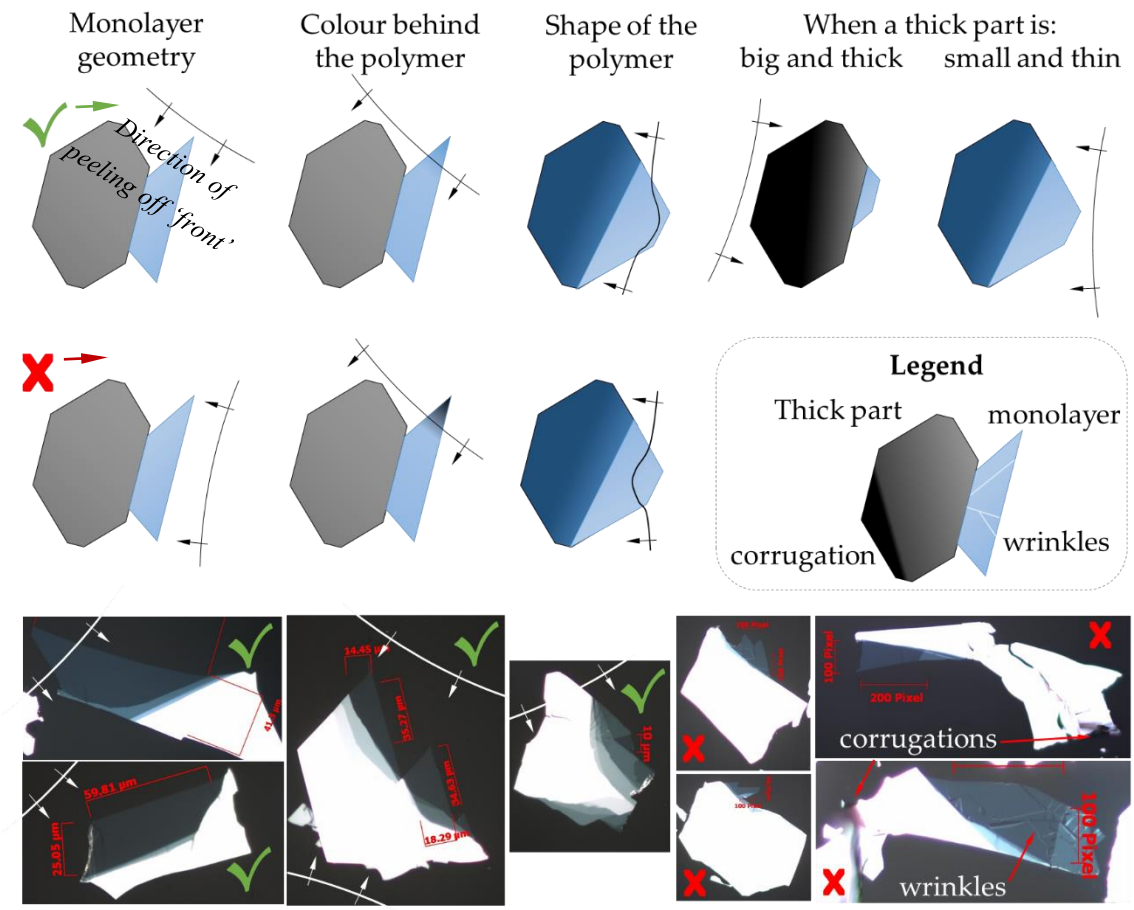

Figure 3.4.3 – Summary of scenarios which occur during the all-dry transfer of a 2D flake. Also, recommendations for and signatures of a successful and unsuccessful transfers displayed in 1st and 2nd rows, marked with green tick and red X respectively. All organised by 4 categories: monolayer geometry, colour behind the polymer, shape of the polymer and the relative size and thickness. Real life examples might consist of a combination of all 4 categories. On the left of the 3rd row, images of suitable for the transfer candidates with marked direction of polymer withdrawal. On the right, unsuitable candidates due to circumstances like severe corrugations and extensive wrinkling.

transfers. However, if the monolayer is subjected too much pressure, the monolayer exhibits large areas of densely populated nanometre-sized bubbles which are created in the response to a sudden release of strain during the peeling off stage [16]. From this point, the PDMS film is pulled very slowly upwards while the velocity of the peeling is monitored. As illustrated in Figure 3.4.3, a good indicator of the transferred flake is when its colour remains the same beyond the PDMS front. If unsuccessful, the flake turns darker and starts pulling other parts of the flake with it much quicker than the PDMS front travels. Another good indicator is the shape of the withdrawing PDMS front between the substrate and the flake. It is also a good sign if the PDMS travels slower on the flake comparable to the rest of the substrate which in result makes the line look slightly convex.

However, if the transfer presents difficulties, the last two resources to increase the odds involve elevating the temperature of the PDMS or applying a small amount of shear. The former is simply done by exposing the glass slide to a heat gun for a minute so the PDMS becomes more fluid-like, benefiting the printing regime. The latter is done by moving the glass slide in-plane, towards the direction of the PDMS propagation. The additional shear component changes the direction of the pulling force to reduce the upward contribution promoting the adhesion to the substrate.

Moreover, the same shear could be implemented in another context. If the flake is applied in the perpendicular direction to the propagation of the PDMS, the shear is likely to lead to wrinkles and corrugations, and in the extreme case, fracture along the line of the propagating PDMS. This can be another useful technique to strain the flakes (on purpose) in order to create local strain gradients across the sample alongside transferring flakes onto pre-stretched[*35*] or pre-patterned[*36*] substrates.

The capability of all-dry transfer cannot be better represented than by showing examples of transferred monolayers and fabricated devices.

3.4.3 Examples of devices

Pictures of fabricated samples in Figure 3.4.4 reflect the flexibility and practicality of the all-dry transfer technique. The summary also showcases deterministic placement and

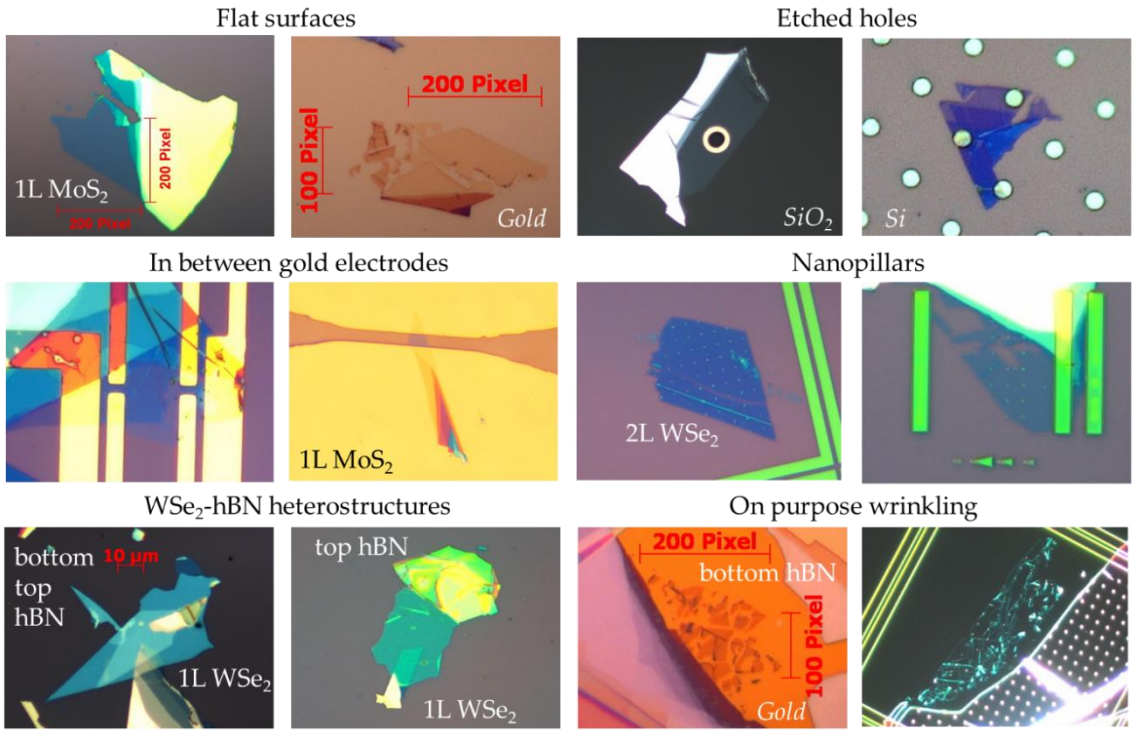

Figure 3.4.4 – Variety of examples of fabricated samples using the all-dry transfer technique which include flat and structured surfaces, heterostructures and on purpose creation of local strain and flake terminations.

compatibility with custom substrates such as dielectric and metal surfaces, pre-patterned structures like etched holes, gold electrodes and nanopillars. The all-dry transfer procedure also enables heterostructures and creating wrinkles and terminations on-demand due to the excess of applied shear.

Overall, the all-dry transfer process is a fast (lasting up to 30 min) and reliable (almost unity yield) procedure where the success rate is dependent on the suitability of chosen flake and the complexity of the substrate. Being solvent-free expands opportunities for the transfer and eliminates contamination. For these reasons, the all-dry transfer procedure paired up with the mechanical exfoliation is likely to remain widely employed fabrication method for devices based on 2D materials. However, its pressure-driven nature also introduces new threats of inducing highly strained topographies like bubbles or wrinkles, which in some context can be seen as an advantage. Moreover, it is widely recognised, but not necessarily studied in-depth, that the polymer-assisted transfer carry a degree of contamination. This becomes visible only after assembling heterostructures, as the contaminant is captured in-between layers and forced to cluster into microscopic bubbles due to the van der Waals interlayer attraction.

3.5 Summary, lessons learnt and future prospects

3.5.1 Fabrication overview

In the beginning of the chapter, a broad overview of fabrication methods was presented to appreciate the fast-growing, thriving and vast field of 2D material with the desire for a high volume of high quality monolayers yet to be satisfied. Without a clear winner, the fabricator of monolayers will choose one particular method over another according to the balance between available resources such as time, price and equipment and returns in the form of quality, yield, size and control over the thickness. Taking all into consideration, it seems that the fabricator is more likely to lean towards mechanical exfoliation as it provides the best quality of samples on the market and it is the cheapest and the easiest method available. However, this may not last because it is likely only a matter of time when bottom-up fabrication will outperform the top-down methods.

3.5.2 Mechanical exfoliation

The next section thoroughly presented the mechanical exfoliation to shine light on the procedure and its limitations. It was recognised that although mechanical exfoliation is sufficient for producing monolayers for spectroscopic investigations, it also comes with the major drawback of being an intrinsically size-limited method. It has been shown that producing monolayers larger than 400 μm^2 is very time-consuming. One could fairly state

that, in its current form, mechanical exfoliation is more an art than a purely scientific method. This is because its outcomes are changeable, unpredictable and user-dependent despite attempts to maintained identical procedures. The layer by layer removal and innovative methods like gold-assisted exfoliation can be seen as attempts to bypass these limitations and turn mechanical exfoliation into well-defined procedure with deterministic and large-area yield. However, the quality of samples made with these methods requires further development.

3.5.3 Characterisation tools

In addition to fabricating monolayer of 2D crystals, this chapter introduced characterisation tools including optical inspection, Raman spectroscopy, AFM, PL and ellipsometry. These sections provided in-depth analysis and discussion on their usefulness in identifying the thickness of 2D crystals down to the monolayer level. The considerable number of characterising tools claiming to be suitable for identifying the thickness of atomically thin 2D materials certainly gives an impression of overabundance. However, not a single technique has shown to be completely self-sufficient. Each has had its own shortcomings and artefacts. When working with direct bandgap semiconductors the best choice of diagnostics is photoluminescence. In fact, combined with optical contrast imaging, PL provides a robust toolbox for this thesis. It has been also stated that new imaging ellipsometry might become a sought after diagnostics tool for 2D devices due to its commercial availability and the suitability specially adjusted for needs of 2D identification. However, above all, it is always good practice to use a selection of tools that complement each other. This is especially relevant when assembling 2D heterostructures. The same set of tools allows obtaining a comprehensive view on the intrinsic behaviour of fabricated devices and on the factors influencing their performance like contamination and local strain.

3.5.4 Dry viscoelastic transfer

The working principle of viscoelastic transfer was explained with the aid of relative surface energies between two interfaces in the three body system consisting of the viscoelastic PDMS polymer, the monolayer and the substrate. The relationship between two interfaces defined regimes for printing and pick-up which could be experimentally accessed by slow and fast peeling of the polymer. The role of substrate and polymer were recognised and methods to influence their surface energies were mentioned. Empirical recommendation for the successful transfer were given.

The chapter also presented the experimental setup which enabled the all-dry viscoelastic transfer as well as examples of fabricated samples showing a range of applications. In the context of the experimental setup presented in the thesis, further and obvious ways for improvements would include (i) implementing more sophisticated and more local temperature control than using a heat gun, (ii) eliminating the double-sided type and replacing it with vacuum-based fixture, (iii) automating the transfer to access slow speeds of the peeling off, (beyond human capability and patience), and (iv) perhaps automating the searching for the monolayers with a scanning optical microscope programmed to recognise their contrast. Furthermore, in order to combat bubbles and the contamination one could seek improvements in searching for cleaner, more viscoelastic and more temperature resistant polymer. This would promote reaching the printing regime more promptly. Currently used modifications are poly(methyl-methacrylate) (PMMA) substitution[*18*] or the addition of polycarbonate (PC) on the top of the PDMS film combined with the hot pick-up technique[*17*],[*32*].

3.6 References

1. S. Bae *et al.*, Roll-to-roll production of 30-inch graphene films for transparent electrodes. *Nature Nanotechnology* **5**, 574 (2010).

2. G. R. Bhimanapati *et al.*, Recent Advances in Two-Dimensional Materials beyond Graphene. *ACS Nano* **9**, 11509-11539 (2015).

3. R. Dong, I. Kuljanishvili, Review Article: Progress in fabrication of transition metal dichalcogenides heterostructure systems. *Journal of Vacuum Science & Technology B, Nanotechnology and Microelectronics: Materials, Processing, Measurement, and Phenomena* **35**, 030803 (2017).

4. S. Chen *et al.*, Millimeter-Size Single-Crystal Graphene by Suppressing Evaporative Loss of Cu During Low Pressure Chemical Vapor Deposition. *Advanced Materials* **25**, 2062-2065 (2013).

5. C. Huang *et al.*, Lateral heterojunctions within monolayer MoSe2–WSe2 semiconductors. *Nature Materials* **13**, 1096 (2014).

6. Y. Chen *et al.*, Tunable Band Gap Photoluminescence from Atomically Thin Transition-Metal Dichalcogenide Alloys. *ACS Nano* **7**, 4610-4616 (2013).

7. H. J. Liu *et al.*, Molecular-beam epitaxy of monolayer and bilayer WSe2 : a scanning tunneling microscopy/spectroscopy study and deduction of exciton binding energy. *2D Materials* **2**, 034004 (2015).

8. C. R. Serrao *et al.*, Highly crystalline MoS2 thin films grown by pulsed laser deposition. *Applied Physics Letters* **106**, 052101 (2015).

9. K. S. Novoselov, A. H. C. Neto, Two-dimensional crystals-based heterostructures: materials with tailored properties. *Physica Scripta* **2012**, 014006 (2012).

10. V. Nicolosi, M. Chhowalla, M. G. Kanatzidis, M. S. Strano, J. N. Coleman, Liquid Exfoliation of Layered Materials. *Science* **340**, (2013).

11. A. Castellanos-Gomez *et al.*, Laser-Thinning of MoS2: On Demand Generation of a Single-Layer Semiconductor. *Nano Letters* **12**, 3187-3192 (2012).

12. T. Lin *et al.*, Controlled Layer-by-Layer Etching of MoS2. *ACS Applied Materials & Interfaces* **7**, 15892-15897 (2015).

13. X. Wang *et al.*, Chemical Vapor Deposition Growth of Crystalline Monolayer MoSe2. *ACS Nano* **8**, 5125-5131 (2014).

14. A. P. Rooney *et al.*, Observing Imperfection in Atomic Interfaces for van der Waals Heterostructures. *Nano Letters* **17**, 5222-5228 (2017).

15. J. Hone, in *Graphene 2017 Conference*. (2017).

16. C.-G. Andres *et al.*, Deterministic transfer of two-dimensional materials by all-dry viscoelastic stamping. *2D Materials* **1**, 011002 (2014).

17. L. Wang *et al.*, One-Dimensional Electrical Contact to a Two-Dimensional Material. *Science* **342**, 614-617 (2013).

18. A. V. Kretinin *et al.*, Electronic Properties of Graphene Encapsulated with Different Two-Dimensional Atomic Crystals. *Nano Letters* **14**, 3270-3276 (2014).

19. S. B. Desai *et al.*, Gold-Mediated Exfoliation of Ultralarge Optoelectronically-Perfect Monolayers. *Advanced Materials* **28**, 4053-4058 (2016).

20. R. V. Gorbachev *et al.*, Hunting for Monolayer Boron Nitride: Optical and Raman Signatures. *Small* **7**, 465-468 (2011).

21. M. M. Benameur *et al.*, Visibility of dichalcogenide nanolayers. *Nanotechnology* **22**, 125706 (2011).

22. A. Castellanos-Gomez, N. Agraït, G. Rubio-Bollinger, Optical identification of atomically thin dichalcogenide crystals. *Applied Physics Letters* **96**, 213116 (2010).

23. W. Zhao *et al.*, Lattice dynamics in mono- and few-layer sheets of WS2 and WSe2. *Nanoscale* **5**, 9677-9683 (2013).

24. C. Rice *et al.*, Raman-scattering measurements and first-principles calculations of strain-induced phonon shifts in monolayer MoS2. *Physical Review B* **87**, 081307 (2013).

25. C. Fabian *et al.*, Ultra-low power threshold for laser induced changes in optical properties of 2D molybdenum dichalcogenides. *2D Materials* **3**, 045008 (2016).

26. J. S. Cameron, D. S. Ashley, J. S. Andrew, G. S. Joseph, T. G. Christopher, Accurate thickness measurement of graphene. *Nanotechnology* **27**, 125704 (2016).

27. P. Nemes-Incze, Z. Osváth, K. Kamarás, L. P. Biró, Anomalies in thickness measurements of graphene and few layer graphite crystals by tapping mode atomic force microscopy. *Carbon* **46**, 1435-1442 (2008).

28. A. Splendiani *et al.*, Emerging Photoluminescence in Monolayer MoS2. *Nano Letters* **10**, 1271-1275 (2010).

29. S. B. Desai *et al.*, Strain-Induced Indirect to Direct Bandgap Transition in Multilayer WSe2. *Nano Letters* **14**, 4592-4597 (2014).

30. U. Wurstbauer *et al.*, Imaging ellipsometry of graphene. *Applied Physics Letters* **97**, 231901 (2010).

31. M. A. Meitl *et al.*, Transfer printing by kinetic control of adhesion to an elastomeric stamp. *Nat Mater* **5**, 33-38 (2006).

32. F. Pizzocchero *et al.*, The hot pick-up technique for batch assembly of van der Waals heterostructures. **7**, 11894 (2016).

33. P. Tonndorf *et al.*, Single-photon emission from localized excitons in an atomically thin semiconductor. *Optica* **2**, 347-352 (2015).

34. S. Kumar, A. Kaczmarczyk, B. D. Gerardot, Strain-Induced Spatial and Spectral Isolation of Quantum Emitters in Mono- and Bilayer WSe2. *Nano Letters* **15**, 7567-7573 (2015).

35. A. Castellanos-Gomez *et al.*, Local Strain Engineering in Atomically Thin MoS2. *Nano Letters* **13**, 5361-5366 (2013).

36. A. Branny, S. Kumar, R. Proux, B. D. Gerardot, Deterministic strain-induced arrays of quantum emitters in a two-dimensional semiconductor. *Nature Communications* **8**, 15053 (2017).

Chapter 4 Strain-induced single quantum emitters in mono- and bi-layer WSe_2

4.1 Introduction

Strain is a powerful tool to tune the optical properties of solid-state SQEs. In the self-assembled QD platform, strain earned its status by providing a means for continuous tuning of the emission energy while reaching and maintaining zero fine-structure splitting (FSS) [*1*]. This would not be possible without the vector property of strain which was exploited by a sophisticated piezoelectric device with controllable multi-degree of freedom. The strain-driven wavelength tuning enables precise colour matching with photonic cavities and atomic resonances, while keeping the FSS close to zero which is the condition for generating pairs of entangled photons via biexciton cascade [*2, 3*].

Two-dimensional materials present an even greater prospect for strain engineering due to the direct access and their outstanding mechanical properties, which are superior to bulk III-V semiconductors, (such as high resistance to strain [*4*] with high elastic limit [*5*] and high tune-ability [*6*]). The direct access is the consequence of the unique 2D material fabrication technique which produces fully exposed monolayers and allows integration with arbitrary substrates. As a result, monolayers can be easily integrated in a number of experiments measuring their mechanical properties. To date, strain engineering involved pushing AFM tips through a monolayer suspended over a hole [*4*], bending [*7-10*] and elongating flexible substrates [*11*], thermal expansion [*12, 13*], piezoelectricity of a ceramic crystal substrate [*14*] and controlled generation of wrinkling with pre-stretched substrates [*15, 16*]. All of these techniques demonstrate a range of strains, from uniform uniaxial and biaxial to local strains. They provided coefficients of the mechanical and optical responses, presented in a recent strain review [*6*]. Interestingly, in the review, strain measurements performed at cryogenic temperatures are not mentioned [*6*]. In order to realise strain engineering for SQEs present in WSe_2, new solutions have to be compatible with cryogenic temperatures and technology. A natural choice for inducing static strain fields in 2D layers are pre-patterned or pre-stretched substrates and for in-situ strain tuning, piezoelectric crystals.

In this chapter, I will present experimental results that demonstrate the consequences of local strain gradients achieved with pre-patterned substrates. First, I will show the correlation between the localisation of SQEs in monolayer WSe_2 and localised pockets of high strain. It will be shown that the local strain can induce spatially and spectrally isolated SQEs. To understand the nature of the localization, the strain gradients will be

analysed and quantified. In the following section, the chapter will also show how the correlation can be utilised to achieve deterministic arrays of quantum emitters with nearly 100% efficiency in mono- and bilayer WSe_2.

4.2 Correlation between SQE localisation and point-like strain perturbations

4.2.1 The sample: 2D layers of WSe_2 over a hole

In this section, flakes of WSe_2 transferred onto pre-patterned substrates will be used to correlate the positioning of SQEs and point-like strain gradients. The micrograph in Figure 4.2.1a shows a sample where a monolayer of WSe_2 lightest in contrast covers a circular (4 μm diameter) hole (1 μm depth). The neighbouring bilayer part appears with the second lowest contrast. Apart from thickness, the contrast can also locate 'naturally' occurring and sometimes unintentional corrugations like wrinkles and bumps which are also present in this sample. Such topographies usually result in higher optical contrast. These features are also expected to exhibit higher amounts of local strain than the rest of the flake. Therefore, they will be the focus point of this section.

The flake was isolated from the bulk crystal, supplied from Nanoscience Instruments (product NS00182), with mechanical exfoliation and transferred using an all-dry viscoelastic stamping procedure as described in the fabrication Chapter 3, in Sections 3.2 and 3.4. This deterministic transfer allowed for aligning the flake to the features of silicon wafer with a high precision. Interestingly, the flake preferentially fractured along crystal axis forming 60° angles and equal-sided triangles resembling its intrinsic D_{3h} point group symmetry.

4.2.2 Spatial mapping of photoluminescence and the distribution of quantum emitters

The aim of this section is to correlate the local strain and the localisation of SQEs. To investigate the distribution of local stain and learn how PL emission from WSe_2 is modulated, the PL signal from entire flake was spatially mapped with a lateral steps size of 250 nm. Local information about the sample is valuable because its environment can differ locally due to a number of reasons such as strain, dielectric screening, presence of charge traps or debris on the substrate or remainders from fabrication procedure. To start, the number of layers in the sample were unambiguously confirmed by μPL measurements and spatial mapping as shown in the Figure 4.2.2b,c. Photoluminescence from the monolayer has typical features - 2D neutral exciton (2D-X0), trion (2D-XT) and a broadband emission at lower energies. In the Figure 4.2.2c, each point of the spatial map represents integrated intensity over the spectral window within 680 - 840 nm. The map exhibits one-to-one correspondence with the micrograph showing large area of uniform

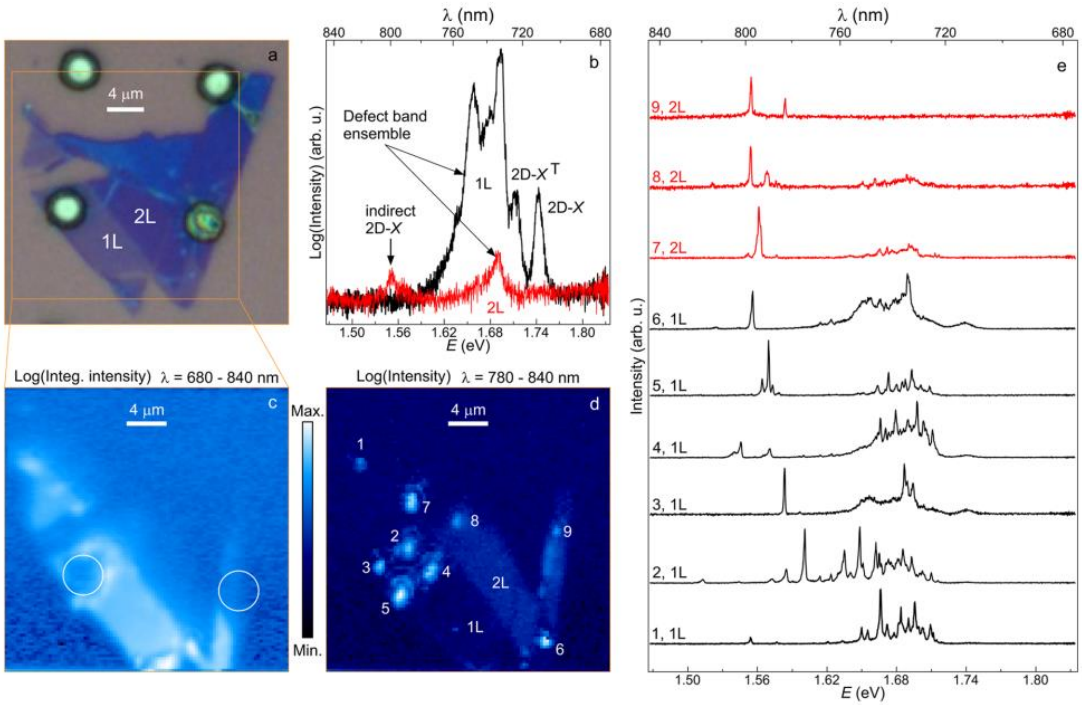

Figure 4.2.1 - **(a)** Optical micrograph of mechanically exfoliated WSe_2 flake featuring mono- and bilayer parts, transferred over an etched hole (1 μm deep, 4 μm diameter) in a Silicon substrate. The square marks the region of scanned PL. **(b)** Typical PL emission from unstrained mono- and bilayer WSe_2. Contour PL space map of **(c)** integrated intensity within 680 - 840 nm spectral window and **(d)** peak intensity within 780-840 nm. Circles mark locations of etched holes. **(e)** Spectra emitted from bright spots numbered in **d** accordingly. The excitation power was 5 μW.

intensity where the flake is fully supported as well as areas of increased intensity around the hole and decreased inside it.

Both type of intensity modulations can be associated with strain. In addition, the reduced intensity over the hole was likely caused by alteration of the focal plane due to physical buckling of the flake. This is a relevant because the spatial map was taken for fixed focal plane. On the other hand, locations where the PL has been enhanced become more evident if the same intensity map displays a narrower spectral window between 780 – 840 nm, as shown in the Figure 4.2.1d. In this instance, a much weaker indirect 2D-X emission uncovers the shape of the bilayer and a few localised bright spots become visible.

These bright spots occur in specific places - (i) on the monolayer around the edge of the hole and (ii) in both monolayer and bilayer regions of the flake. Each location is numbered and represented by the characteristic spectrum in Figure 4.2.2e. Spectra in black labelled 1-6 are from monolayer and in red 7-9 are from bilayer WSe_2. Spectra from the bright spots are strikingly different from the typical emission spectra from mono- and bilayer WSe_2 as seen in Figure 4.2.2b. They developed a comb-like emission in the region of the defect-band and very sharp emission lines at much lower energies. It has been shown that

each line constitutes a single photon emitter [*17-20*]. However, the observation of peaks in bilayer and such isolated, highly detuned peaks in monolayer is unique. In the next section, it will be demonstrated that locations at which the spectrum develops the comb-like emission are caused by pockets of local strain.

The micrograph provides the quickest and the easiest to recognise the local strain. As mentioned in Section 4.2, the parts of the flake with a higher contrast than the rest indicate changes in the topography such as point-like corrugations and wrinkles. For example, the bright spots with 1 and 6 clearly originate from the bumps on the monolayer. Moreover, the emitters 7 and 8 can be correlated with wrinkles in the bilayer part. However, the quantum emitters in the PL map appear in more places than the micrograph is able to disclose. For example, emitters 2-5 seems to lay around the edge of the hole without any indication from the optical image. In order to explain the origin of this appearance, a thorough approach of measuring the local strain in the sample is essential. Here the local strain is experimentally estimated by exploiting the relationship that strain has with the energy of 2D-X0 emission. The estimate is based on the relationship calculated from first principles and is given to be −55 meV shift per percent of uniaxial tensile strain (see Figure S5(b) of ref [*7*]). This can be used to directly convert a map of the 2D-X0 energy determined by PL into a strain map. Figure 4.2.2a demonstrates the outcome of this conversion.

The map in Figure 4.2.2a displays the energy of 2D-X0 peak converted into strain. The strain map does not display the absolute value of strain but rather the relative difference from the reference point R, which belongs to the flat, unstrained region. For the region near R, the strain variation is less than 0.05%. This uniform and unstrained area coincides with the area of constant integrated intensity of PL.

Apart from unstrained areas, there are distinct pockets of steep and localized strain gradients which occur around the edge of the hole and at all locations mentioned previously. The strain pockets are labelled P1 to P6 and the spectra associated with each pocket are shown by Figure 4.2.2b. The PL signal from the reference point R is also included for comparison. This comparison endorses the same striking difference observed in the Figure 4.2.1. Each spectrum from inside the strain pocket exhibits almost vanishing, red-shifted 2D-X0 peak and a dispersed forest of sharp lines with occasional highly isolated peaks at lower energies.

Some of the pockets can be immediately correlated to the change in contrast in the optical image. For example, pocket P1, showing a nominally identical spectrum to spectrum 6 in Figure 4.2.2, originates from a physical bump in the bottom right. Other pockets P2-P4 are caused by bending of the flake around the edge of the etched hole. Pocket P5 experiences the largest red-shift of 2D-X0 and is caused by a wrinkle propagating from the 2L region, as seen in the optical micrograph Figure 4.2.2a. Further, strain-gradient correlations are found for all emitters in Figure 4.2.2d-e: four localised at the edges of the patterned hole, the remaining at locations of unintentional strain. This direct correlation of localised strains and occurrence of spectrally and spatially isolated quantum emitters leads to a robust conclusion that the local strain variations are responsible for inducing quantum emitters in a 2D semiconductor.

4.2.3 In depth characterisation of local strain gradients

To characterize the strain pockets (their widths and depths). Figure 4.2.2c displays the change in 2D-X0 peak energy (ΔE^{2D-X0}) for horizontal line-cuts in the strain map, at the centre of the five highly strained regions and the reference point R. Notably, the strain modulation across the flat region is smooth while pockets P1−P3 show linewidths (FWHM) approaching the diffraction limit of the confocal microscope resolution (~500 nm). This suggests that actual strain variations are even more localised and deeper than measured. This is simply due to the averaging over the microscope resolution. Nevertheless, ΔE^{2D-X0} as large as −10 meV are observed in the localized pockets which translates to estimated relative strain change of around 0.2%. This analysis sets a guideline for strain gradients which are sufficient to cause the localisation of single quantum emitters in a 2D semiconductor.

To decisively eliminate local contamination and chemical doping as an alternative explanation for the spectrally and spatially isolated emitters, Figure 4.2.2d plots three spectra. These PL spectra were taken from locations R, P3 and P6 shown in Figure 4.2.2a. We can observe that: (i) the ratio of 2D-X0 to 2D-XT intensities is maintained at positions R and P3; (ii) the center of the broad defect ensemble moves linearly and at the same rate as the 2D-X0 and 2D-XT; and (iii) the linewidth of the broad defect ensemble increases with increasing strain. Note that the measurement of strain at location P6 was not possible because the 2D-X0 signal was too weak. Instead, a clear widening of the defect ensemble band can be seen. These three observations strongly support the correlation of strain and emitter tuning rather than local substrate contamination or chemical doping.

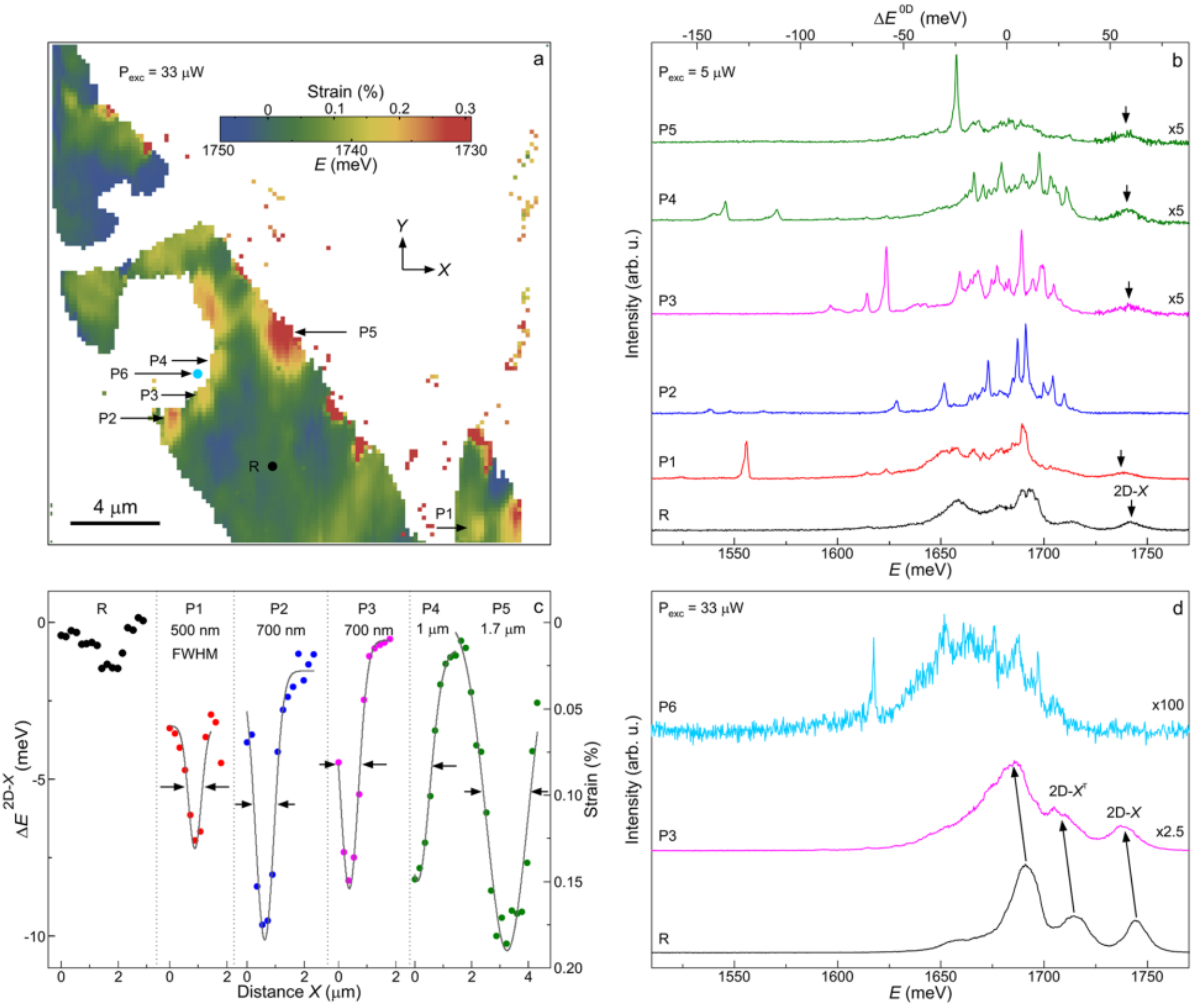

Figure 4.2.2 – **(a)** Contour space map of the 2D-X0 energy of the monolayer from Figure 4.2.1a showing a several local energy minima, labelled as pockets P1-P5. To estimate strain, the map also displays the energetic difference, $\Delta E^{2D\text{-}X0}$ relative to the reference point R. **(b)** PL spectra from the pockets P1-P5 and reference R and **(c)** horizontal cross-sections through the same points. **(d)** Set of PL spectra from R, P3 and P6 taken with high excitation power to demonstrate linear homogenous spectral shift, dispersion of defect band and vanishing 2D-X0 with increasing strain.

To summarise the section, it has been demonstrated that local strain gradients offer the capability to engineer the spatial and spectral properties of SQEs. It red-shifts all peaks in the spectrum, weakens neutral exciton emission intensity, disperses the defect assemble emission and creates few noticeable emitters which become favourable to emit. These results raise the prospect of deterministically creating a lattice of strained quantum emitters in 2D semiconductors by placing the flake over a nanostructured surface such as periodic array of pillars or holes. This will be the focus of the following section.

4.3 Deterministic array of strained single quantum emitters

Deterministic positioning of SQEs is a necessary prerequisite of scalability in quantum photonic platforms. Site control has been achieved with defects in diamonds [*21*] and

self-assembled quantum [*22*] dots but it often meant deterioration of coherence and optical quality. In light of the results in the previous section, localised strain offers the opportunity to build a scalable quantum architecture with two-dimensional semiconductors.

4.3.1 Sample fabrication

To achieve point-like strain perturbations in WSe_2, all flakes presented in the section were transferred with viscoelastic, all-dry technique onto pre-patterned nanopillar square lattice with 4 μm spacing. The viscoelastic transfer relies on van der Walls adhesion and produces enough pressure which forces the flake to closely adhere to the topography of the nanostructured surface inducing significant amount of elastic strain at the nanopillar locations. The nanopillars made of a dielectric negative resist were fabricated by electron beam lithography which involved spin coating the resist (AZ 2070 from MicroChemicals), exposure to electrons (Raith Pioneer) and development by immersion in the solvent (AZ 726 MIF Developer from Electric Materials).

With this method, 3 samples were fabricated. To demonstrate the proof of the concept, first two samples, a monolayer and a bilayer WSe_2 were placed on identical nanopillar with aspect ratio of height to width (h:w) of ~0.3. To optimise the technique and to seek the best position accuracy, the third sample is a large monolayer placed on the strain lattice with varying nanopillar dimensions. After the transfer, locations of nanopillars in each sample are identified by regions with increased contrast in the optical micrograph and their effect is analysed with PL confocal mapping and hyperspectral analysis.

4.3.2 A monolayer WSe_2 quantum emitter array

To examine how well the flake conforms to the contours of the nanopillar, the topography of monolayer WSe_2 was characterised by atomic force microscopy (AFM) and scanning electron microscopy (SEM) as shown in Figure 4.3.1-2. Figure 4.3.1a,b displays optical images of the sample before and after the transfer where monolayer and bilayer parts were identified by their contrast and then confirmed by the PL emission. The Figure 4.3.1c,d shows the results of AFM and SEM imaging which confirms the same physical features of the region marked by the black frame in Figure 4.3.1b. Both images demonstrate that flake can adhere to a nanopillar very tightly like in #2, 3, 7 or stretch over a bigger area analogously to a canvas over a tent-pole as for #5, 6, 8, 9.

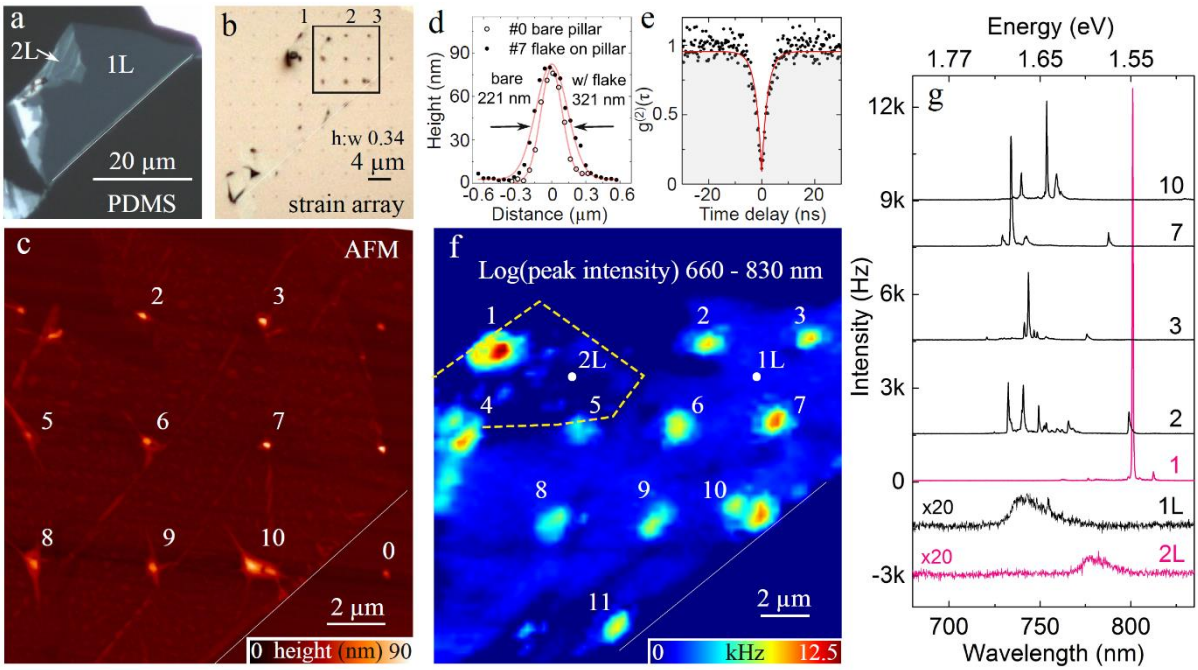

Figure 4.3.1 – Optical micrograph of an exfoliated WSe_2 monolayer **(a)** before and **(b)** after transfer onto a strain array with dielectric nanopillars seen as black points. The black square in **b** indicates the characterised region in **c** and **f**. **(c)** AFM scan displaying the topography of the flake on top of the square lattice of nanopillars. **(d)** AFM cross-sections comparing bare nanopillar #0 with covered with monolayer nanopillar #7. **(e)** Results of second-order photon correlation measurement produced by a typical quantum emitter hosted by monolayer exhibiting clear single-photon statistics [$g(2)(0) = 0.07 \pm 0.04$ and $\tau = 2.8 \pm 0.4$ ns]. **(f)** Contour PL space map of peak intensity within 660-830 nm spectral range. **(g)** PL spectra of induced quantum emitters at corresponding and labelled nanopillar sites. Weak signal from unstrained 1L and 2L WSe_2, in between nanopillars is also shown.

Despite these differences, the PL mapping in the Figure 4.3.1f shows that each nanopillar induces increased PL peak and integrated intensity by a factor 50 and 2, respectively (relative to the unstrained regions in between nanopillars). In between pillars, the flake emits a weak broad defect band emission. This is in striking contrast to the emission from nanopillar locations where a spectrum with discrete lines of high intensity and narrow linewidths are typically observed including very bright and clean emission from the small bilayer region as shown in Figure 4.3.1g. Both observations, the enhancement of PL intensity and the appearance of sharp peaks, are common for all samples placed on a strain lattice. Each of these peaks signify emission from single photon emitters. To verify the quantum nature of induced emitters at the strain sites, a second-order correlation measurement was performed. Its results, presented in Figure 4.3.1e, exhibits antibunching with fitted values for $g^{(2)}(0) = 0.07 \pm 0.04$ and decay time of $\tau = 2.8 \pm 0.4$ ns, validate single photon emission.

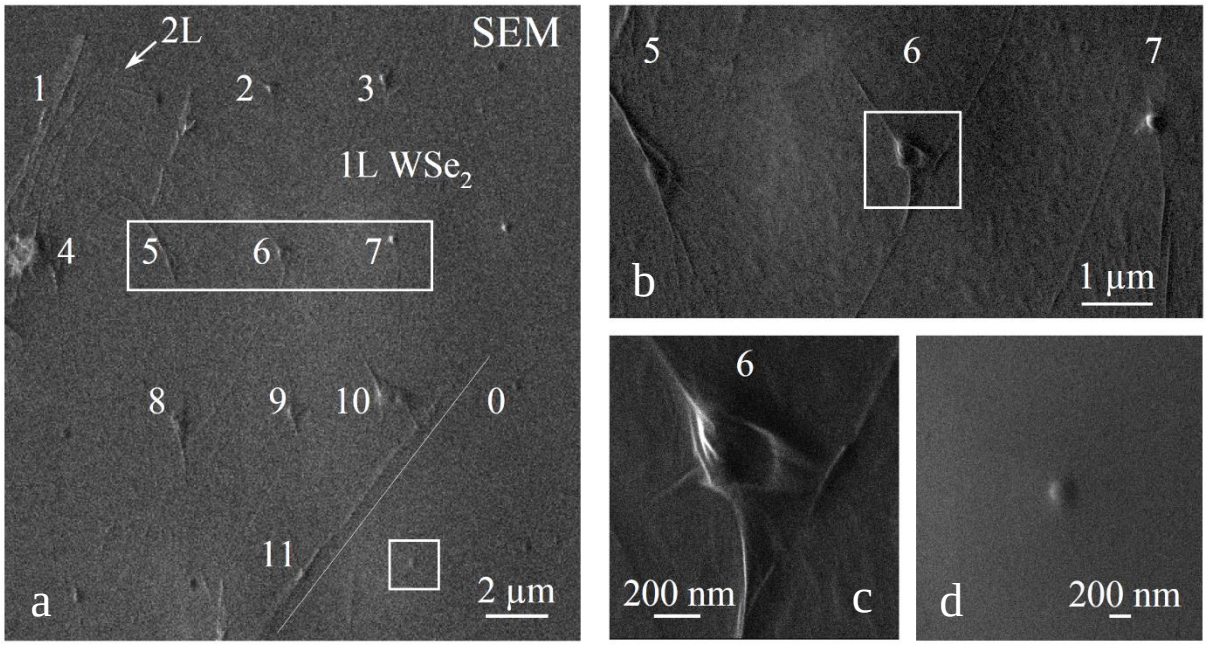

Figure 4.3.2 – Scanning electron microscope (SEM) images of WSe_2 monolayer on nanopillars from Figure 4.3.1. **(a)** Zoomed out view of the entire sample showing one-to-one comparison with Figure 4.3.1 and same labelling. **(b)** Magnification of nanopillars 5, 6 and 7. **(c)** Magnification of nanopillar 6. The wrinkling of the monolayer at the nanopillar agrees with AFM profiles. **(d)** A bare nanopillar marked by a white square at the bottom right in **a**.

4.3.3 Impact of topography on photoluminescence emission.

While making a closer comparison between the AFM, SEM and PL of sample no. 1, one can observe that creases and wrinkles emerge from the nanopillars and sometimes propagate to the neighbours, which have no noticeable effect on the PL emission. These corrugations were expected from suspended flake over the periodic array of nanopillars and can be further engineered [*23, 24*]. Nevertheless, this indicates that the 4 µm spacing in the array is sufficiently large to prevent the creation of wrinkles which would mask the point-like strain perturbations created by the nanopillars. From AFM and SEM one can also learn that there are differences in the precise dimensions of the final monolayer topography induced by each nanopillar which in fact, have direct impact on the PL emission as shown in Figure 4.3.3, where pink numbers correspond to the strain sites as numbered in Figure 4.3.1-2. Therefore, one can expect higher integrated intensity and brighter quantum emitters as the deformation gets narrower and taller. Further, the FWHM of the induced deformation directly correlates with the FWHM of the PL intensity enhancement. Figure 4.3.3 presents a trend between topography and PL emission where a distinct, high-performance group can be identified of closely conforming WSe_2 at nanopillars #2, 3 and 7 which generate brighter PL signal than the rest. This suggests that the dimensions of nanopillars play a crucial role in further engineering and improving

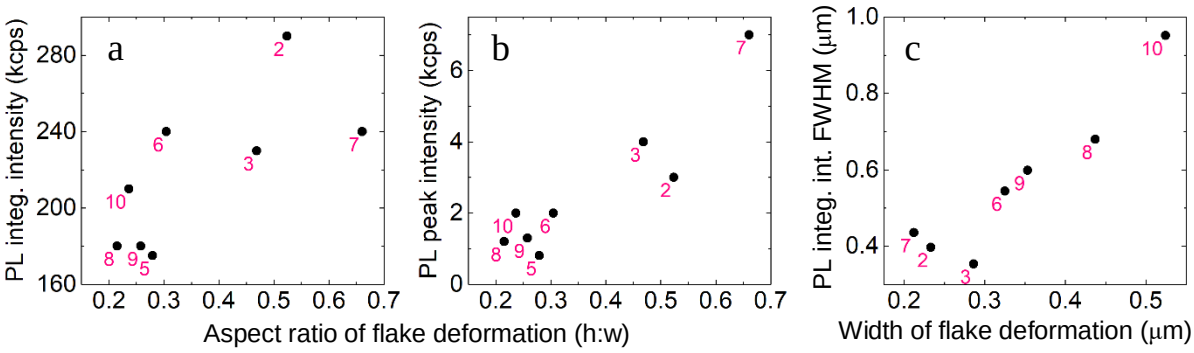

Figure 4.3.3 – **(a)** Integrated and **(b)** maximum peak intensity of PL emission from strain sites, as labelled in Figure 4.3.1f, plotted as a function of height to width aspect ratio of created deformation in WSe_2 monolayer given by AFM. (c) The width of strain-induced enhancement of PL emission as a function of the width of flake deformation. All graphs show correlations between topography and PL emission.

emitters brightness, localisation accuracy and the quality of spectral and spatial isolation. This will be pursued in the following section 4.3.5.

4.3.4 A bilayer WSe_2 quantum emitter array.

Intriguingly, when a bilayer WSe_2 is subjected to point-like strain perturbation, similar results to those of monolayer are obtained. Figure 4.3.4a,b show optical micrographs before and after the transfer, where black points are caused by nanopillars in the strain array. As the PL map discloses in Figure 4.3.4c, once again, a significant, periodic and localised enhancement of the emission intensity at each nanopillar site was observed which was as high as 150 times in peak and 3 times in integrated intensity. This strain-driven intensity modulation can be associated with the funnelling effect as well as with transition to a direct bandgap. The PL maps also covers the regions of the flake with monolayer and trilayer parts. While the monolayer exhibits similar behaviour to the previously studied sample, the trilayer is not influenced by the strain and remains dark in PL. Crucially, spectra from nanopillar sites contain bright narrow linewidth peaks as shown in Figure 4.3.4d. Figure 4.3.4e superimposes their locations on a high-resolution spatial map. Individual emitters hosted by the bilayer also exhibit pure single photon, as emission confirmed by second-order correlation measurement (Figure 4.3.4f) where the fitting provided $g^{(2)}(0) = 0.03 \pm 0.02$ and a decay time of $\tau = 4.8 \pm 0.1$ ns. Interestingly, these quantum emitters appear at shorter wavelengths than the weak broad defect band emission. This is opposite to the quantum emitters hosted by monolayers which appear at longer wavelengths. This is consistent with the bandgap response to strain. For small amounts of strain, the bandgap modulation in monolayer and bilayer acts in the opposite directions. Notably, several bilayer quantum emitters share very similar wavelengths. These results introduce bilayer WSe_2 as a new member of 2D quantum photonic platform

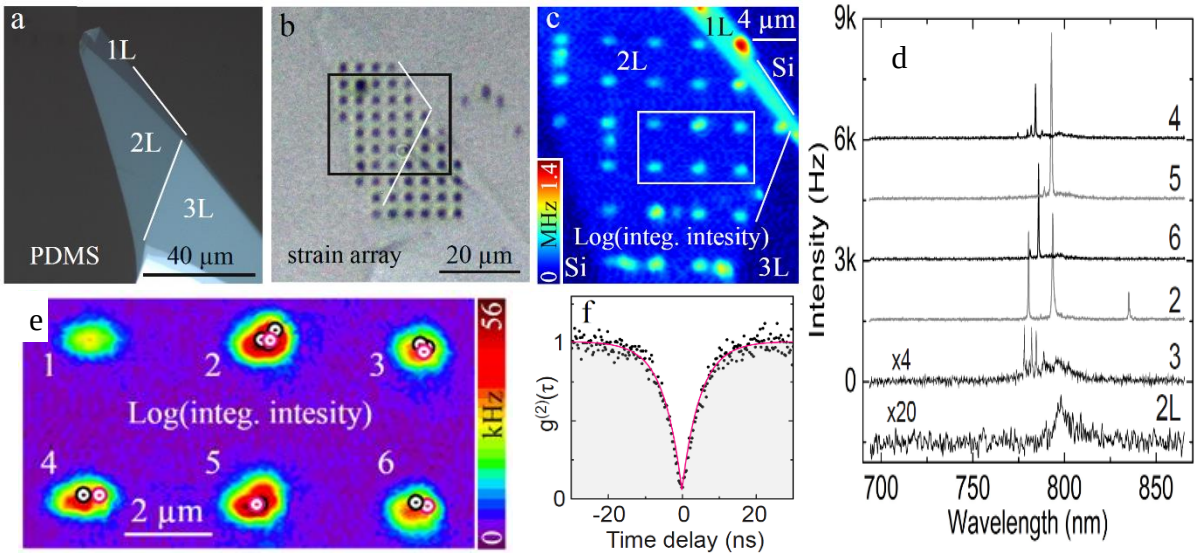

Figure 4.3.4 – Optical micrograph of an exfoliated WSe_2 bilayer **(a)** before and **(b)** after transfer onto a strain array with dielectric nanopillars seen as black points. The black frame in **b** indicates the characterised region for PL in **c**. **(c)** Contour PL space map of peak intensity within 700-860 nm spectral range. **(d)** PL spectra of induced quantum emitters at five nanopillars indicated in **c**, as labelled in **e** with red circles. **(e)** A high resolution color-coded PL map of integrated intensity of six pillars marked in **c** with superimposed positions of individual emitters of which a few are shown in **d**. **(f)** Results of a second-order photon correlation measurement produced by a typical quantum emitter hosted by a WSe_2 bilayer exhibiting single-photon statistics [$g(2)(0) = 0.03 \pm 0.02$ and $\tau = 4.8 \pm 0.1$ ns, emitter at nanopillar #1 in Figure 4.3.1f,g].

and demonstrate wider applicability of nanoscale local strain engineering in inducing SQEs. In its own rights, bilayer WSe_2 is an intriguing host, exhibiting distinct features from the monolayer which make this material unique, for instance for investigating the relation between layer-dependent pseudo-spins and SQEs [*25*].

4.3.5 Optimisation of strain-induced arrays of quantum emitters.

To employ the observation presented in the section 4.3.3 and explore optimised nanopillar dimensions, another strain array was lithographically defined to create a set of local strain perturbations. The new strain array consists of five rows of nanopillars varying in the aspect ratio, with height to width ratios from 0.15 to 0.59 as shown by SEM in Figure 4.3.5a. AFM was used to inspect the exact nanopillar dimensions and confirmed uniformity within each row yielding the cross sections displayed in Figure 4.3.5c. Here, instead of needle-like, nanopillars with high w:h ratio has flat tops which one could expect to create ring-shaped strain perturbations. In Figure 4.3.5b, the optical image shows a large, 100×25 µm WSe_2 monolayer which covered 101 nanopillars and all 5 rows in the strain array. The change in the contrast uncovers the locations of each nanopillar. Most pillars appear as bright points but some from the tallest (row 4 and 5) display bright circles

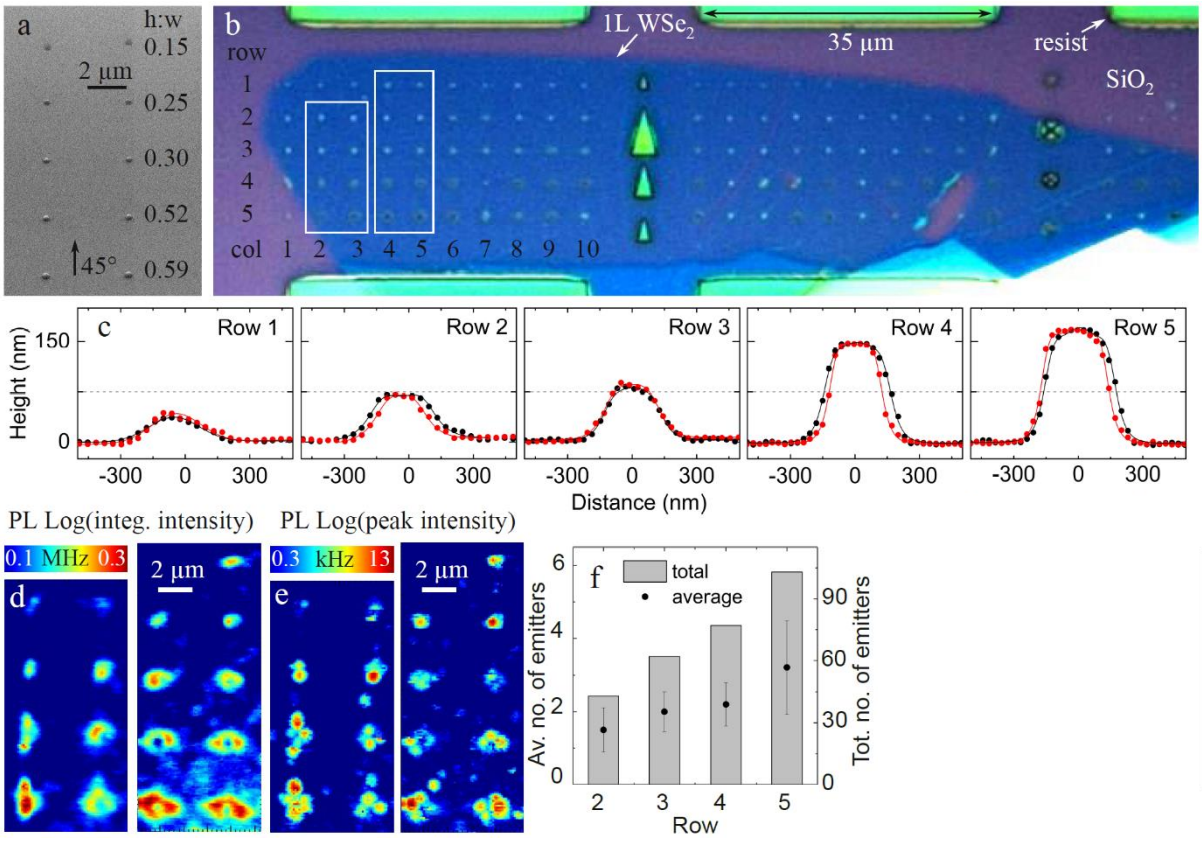

Figure 4.3.5 – **(a)** A 45° SEM image of SiO_2 substrate with a nanopillar array of varying aspect ratio, as labelled. **(b)** Optical micrograph of a large (100×25 µm) WSe_2 monolayer which covers 101 nanopillars seen as bright and dark points with labelled columns and rows. When dark in colour, this might suggest the flake being pierced by the nanopillar or closely conforming to its topography including the flat top. **(c)** Vertical and horizontal AFM cross-sections of bare nanopillars from five rows with varying aspect ratio. **(d)** A high resolution contour PL space map of integrated intensity within 690-850 nm for columns 2-5 marked in **b**. As nanopillar aspect ratio increases the bright ring increases its diameter. **(e)** The set of maps as d but displaying peak intensity instead where individual quantum emitters are resolved. **(f)** Cumulative and average emitter statistics per pillar for each row. Error bar corresponds to a single standard deviation.

with a dark centre. This feature is not seen in other fabricated samples. Yet, in Figure 4.3.5d the PL map of integrated intensity once again reveals periodic locations at which nanopillars significantly increased the intensity due to exciton funnelling. Noticeably, for the nanopillar row with highest aspect ratio, the intensity enhancement takes the shape of a ring. This could be caused by the punctured flake which happened during the transfer process as terminations of the flake tend to also induce bright quantum emitters. Equally, the flake could simply conform very closely to the flat-topped and bend over the circular edges to produce a ring-shaped strain profile. Nevertheless, the total intensity shows a clear increasing trend with increasing aspect ratio of the pillars and the sizes of the bright rings reflect the dimensions of the nanopillar. On the other hand, thanks to mapping of the peak intensity, 285 intense narrow linewidth peaks were identified in the entire sample. It safe to assume that each signifies a single quantum emitter. Every

peak in the spectrum narrower than 1 nm was included in the statistics assuming each emerged from a single emitter without taking into account multiple-peak emissions. Figure 4.3.5f counts them all and displays them as a function of row number. From these statistics, a single conclusion can be made: the higher the aspect ratio the larger number of emitters. However, with the flat-topped pillars, the message might not be accurate and instead it should read: the larger the ring of strain perturbation the larger number of emitters. A parallel work of Palacios-Berraquero *et. al.* also shows that for needle-topped nanopillars one could expect the number of emitters converge towards one with increasing aspect ratio [*26*]. Nevertheless, although it observed that tall pillars induce more emitters, thanks to larger and sharper strain modulation their spectra tend to be cleaner and with fewer lines than those from shorter pillars. It is also clear that the success of inducing emitters with nanopillars is as high as 96% for row 3 and 4 (45 out of 47 yield at least 1 quantum emitter), and 85% for row 2 (17 out of 20 show a single emitter). However, nanopillars from row 1 did not induce bright enough emitters to be easily distinguished from the broad background, therefore they are not displayed. These results demonstrate that dielectric nanopillars arranged in an array provide a reliable way of creating a large number of quantum emitters thanks to nanoscale local strain. Next, I will investigate how accurately the nanopillars define the locations of the emitters.

4.3.6 Positioning accuracy.

In this section, positioning accuracy of the strain-induced quantum emitters will be determined. To obtain emitter locations relative to the centre of the nanopillar, PL maps of high spatial resolution were used. While precise locations of individual emitters can be distilled from the spatial distribution of the peak intensity, the exact position of the nanopillars is not known *a priori*. Therefore, nanopillar locations are extracted from a weighted average wavelength (WA_λ). The spectral weighted average gauges the global shift in the PL spectrum due to the presence of nanopillar. Therefore, apart from localising the centre of the nanopillar, the WA_λ can be also utilised to estimate strain. Figure 4.3.6a compares two spectra, one from the centre of nanopillar and another from unstrained region, where the spectral shift is evident. A spatial map of the global shift is computed by converting the spectrum at each location into a single number with the following formula: $WA_\lambda = (\Sigma_\lambda \lambda \cdot I) / (\Sigma_\lambda I)$. This numerical approach was chosen to track the shift instead of fitting because the spectrum does not resemble standard peak functions, including Gaussian. Furthermore, the strain is so large that it is impossible to map the energy of 2D-X0 as its intensity vanishes completely.

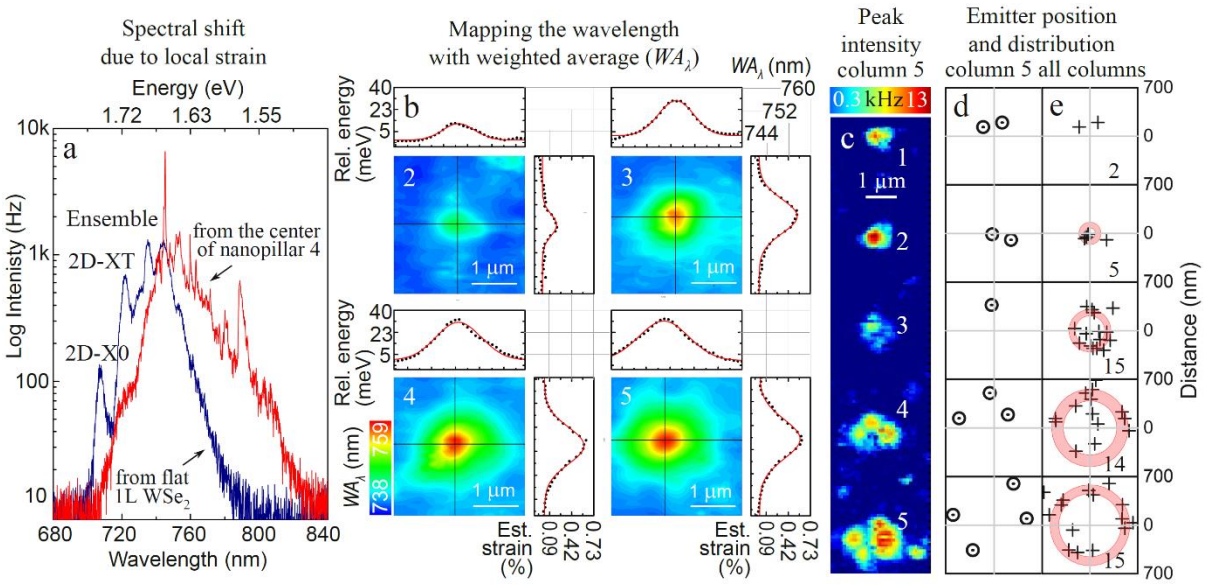

Figure 4.3.6 – **(a)** Typical PL spectra from unstrained and biaxially strained WSe_2 monolayer at the centre of nanopillar #4 in column 5. 2D-X0 and 2D-XT refers to the non-localised neutral and charged exciton emissions respectively. **(b)** Contour space map of weighted average wavelength (WA_λ) for nanopillars 2-5 from **c**. Cross-sections of WA_λ are fitted with Gaussian peaks which provide precise position of the nanopillar centre. The absolute spectral shift is converted into relative energy shift and estimated strain with the respect to unstrained regions. **(c)** A high-resolution contour PL map of peak intensity from column 5. The single emitters are resolved, their locations extracted from fitted Gaussian peaks and to be compared against the WA_λ mapping. **(d)** Locations of individual emitters (black circles) relative to the nanopillar centres (grey crosses) for each row in column 5. **(e)** Distribution of emitters (black crosses) from columns 2-5. The red rings and their thickness corresponds to average emitter displacement and its single standard deviation. The number of emitters contributing to the distribution is listed in the botton right corner of each map.

The result of the conversion leads to a smooth profile map with well-defined peaks of elevated WA_λ as shown Figure 4.3.6b for nanopillars from Column 5 and Rows 2-5. The cross-sections of the profiles can be fitted with Gaussian peaks providing high accuracy positioning for the nanopillar centres. This localization approach relies on the assumptions: (i) that the strain is the largest at top of each nanopillar and (ii) the strain can be estimated by the global spectral shift yielding to the nanopillar location. For instance, for nanopillar #4, a rough estimate of strain gives 0.60% after conversion from the relative spectral shift of WA_λ = 30.8 meV (13.3nm) [*7*]. Finally, Figure 4.3.6d shows nanopillars in Column 5 as grey crosses with superimposed displacements of individual emitters marked as black circles. To evaluate the overall position accuracy, the relative placement of emitters from Columns 2-5 were combined to arrive at the distribution shown in the Figure 4.3.6e. The red rings and their thicknesses illustrate the mean displacement with a single standard deviation. While Row 1 did not produce enough emitters for useful statistics, the distribution of other rows exhibits a progression from

highly confined displacement σ = 120 ± 32 nm in Row 2 to a wide ring with radius equal to σ = 521±32 nm in Row 5, where σ is the average emitter displacement from the nanopillar centre. Average displacements for other Rows 3 and 4 are σ = 262 ± 46 nm and σ = 476 ± 85 nm. These numbers indicate that the flat-topped nanopillars induce emitters at the circumference, hence they are not a desirable geometry. On the other hand, for nanopillars which created a point-like strain perturbation (like Row 2), quantum emitters are found in their centre. In the best case, for Column 5 and Row 2, the displacement is only 30 nm.

4.3.7 On practicalities and limitations of acquiring the local strain with 2D neutral exciton and spectral weighted average.

This section discusses and compares the two approaches for estimating strain using the neutral exciton emission energy and spectral weighted average. In the case of 2D-X0, the first aspect to mention is that all spectra were fitted with 3 to 5 Gaussian peaks and the PL map was taken at elevated power (33 μW) to ensure a sufficient signal to background ratio (SBR). Although potentially harmful to the flake, the high power is essential due to the decline of the neutral exciton emission intensity caused by the strain and the exciton funnelling effect. Even at that power, there are still places on the sample, i.e. in the proximity of the hole edges, at which the 2D-X0 peak vanishes due to high strain, setting a limit on the maximum measurable strain at around 0.2%. At these locations the fitting becomes unreliable. Therefore, values > 0.2% are not included in the strain map.

Another point worth-noting is that the conversion used for 2D-X0 and WA_λ assumes uniaxial tensile strain, while the strain in the sample is likely to be biaxial due to the geometry of unintentional bumps and deterministic nanopillars. Despite this, the approach still describes quantitatively the relative shifts of 2D-X0 energy and entire spectrum with WA_λ which was obtained by direct measurement. Another source of limitation which is relevant for both strain indicators, arises from the optical set up. The optical resolution limits the smallest spatial variation that can be detected originating from the diffraction-limited laser spot size with FWHM of approximately 500 nm. Therefore, any variation smaller than the laser spot size will be averaged over the entire area, leading again to reduced values of measured strain. This limitation especially affects the strain estimation for strain array where the nanopillars were 500 nm in diameter wide. Perhaps this is why the flat-topped pillars generate single peaks in the WA_λ profile while rings were anticipated.

Finally, the weighted average relies on the assumption that the entire spectrum shifts with strain at the same rate as the 2D-X0 does, which might not be accurate as these two quantities have not been calibrated. However, WA_λ provides an easy and universal way of estimating strain in 2D semiconductors as it involves minimal amount of post-processing and does not require specific peaks to be present.

4.4 Summary

Semiconducting 2D TMDs, such as mono- and bilayer WSe_2, represent a novel solid-state platform for quantum optics with great potential as outlined in the introduction Chapter 1, in Section 1.4. This chapter, brought to light a particularly powerful feature: local strain engineering and its influence on SQEs.

The focus of this chapter was the photoluminescence of monolayer and bilayer WSe_2 samples subjected to local strain engineering. The strain engineering was achieved by transfer-induced and naturally occurring corrugations like wrinkles as well as by the nanostructured substrates with arrays of nanopillars. Both approaches created large local strain gradients.

With the aid of scanning confocal microscopy, PL signals acquired at each point on the sample produced a spatial map of single emitter distributions. Similarly, spatial information about the strain landscape was obtained from the 2D-X0 emission to observe numerous strain pockets. After comparing both spatial maps, the influence of local strain pockets became apparent. Strain pockets induced, redshifted and localised single quantum emitters. Further, in-depth characterisation showed that strain gradients as deep as 10 meV (0.2%) and as narrow as diffraction-limit (500 nm) are sufficient to localise emitters in WSe_2. Moreover, with the analysis of the relative intensities and the shift of neutral exciton and trion, local contamination and chemical doping were excluded as a contributor to the emitter localisation. These results demonstrated that strain engineering is a viable approach to obtain spatially and spectrally isolated quantum emitters in 2D semiconductors.

These results opened the opportunity to construct deterministic array of quantum emitters via nanoscale local strain engineering utilised. Strain arrays were nanofabricated on 3 samples. It was observed that the strain devices locally modified the electronic and optical properties of mono- and bilayer WSe_2 to reliably induce highly pure single quantum emitters with highly deterministic positioning. The optimisation of nanopillar dimensions led to results with near unity yield in generating an emitter at each nanopillar

site and a mean localisation accuracy of 120 nm, achieved by nanopillars with 0.3 aspect ratio. Further, spectra generated by appropriately shaped nanopillars exhibit clean single emissions with a single dominant peak and negligible background. Interestingly, bilayer WSe_2 joins the 2D quantum photonics platform.

This approach with a straightforward fabrication procedure is fully scalable and can be applied to other 2D semiconductors. Local strain engineering opens prospects of embedding emitters deterministically in charge devices and coupling them to cavities and waveguide modes for cavity quantum electrodynamics and integrated photonics applications [*27, 28*].

Notably, there is significantly more potential for strain engineering of 0D-X states than presented in this chapter. First, there are a number of already available approaches for static and dynamic, uniaxial and biaxial strain engineering [*6, 29*] which could generate the extraordinary amounts of strain 2D materials can withstand [*4*]. It is widely appreciated that the impact of strain extends to other electronic and optical properties of 0D-X states beyond the emission energy. For instance, in-situ strain tuning can enable engineering of the carrier confinement potential [*30*], the permanent dipole moment, the fine-structure splitting [*31*], and the spin properties [*32*] of localized exciton states. Notably, such quantum emitters could underpin a hybrid semiconductor-atomic interface [*33*].

4.5 References

1. R. Trotta *et al.*, Wavelength-tunable sources of entangled photons interfaced with atomic vapours. *Nature Communications* **7**, 10375 (2016).

2. O. Benson, C. Santori, M. Pelton, Y. Yamamoto, Regulated and Entangled Photons from a Single Quantum Dot. *Physical Review Letters* **84**, 2513-2516 (2000).

3. N. Akopian *et al.*, Entangled Photon Pairs from Semiconductor Quantum Dots. *Physical Review Letters* **96**, 130501 (2006).

4. A. Castellanos-Gomez *et al.*, Elastic Properties of Freely Suspended MoS2 Nanosheets. *Advanced Materials* **24**, 772-775 (2012).

5. S. Bertolazzi, J. Brivio, A. Kis, Stretching and Breaking of Ultrathin MoS2. *ACS Nano* **5**, 9703-9709 (2011).

6. R. C.-G. Roldán, André;, Cappelluti, Emmanuele; Guinea, Francisco, Strain engineering in semiconducting two-dimensional crystals. *Journal of Physics: Condensed Matter* **27**, 313201 (2015).

7. S. B. Desai *et al.*, Strain-Induced Indirect to Direct Bandgap Transition in Multilayer WSe2. *Nano Letters* **14**, 4592-4597 (2014).

8. C. R. Zhu *et al.*, Strain tuning of optical emission energy and polarization in monolayer and bilayer MoS${}_{2}$. *Physical Review B* **88**, 121301 (2013).

9. K. He, C. Poole, K. F. Mak, J. Shan, Experimental Demonstration of Continuous Electronic Structure Tuning via Strain in Atomically Thin MoS2. *Nano Letters* **13**, 2931-2936 (2013).

10. H. J. Conley *et al.*, Bandgap Engineering of Strained Monolayer and Bilayer MoS2. *Nano Letters* **13**, 3626-3630 (2013).

11. Y. Wang *et al.*, Strain-induced direct–indirect bandgap transition and phonon modulation in monolayer WS2. *Nano Research* **8**, 2562-2572 (2015).

12. R. Frisenda *et al.*, Biaxial strain tuning of the optical properties of single-layer transition metal dichalcogenides. *npj 2D Materials and Applications* **1**, 10 (2017).

13. P. Gerd *et al.*, Control of biaxial strain in single-layer molybdenite using local thermal expansion of the substrate. *2D Materials* **2**, 015006 (2015).

14. Y. Y. Hui *et al.*, Exceptional Tunability of Band Energy in a Compressively Strained Trilayer MoS2 Sheet. *ACS Nano* **7**, 7126-7131 (2013).

15. A. Castellanos-Gomez *et al.*, Local Strain Engineering in Atomically Thin MoS2. *Nano Letters* **13**, 5361-5366 (2013).

16. S. Yang *et al.*, Tuning the Optical, Magnetic, and Electrical Properties of ReSe2 by Nanoscale Strain Engineering. *Nano Letters* **15**, 1660-1666 (2015).

17. C. Chakraborty, L. Kinnischtzke, K. M. Goodfellow, R. Beams, A. N. Vamivakas, Voltage-controlled quantum light from an atomically thin semiconductor. *Nat Nano* **10**, 507-511 (2015).

18. Y.-M. He *et al.*, Single quantum emitters in monolayer semiconductors. *Nat Nano* **10**, 497-502 (2015).

19. KoperskiM *et al.*, Single photon emitters in exfoliated WSe2 structures. *Nat Nano* **10**, 503-506 (2015).

20. A. Srivastava *et al.*, Optically active quantum dots in monolayer WSe2. *Nat Nano* **10**, 491-496 (2015).

21. T. Schröder *et al.*, Scalable focused ion beam creation of nearly lifetime-limited single quantum emitters in diamond nanostructures. *Nature Communications* **8**, 15376 (2017).

22. M. H. Baier *et al.*, Single photon emission from site-controlled pyramidal quantum dots. *Applied Physics Letters* **84**, 648-650 (2004).

23. A. Reserbat-Plantey *et al.*, Strain Superlattices and Macroscale Suspension of Graphene Induced by Corrugated Substrates. *Nano Letters* **14**, 5044-5051 (2014).

24. H. Li *et al.*, Optoelectronic crystal of artificial atoms in strain-textured molybdenum disulphide. **6**, 7381 (2015).

25. A. M. Jones *et al.*, Spin–layer locking effects in optical orientation of exciton spin in bilayer WSe2. **10**, 130 (2014).

26. C. Palacios-Berraquero *et al.*, Large-scale quantum-emitter arrays in atomically thin semiconductors. **8**, 15093 (2017).

27. K. J. Vahala, Optical microcavities. *Nature* **424**, 839-846 (2003).

28. P. Lodahl, S. Mahmoodian, S. Stobbe, Interfacing single photons and single quantum dots with photonic nanostructures. *Reviews of Modern Physics* **87**, 347-400 (2015).

29. C. W. Hicks *et al.*, Strong Increase of T_c of Sr₂RuO₄ Under Both Tensile and Compressive Strain. *Science* **344**, 283-285 (2014).

30. C. E. Kuklewicz, R. N. E. Malein, P. M. Petroff, B. D. Gerardot, Electro-Elastic Tuning of Single Particles in Individual Self-Assembled Quantum Dots. *Nano Letters* **12**, 3761-3765 (2012).

31. F. Ding *et al.*, Tuning the Exciton Binding Energies in Single Self-Assembled InGaAs\GaAs Quantum Dots by Piezoelectric-Induced Biaxial Stress. *Physical Review Letters* **104**, 067405 (2010).

32. Y. H. Huo *et al.*, A light-hole exciton in a quantum dot. *Nat Phys* **10**, 46-51 (2014).

33. AkopianN, WangL, RastelliA, O. G. Schmidt, ZwillerV, Hybrid semiconductor-atomic interface: slowing down single photons from a quantum dot. *Nat Photon* **5**, 230-233 (2011).

Chapter 5 Properties of WSe_2 single quantum emitters

5.1 Introduction

In the previous chapter, the emitter localisation has been correlated with the point-like local strain gradients. This chapter presents the detailed spectroscopy of such strain-induced quantum emitters hosted by mono- and bilayer WSe_2. In order to characterise the SQEs, results from a number of measurements are presented here. The section opens with PL spectroscopy of the atomically thin WSe_2 host. Next, the purity of single photon emission is quantified. Using high-resolution spectroscopy, their optical features (e.g. linewidth, lifetime, emission energy) of emitters, their stability, and their behaviour under various conditions (temperature, magnetic field etc.) are studied. The statistics of emission energy gathers information about their confinement and the likelihood of appearance. The magneto-optics and polarization-resolved measurements are used to categorise the emitters, and 3 such groups are identified. Although our understanding of WSe2 SQEs is still incomplete, the optical characterization offers a gateway to uncover the intrinsic properties and nature of these emerging quantum emitters.

Data presented in this chapter was acquired from different types of samples including WSe_2 flakes placed (i) on a flat SiO_2 substrate, (ii) on few-layer hBN on a gold substrate, (iii) a flake suspended over a 4 μm circular hole etched in a Si substrate, and (iv) a SiO_2 substrate with arrays of dielectric nanopillars.

5.2 Photoluminescence of mono- and bilayer WSe_2 and their SQEs

The PL signal from a monolayer WSe_2 sample placed on a flat SiO_2 substrate (type (i)) typically features a rich spectrum that consists of two broad (~10 meV) peaks which are associated with the delocalised quantum-well neutral exciton (2D-X0) emitting at 1.74 eV (~710 nm) and a charged exciton or trion (2D-XT) at 1.71 eV (724 nm) as shown in Figure 5.2.1a[*1*] (for T = 4K and P_{exc} = 12 μW). At lower energies, the spectrum also exhibits a broadband emission centred around 1.67 eV (741 nm) which is typically assigned to an ensemble of defect-bound excitons [*1, 2*]. A summary of the central energies, linewidths and the shift from the optical bandgap of all peaks is presented in Table 5.2.1.

By analysing the spectrum one can deduce a few insights about the sample. First, the intensity ratio of 2D-X0 to 2D-XT indicates the amount of doping in the sample. Beside the intrinsic doping, it could also originate from flake's interaction with its environment - the substrate, residue from chosen transfer technique and molecules in the atmosphere

	2D-X0	2D-XT	defect band	2L WSe_2
central energy (eV)	1.74	1.71	1.67	1.59
central wavelength (nm)	711	724	741	780
FWHM (meV)	11.5	15	51	35
energy shift from 2D-X0 (meV)		31	71	155

Table 5.2.1 – A summary of spectral lines featured in monolayer and bilayer WSe_2 on a flat SiO_2 substrate in terms of their central emission energy and wavelength, linewidth (FWHM), and the relative to 2D-X0 energy separation.

which could interact with the sample via atomic vacancies. Further, the separation between 2D-X0 and the 2D-XT of ~31 meV directly measures the trion binding energy. This implies that 2D-XT could survive even at room temperature where the thermal energy reaches 25 meV[*3*].

The peak linewidth signifies the amount of inhomogeneous broadening. The broadening could be related to dephasing mechanisms caused by scattering with defects, charge noise, interaction with phonons and fluctuations in dielectric and strain landscapes. For the 2D excitons, it is illuminating to realise that the measured 2D-X0 linewidth of 11 meV is an order of magnitude larger than the homogenous linewidth (0.33 meV) given by a measured lifetime of 2 ps[*4*]. Interestingly, a simple encapsulation of monolayers in high quality hBN reduces the linewidths of 2D-X0 to around 2 meV in MoS_2 [*5-7*]. This clearly demonstrates the crucial role played by the environment in influencing optical

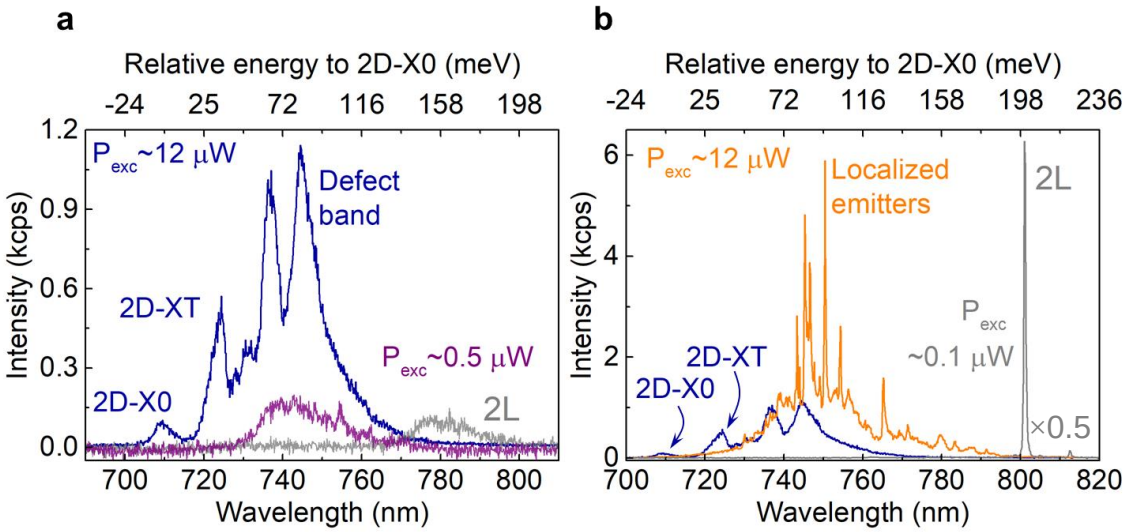

Figure 5.2.1 – **(a)** Representative PL emission from monolayer and bilayer WSe_2 on a flat SiO_2 substrate under high and low excitation powers. **(b)** An example of PL emission from localized SQEs hosted by monolayer and bilayer WSe_2 (from strain sites defined by dielectric nanopillars, type (iv) sample) superimposed on the spectrum from **a**.

properties of TMDs. On the other hand, in Figure 5.2.1a defect ensemble with broad and smooth lines hints at a large population of potential traps acting as recombination sites that overlap spectrally and spatially.

In stark contrast to the monolayer, the PL emission from bilayer WSe_2 is dim and almost featureless. This is consistent with the insights from DFT calculations which predicts the transition from direct to indirect semiconductor. This makes the bilayer an inefficient emitter due to the additional momentum required to satisfy the radiative recombination. Despite this, at elevated powers, bilayer PL emission is still detectable and occurs at 1.55 eV (800 nm), 200 meV away from the monolayer 2D-X0[*8*].

While PL spatial maps of monolayer flakes reveal that the high-power spectrum from Figure 5.2.1a remains homogenous across the majority of each sample, there are some locations where the spectrum develops an intense comb-like appearance as presented in Figure 5.2.1b. Although the SQEs in the spectrum overlap with the broadband defect-bound emission (Figure 5.2.1a), the precise definition of "defects" in this case is still to be confirmed. In the previous chapter, the SQE localization was linked to local strain pockets, creating a powerful technique to induce a clean spectrum with a single dominant SQE, an example of which is PL of bilayer SQE in Figure 5.2.1b marked in grey. Both spectra of SQEs were taken from regions of highly localised strain gradients of the flakes transferred onto a nanopillar array, from type (iv) sample.

5.3 Single photon purity

Purity is an important characteristic of any single photon source, as outlined in the introductory chapter 1. Here, I present the purity of localized emitters hosted by WSe_2 as measured with the Hanbury Brown and Twiss (HBT) intensity interferometer to record the second-order correlation function, $g^{(2)}(\tau)$. The working principle of HBT interferometer was described in the method section, Chapter 2.

The first published $g^{(2)}(\tau)$ results from WSe_2 emitters (type (i) samples) used aggressive spectral filtering to prove the antibunched emission ($g^{(2)}(\tau) < 0.5$)[*9-13*], although the purity was relatively poor. Here, all studied emitters are induced by local stain perturbations leading to background-free, spatially and spectrally isolated spectral lines. This is particularly beneficial because the outcome of $g^{(2)}$ highly depends on the quality of filtering where background from other neighbouring emitters can easily hinder the experimentally measured single-photon purity.

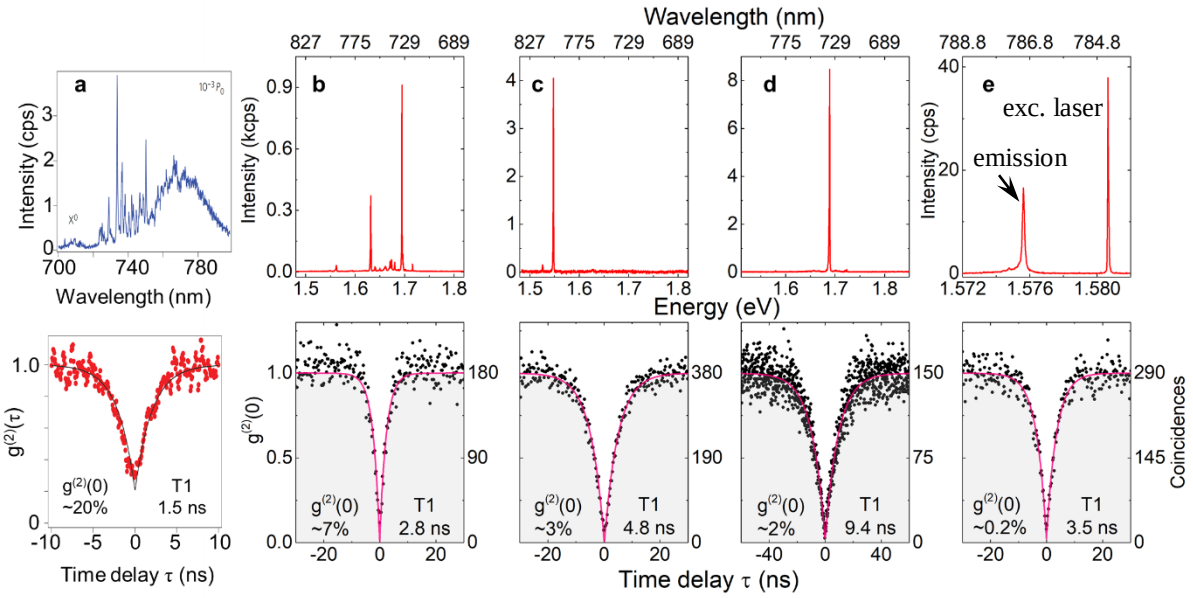

Figure 5.3.1 – **(a-e)** Emissions from WSe_2 SQEs (top panel) paired up with the results of the second-order correlation function $g^{(2)}(\tau)$ (bottom panel) which shows measured values of single photon purity $g^{(2)}(0)$ and the lifetimes of the exciton τ. Emissions originate from **(a)** a randomly found emitter; **(b)** deterministically strain-induced emitter in monolayer and **(c)** bilayer with a dielectric nanopillar; **(d-e)** emitters from highly strained regions in the proximity of a rough gold surface. Arrows in the top panel mark the line filtered for autocorrelation measurement. All emitters were excited with 532 nm laser apart from e where the laser (included in the spectrum) is only 5 meV above the emission. Both figures in a were adapted from [10] type (i) sample, **b,c** from [15] type (iv) sample, and **d,e** from [16] type (ii) sample.

Figure 5.3.1, in the bottom panel, displays and compares results of $g^{(2)}(\tau)$ generated by emitters hosted by monolayer and bilayer WSe_2, paired with corresponding spectra shown in the top panel. Each spectrum exhibits an emitter with a high degree of spectral isolation which, combined with appropriate filtering, directly leads to improved purity. Types of samples associated with the results are listed in the caption of Figure 5.3.1. The purity of randomly distributed emitters found in WSe_2 samples supported by a flat substrate (from the first reports, Figure 5.3.1a, $g^{(2)}(0) = 0.20$) can be slightly improved when emitters are red-shifted away from the overcrowded comb-like emission, done with localised strain fields by placing a monolayer over a hole, few μm in diameter ($g^{(2)}(0) = 0.17$, shown in [*14*], type (iii) sample). When the point-like strain fields are further engineered and applied with a nano-sized pillars, the spectrum becomes much cleaner, containing only a few, bright and dominant emitters as seen in Figure 5.3.1b-d. In such circumstances, the $g^{(2)}(0)$ can be as good as a few percent for mono(bi)layer WSe_2 [*15*]. The background can be further reduced by abandoning non-resonant, far above the optical bandgap excitation. The best result of $g^{(2)}(0) = 0.2\%$ was achieved with near-resonant excitation via a blue-shifted exciton state[*16*] which eliminated any stray PL emission and allowed for

convenient filtering of the pump laser. Although SQEs hosted by 2D crystals are very new, the level of purities presented here have already reached competitive levels, a promising prospect for this emerging 2D solid-state quantum photonic platform.

In addition to quantifying the single-photon purity of the source, the fitting parameters of $g^{(2)}(\tau)$ also provides the value for a characteristic time, τ_c, needed to generate a second under continuous wave illumination. At low excitation powers, this is equivalent to the lifetime of the exciton. The lifetimes of SQEs, shown in the lower panel of Figure 5.3.1, are roughly a few nanoseconds, equivalent to linewidths of the order of 0.1 μeV (i.e. τ_c = 4 ns implies linewidth of 0.15 μeV due to Heisenberg's uncertainty principle). This is in stark contrast to the spectrally measured linewidths which vary between 60 and 300 μeV, 3 orders of magnitude larger than their Fourier transforms.

The discrepancy in the linewidth suggests the presence of large charge noise in the environment, perhaps in part driven by the non-resonant excitation. This causes spectral fluctuations that occur faster than the experimental acquisition time, leading to an increased, time-averaged, linewidth. In order to obtain transform-limited linewidths, the legitimate proposals of controlling environmental noise might involve obtaining better quality crystals, hBN encapsulation, charge tuning and resonant fluorescence to engineer and reduce residual charges. However, so far, it appears that 3D confined excitons experience an even greater departure from transform-limited linewidths than delocalised 2D excitons. This also suggests that unless the source of noise is identified and minimised, we are unable to experimentally access coherence times of WSe_2 SQEs which is significantly jeopardized by dephasing mechanisms.

5.4 High resolution spectroscopy

The spectrum in Figure 5.4.1a represents a typical single emitter in a type (iii) sample. A doublet with ~100 μeV linewidth peaks (separated by Δ = 726 μeV) is observed. In this case the peaks of the doublet have highly unequal intensities. In the inset of the Figure 5.4.1, the time trace reveals the spectral jitter which signals that both lines of the doublets experience the same charge noise, a strong hint that they originate from a single emitter. This will be further confirmed by the Zeeman effect and the relative phase of their polarisations. Nevertheless, the presence of a doublet indicates an emission from a neutrally charged exciton with a broken confinement symmetry. The broken symmetry in the confinement leads to mixing of the two neutral excitonic states which results in splitting the emission into two lines. The mixing of states happens due to the

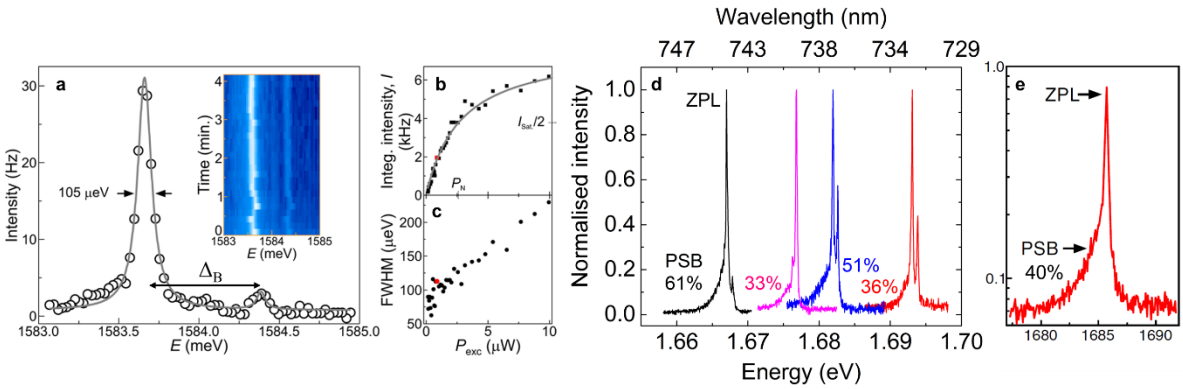

Figure 5.4.1 – **(a)** High resolution PL spectrum of a typical single emitter hosted by monolayer WSe_2. The grey line is the fit of two Lorentzian peaks which gives values for linewidths (~100 μeV) and the fine-structure splitting (~700 μeV). The inset displays the time trace of the emitter where spectral co-wandering is observed. **(b-c)** Power dependences of integrated intensity in **b** and linewidth of the low-energy line in **c**. The grey line in **b** is the saturation curve fit. The red data point corresponds to the spectrum in **a**. **(d-e)** Examples of doublets in **d** and a singlet in **e** with a significant phonon sideband where its relative contribution to the total integrated intensity is noted. Data in **a-c** from type (iii), in **d** from type (ii) sample, but the blue spectrum (at 737 nm) is from type (ii) sample, and in **e** from type (ii) sample.

electron−hole spin-exchange interaction and the splitting in the energy is referred to as a fine structure splitting (FSS) [*17*]. The magnitude of the FSS in the order of 700 μeV in WSe_2 emitters, significantly larger than in self-assembled QDs which typically show splittings of <100 μeV [*18*]. In epitaxial QDs the symmetry breaking is dominated by their usual physical shape of elongated islands; in WSe_2 the reason for such large FSS is still not fully understood. However, this is likely to be caused by a large long-range exchange energy facilitated by the large Coulomb interaction.

In Figure 5.4.1b, the intensity of the doublet shows a clean saturation behaviour consistent with a two-level system with a linear trend at low excitation powers and a plateau at high powers. The two-level system picture is further confirmed with a theoretical fit using the relation $I = I_{sat}\,(P_{exc} / (P_{exc}+P_n))$ which reflects closely the data and gives the parameter of $P_n = 2.78$ μW, where P_n is the normalization excitation power at which integrated intensity of the emitter becomes half of the saturation integrated intensity (I_{sat}). At the lowest power for which the intensity of the emitter is still practically measurable, the linewidth of the emitter reaches the resolution limit of the spectrometer (~60 μeV).

Increased excitation power affects the inhomogeneous broadening, as shown in the Figure 5.4.1c. This is a well-known phenomenon which occurs under non-resonant excitation conditions due to fluctuating charges in the proximity of the emitter. This suggests that

swapping non-resonant with resonant excitation can provide a way to reduce the inhomogeneous broadening and perhaps lead to transform-limited linewidths.

Another common feature of WSe_2 SQEs observed with high resolution spectroscopy is a weak broad band at low energy accompanying the main peak, which can be associated with a phonon sideband (see Figure 5.4.1d,e). While the importance of the phonon sideband is very well known in QDs and defects in diamond, it is fairly unexplored in SQEs hosted by 2D. Although weak, the phonon sideband contribution to the total intensity can be as high as 61% and does not show a clear trend as a function of emission energy as seen in Figure 5.4.1d. The average phonon side band contribution was measured to be around 41±12%, a significant fraction which is likely to hinder the prospects for indistinguishable photon sources. However, in some cases, the PSB is as small as ~20% of the overall emission. Further, the sometimes considerable PSB could be used as a resource for spin readout.

5.5 Polarisation measurements

The emission lines of the neutral exciton with a fine-structure splitting should show distinct optical selection rules which can be assessed by measuring their polarisation, as shown in Figure 5.5.1a. For neutral exciton emission, one could expect a doublet of equal intensities with orthogonal linearly polarized lines [*17*]. However, the polarization-resolved spectroscopy of most doublets in WSe_2 reveals non-orthogonal phase between lines which have unequal intensities, an example of which is presented in Figure 5.4.1a. Doublets with almost orthogonal phase difference ($\Delta\theta$ ~82°) and unequal intensities are also observed, as shown by polarization-resolved intensity contour map in Figure 5.5.1c and polar plots of each emitter in Figure 5.5.1c-e, suggesting that both features are not necessary connected. In fact, the phase varies considerably between 40 and 90 degrees (see Figure 5.5.1c). The spread in phases can be tentatively attributed to the presence of anisotropic strain, as has been observed in epitaxial QDs[*19*]. The physical reasons for observing unequal intensities are even more tentative. However, the majority of doublets show a trend where the high-energy peak is more intense than the low-energy peak which might indicate that their decay rates are different. One could go one step further and suggest that there is a dephasing process which impacts the high-energy peak more than the low-energy peak, but at the moment this is speculative and further work is required.

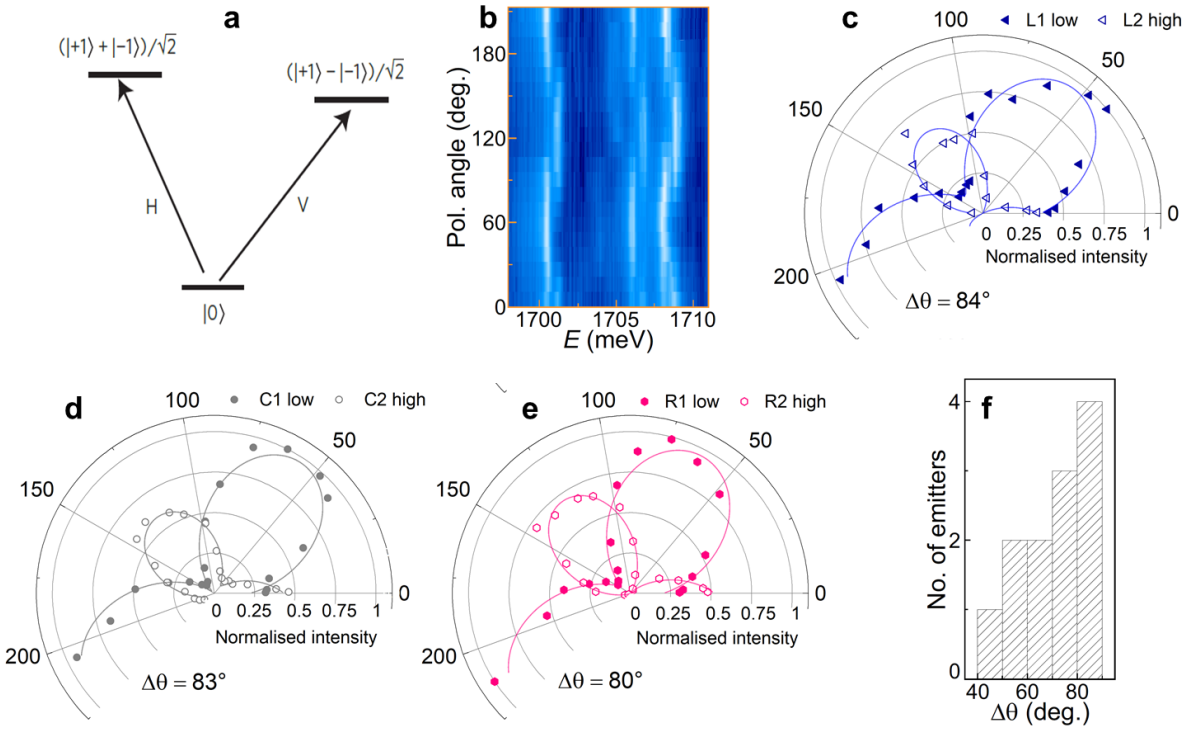

Figure 5.5.1 – **(a)** Energy ladder and optical selection rules of a fine-structure split exciton. **(b)** A contour map of PL intensity as a function of collection polarization angle. **(c-d)** Polar plots of intensity including two lines of all doublets from **b**, labelled as Left, Centre, and Right, where low energy peak is marked by solid markers, high energy peak by open markers. **(c)** Histogram of polarization phases Δθ between the two peaks of 12 doublets.

5.6 Magneto-optics

Another distinct feature of localised excitons is their behaviour under magnetic field (B) which can be used to categorise WSe_2 emitters and to confirm the presence of FSS. In the Faraday geometry, where the magnetic field is applied in the direction perpendicular to flake plane, emitters follow three distinct trends. (i) Doublets are separated by a large 0.6 - 0.8 meV FSS and show a large (~8) g-factor. Their peaks are linearly polarised with a non-orthogonal phase shift and unequal intensity (an example of which is the emitter in the Figure 5.4.1a), but not exclusively. (ii) Doublets with smaller (0.3 meV) FSS and a negligible g factor where both peaks are co-linearly polarised[*16*]. (iii) Single peaks without measurable FSS and minimal Zeeman splitting[*11*].

Figure 5.6.2 displays examples of emitter categories (i) and (ii). With increasing magnetic field, the splitting lines of type I doublets (Figure 5.6.2a) differ from the unchanged emission of a doublet of type II (Figure 5.6.2d). The polarization-resolved intensity maps further distinguish the emitters. In Figure 5.6.2b, lines with unequal intensities, non-orthogonal (40° phase difference) linear polarizations and a large ~0.7 meV Zeeman splitting are observed. This is in stark contrast to the emitter (from Figure 5.6.2e) for

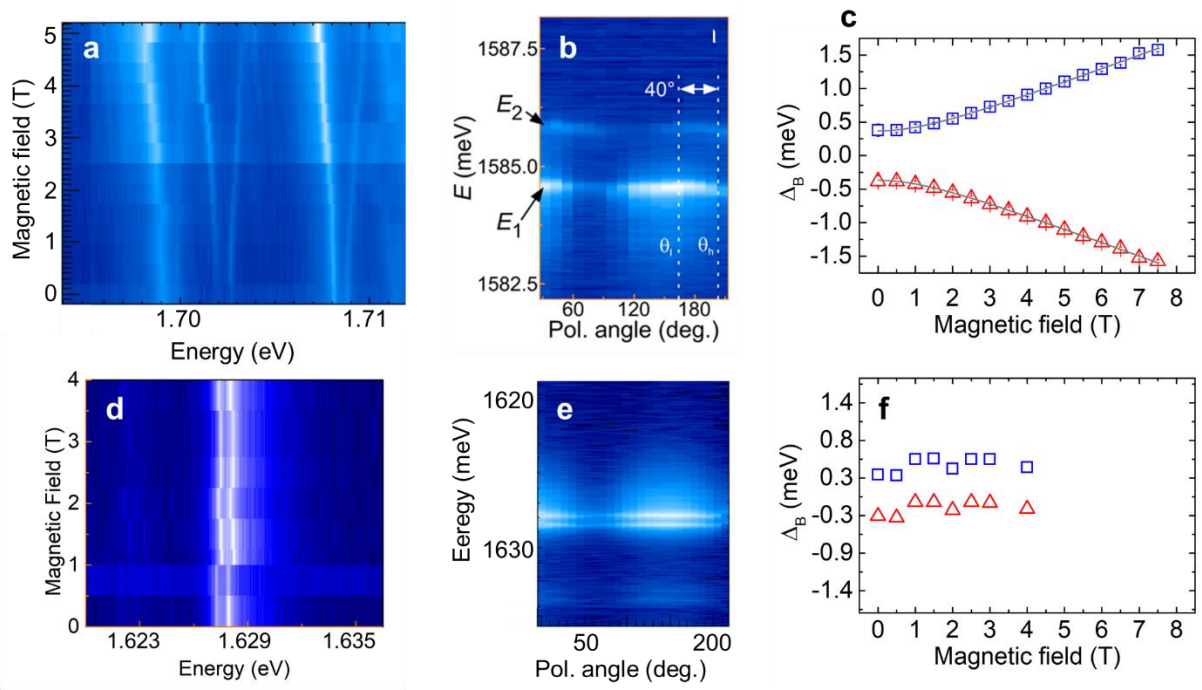

Figure 5.6.2 – **(a)** PL intensity map as a function of applied magnetic field in Faraday geometry featuring two emitters of type I that show large g-factors. **(b)** PL intensity map of polarization resolved doublet emission taken at 2.5 T where the phase difference is 40° suggesting the presence of anisotropic local strain. **(c)** The magnetic field dependence of the doublet from **a**, split by the fine-structure (~ 0.7 meV). The grey line is the fit to the data following the relation Δ_B mentioned in the main text which gives the value of fitting parameter, the g-factor of ~7. Diamagnetic shift has been subtracted from the data. **(d-f)** Counterparts of figures from the top panel **a-e** including an emitter of type II which shows distinct magneto-optical properties. The magnetic dependence in **d** shows no sign of a shift. The polarisation dependence in **e** reveals linearly polarized lines of equal intensities. The peak trace in magnetic field in **f** confirms insensitivity to the magnetic field.

which the lines are equal in intensity, linearly polarized and matching in phase and show slightly smaller splitting at zero magnetic field, equal to 0.63 meV.

As shown by Figure 5.6.2c, with applied field B, the type I follows the relation $\Delta_B = \sqrt{\Delta_0^2 + (\mu_B g_{0D-X} B)^2}$, where Δ_B is the FSS, μ_B is the Bohr magneton and $g_{0D\text{-}X}$ is exciton g-factor. The data closely adheres to the theoretical curve with the fitting parameter, $g_{0D\text{-}X} = 7.16 \pm 0.02$, affirming that the entire doublet arises from a single neutral exciton. Such large values of $g_{0D\text{-}X0}$ are not understood and requires further work. A striking comparison can be made to none g-factors of type II emitters, as displayed in the Figure 5.6.2f.

As magnetic field increases, the central emission ($E_{avg.}$) of the type I doublet also increases in energy, but this time following a quadratic relationship $\Delta E_{avg} = E_{avg}(B) - E_{avg}(0) = \gamma B^2$, where γ is the diamagnetic coefficient, with a fitted value

of γ = -3.9 ± 1.0 μeV/T^2. The diamagnetic coefficient reflects contributions from spatial confinement and interparticle Coulomb interactions. As the exciton wave function gets compressed by the magnetic field, the binding energy increases while the overall diamagnetism gets reduced. Typically, the area of the wave function is proportional to the diamagnetic shift, the very small value of measured γ indicates very strong confinement of neutral exciton. However, the negative sign of γ which is contrary to the one found in epitaxial QDs[*20*] and can be associated with very strong Coulomb interactions acting in the opposite direction to the diamagnetic shift. This is because negative diamagnetic coefficient would mean magnetic field-driven expansion of wave function which is physically impossible.

5.7 Emitter stability

An expectation, drawn from experience with III-V quantum wells and self-assembled QDs[*21*], suggests that a quantum emitter exposed at or just in the proximity to a surface should suffer a severe nonradiative recombination, inhomogeneous broadening, photobleaching and photoblinking caused by nearby surface states. In contrary, the localized states in WSe_2, perhaps aided by the strong exciton binding energy, at least in the first sight do not exhibit such deleterious features. Furthermore, the sp^2 bonding of the host crystal eliminates dangling bonds (in principle) and ensures that the electronic cloud is localized at the transition metal atoms, fully contained within the monolayer. Therefore, one could expect that the localized states are relatively well protected from the influence arising at the surface. However, WSe_2 emitters suffer from a significant spectral wandering which is considered in this section.

Monitoring spectra over a long period of time gages the stability and provides statistics of the spectral fluctuations which can be quantified after computing histograms. Figure 5.7.1 displays emitters from type (iv) samples. Figure 5.7.1a shows a contour PL intensity map containing a time trace of a WSe_2 emitter lasting 20 hours with 2-second binning. The doublet split by ~590 μeV shows no signs of photobleaching, blinking, or deterioration. The results of frequency analysis of another emitter hosted by monolayer (bilayer) are shown in the top (bottom) panel of Figure 5.7.1b-d. The corresponding spectra are shown in Figure 5.7.1b with noted linewidths. For the monolayer emitter, the energy and intensity histograms (Figure 5.7.1c,d) were computed from a time trace of 82 min with 5 second acquisition time. The bilayer emitter was monitored for 24 hours with 3-second acquisition intervals. The histograms of the spectral fluctuation relative to the central emission (low-energy line for monolayer emitter) in Figure 5.7.1c are fit well

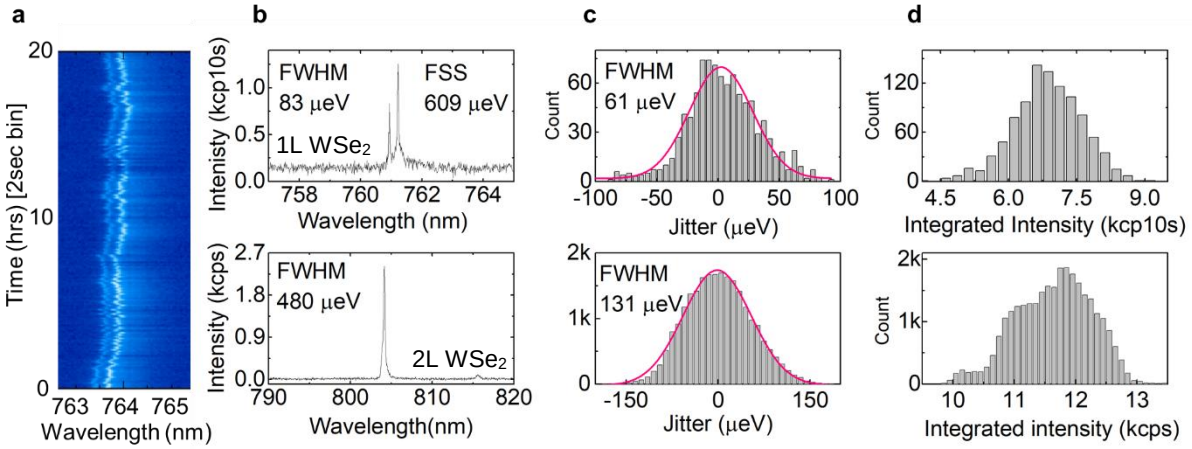

Figure 5.7.1 – **(a)** PL intensity map of a 20-hour time trace binned with 2sec from a WSe_2 doublet which shows spectral wandering but a lack of photobleaching or blinking. Top (bottom) panel presents stability analysis for an emitter from monolayer (bilayer) WSe_2 with **(b)** a PL spectrum, **(c)** histogram of the central emission relative to the mean fitted with a Gaussian peak and **(d)** histogram of the integrated intensity. All emitters are from type (iv) sample.

by a Gaussian function with a single standard deviation of 63 (131) μeV for mono(bi)layer, respectively. This slow spectral jitter is sufficient to prevent further experiments and future applications involving quantum coherence. Finally, the histogram of integrated intensity displayed in Figure 5.7.1d confirms the stability indicating no signs of blinking, bleaching or long-term deterioration.

5.8 Single quantum emitter inhomogeneous distribution

The particular emitter in Figure 5.4.1 is spectrally isolated with central wavelength at 782.82 nm, equivalent to a red-shift of 159 meV from the unstrained 2D-X0. This implies that the emitter emerges from a quantised state deeply confined within the optical bandgap of the material. In Figure 5.8.1, a histogram of another 285 emitters (all from type (iv) sample) reveals that the emission wavelength, (and hence the confinement) of SQEs varies greatly, spanning ~200 meV between 720 and 820 nm (1.72 - 1.51 eV). All emitters appear at lower energy than the 2D exciton peak (~1.74 eV). Fitting a Gaussian to the inhomogeneous distribution gives a FWHM of 73 meV. While the histogram does not favour any particular wavelengths which could be associated with distinct types of confinements, the largest number of emitters (including the most intense) are found around 750 nm (1.65 eV). Furthermore, the blue curve in Figure 5.8.1, which represents an accumulation of the number of emitters as a function of increasing wavelength showing that almost 50% of emitters occur within 740 – 760 nm spectral window. Therefore, the spectral window of 750 ± 10 nm is the most likely place for the most intense SQEs in monolayer WSe_2.

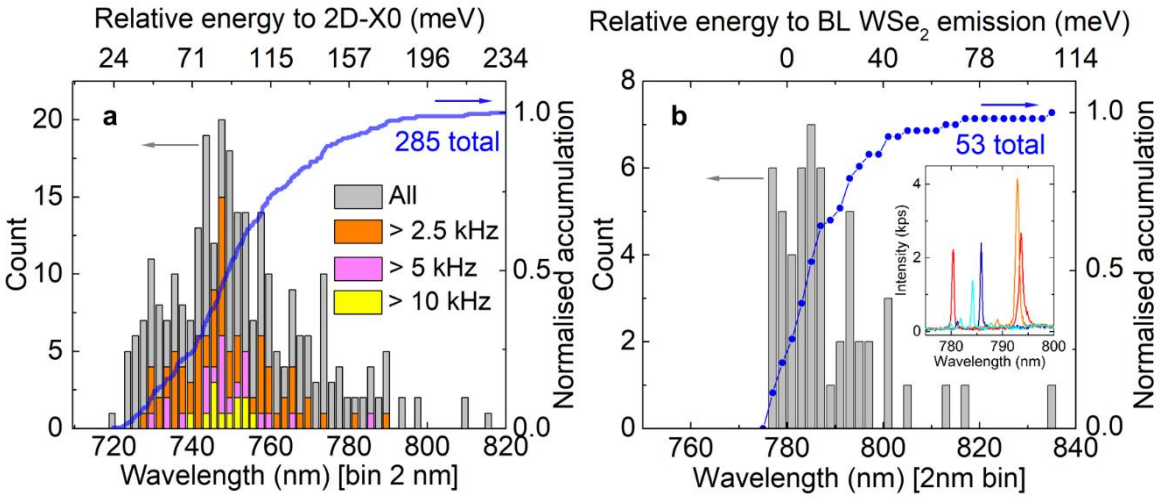

Figure 5.8.1 – **(a-b)** Histogram of the emitter wavelengths from monolayer in **a** and bilayer in **b**. Different colours indicate the brightness thresholds for the peak intensity at 0.8 saturation level. The blue lines are the accumulative number of emitters when counting the emitters at lower wavelengths first. Inset shows two examples of BL WSe_2 emitters with very similar emission energies at 785 nm (blue and light blue spectra), and at 793 nm (orange and red spectra).

The same statistics has been gathered from SQEs hosted by bilayer WSe_2 (53 in total) as shown in Figure 5.8.1b. In bilayer WSe_2, the inhomogeneous distribution is 33 meV, 2 times narrower than in monolayer WSe_2 emitter. In the bilayer, the emitters cover a narrow spectral window between 775 and 835 nm. As the wavelength distribution of bilayer emitters is narrower, it is more possible to observe emitters with matching wavelengths, as shown in inset of Figure 5.8.1b, emitting at 785 and 793 nm. More than 50% of emitters in bilayer occur between 776 – 788 nm (12 nm).

5.9 Temperature dependence

Temperature-dependent spectroscopy is a useful characterisation technique to determine the quantization energy of confined states [*22*]. Figure 5.9.1a shows the evolution of the PL emission from several emitters as the temperature is increased. It is observed that most emitters quench at around 30K but one emitter at around 750 nm survives even beyond 60K. However, to determine energies at which carriers ionize, one need to analyse the reduction of intensity, the spectral shift, and the broadening of the linewidths as a function of temperature. All of these trends are displayed in Figure 5.9.1b-d respectively for two emitters around 740 and 750 nm, which are marked with color-coded data points (pink and black). Solid lines represent fits to the data modelled using equations seen in Figure 5.9.1e, where their fitting parameters are also shown.

In Figure 5.9.1b, the emission energy, $E_g(T)$ was fitted with the Varshani equation[*23*], which reproduces a sudden change in the slope. The average phonon energy ‹ħω›, and the

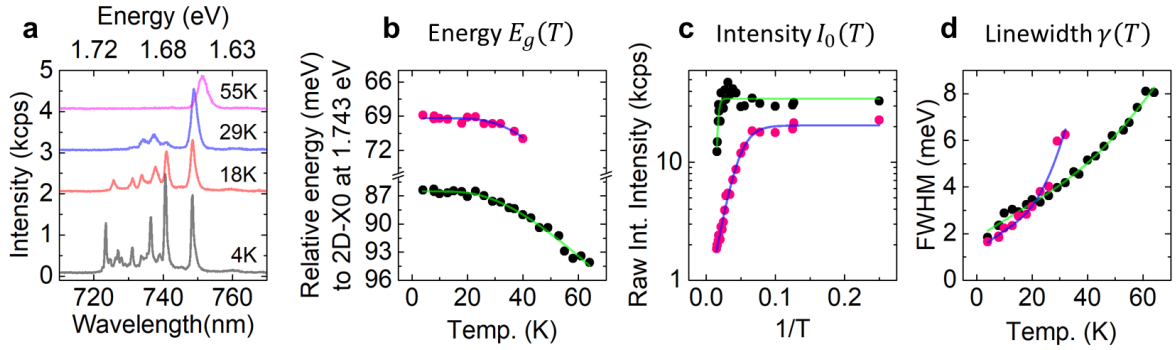

e

	Energy $E_g(T)$	Intensity $I_0(T)$	Linewidth $\gamma(T)$
	$E_g(0) - S\langle\hbar\omega\rangle\left[coth\left(\frac{\langle\hbar\omega\rangle}{2k_BT}\right) - 1\right]$	$\frac{I_0}{1 + Ae^{\frac{-E}{k_BT}}}$	$\gamma_0 + \gamma_{ac}T + \frac{\gamma_{LO}}{Ae^{\frac{E_{LO}}{k_BT}} - 1}$

Label	$E_g(0)$	S	$\langle\hbar\omega\rangle$	I_0	E	γ_0	γ_{ac}	γ_{LO}	E_{LO}
	Emission energy at T=0K	Strength of exciton phonon interactions.	Average phonon energy	Max. intensity at T = 0K	Activation energy	Min. linewidth at T=0K	Acoustic phonon scattering	Longitudinal optical phonon scattering	the activation energy of longitudinal optical phonons
units	eV		meV	kcps	meV	meV	μeV/K	meV	meV
Black 750nm	1.656	1.95±0.18	9.6 ± 0.9	34.5	33.1± 16.7	1.7±0.1	73.1± 7.3	36.3±33.4	10.3 ± 3.9
Pink 740nm	1.674	2.21±0.66	11.9 ± 3.6	20.5	7.1±1.4	1.3±0.1	81.5± 26.9	208 ± 124	11.5 ± 1.4

Figure 5.9.1 – **(a)** The evolution of PL spectra at a few chosen temperatures. **(b-d)** Analysis of two emitters from **a**, at 740 and 750 nm, indicated by consistent color-coded data points, pink and black respectively. **(b)** Spectral shift relative to the 2D-X0 emission energy. **(c)** Integrated intensity of PL emission plotted as a function of inverse temperature. **(d)** Temperature induced line broadening. **(e)** Table containing equations used to fit data sets shown in **b-d**, the description of fitting parameters and their extracted values.

strength of exciton-phonon interaction, *S* (the Huang-Rhys parameter) which relates to an average number of phonons created per one absorbed photon, are extracted. For both emitters these values are at ‹ħω› = ~10 meV and *S* = ~2. The integrated intensity of emitters, in Figure 5.9.1c is modelled with an exponential decay using the Arrhenius rate equation. The fitting parameter, E_a signifies the activation energy of quenching channel through which the carrier escapes the confinement. The fitting reveals a single activation energy for both emitters with values of 26 ± 13 and 7 ± 1 meV for lines at 750 and 740 nm respectively. Finally, the linewidth, shown in Figure 5.9.1d, increases with temperature and was fitted using a combination of linear and exponential components[*22*]. The slope of linear component, γ_{ac} dominating at low temperatures accounts for line broadening due to coupling to acoustic phonons, giving values of ~70 and ~80 μeV/K. At higher temperatures, the exponential component describing the influence of optical phonons becomes the dominant factor in line broadening. Notably, the linewidth trend shows only a subtle deviation from a linear trend causing large errors in γ_{LO} which poses the question

if only a linear trend is more appropriate. For both peaks, the extracted values of the activation energy of optical phonon E_{LO} are ~10 meV.

Strikingly, all characteristic energies, ‹ħω›, E_a and E_{LO}, extracted from the fits, match one another showing values at ~10 meV, which is much smaller than the energy required to reach the optical continuum, lying several tens of meV away from the emission energy. Although these results are preliminary, they suggest that the coupling to optical phonons is the dominant quenching process. Another explanation is that phonons (with energy ~10 meV) allow coupling to a nearby dark state which acts as an effective loss channel[*24*].

5.10 Summary

This chapter presented the optical properties of SQEs hosted by mono- and bilayer WSe_2. The typical PL spectrum originating from the host emphasised the importance of monitoring intensities and emission energies of 2D excitons in order to gain information about the quality of the sample, doping levels and local strain which varies significantly from sample to sample and from point to point. In the case of highly localized and steep strain perturbations, I observe that the broad uniform PL emission of an atomically thin quantum well transforms into a forest of sharp lines that signify SQEs. These strain-induced emitters were investigated in detail throughout the chapter.

I presented second-order correlation from the strain-induced quantum emitter, revealing high single photon purity levels. This is enabled by the ability to create large point-like strain fields as well as a quasi-resonant excitation scheme. Both approaches succeeded at creating background-free single photon emission containing only a few (or even just one) intense emitter(s) which yield single photon purities of less than a percent. These measurements also informed about the exciton lifetimes of the order of few ns. Combined with the saturation behaviour of a few-level system, the single-photon emission validates the interpretation of a new quantum emitter.

The sharp spectral lines were further characterised with the aid of high resolution spectroscopy. The measurements revealed that excitonic emission commonly consists of a doublet called FSS (~ 700 μeV), which often has unequal intensities, large g-factors (~8) and a visible phonon side band (~ 40%). Identifying the origin of these emitters requires further work, but the large FSS likely stems from the large Coulomb interactions in 2D materials. I report 60-μeV emitter linewidth (limited by spectrometer resolution) at low excitation powers, 3 orders of magnitude larger than its transform limit, indicating

significant environmental noise which increases with increasing the non-resonant excitation power and happens within a timescale shorter than the typical spectral acquisition (~1 sec). Spectral wandering occurring at longer time scales (of the order of few seconds) was also observed. The spectral wandering needs to be addressed before two-photon interference measurements can be attempted. The emitter intensity was another aspect of emitter photo-stability which was investigated in great detail. The time traces lasting several hours confirmed the long-term robustness of emission intensity which did not show signs of degradation.

The statistics of emitter emission energies were also presented. In monolayer WSe_2, the histogram displayed a wide spread of energies suggesting a large number of types of confinements, perhaps due to varying local strain profiles. However, the statistics point out a high likelihood of emitters around 750 nm in monolayer. The same statistics in bilayer is twice as narrow and some emitters show nominal matching emission energy.

The behaviour of localized excitons under elevated temperatures (up to tens of K) were analysed in terms of their emission energy, intensity and linewidth. The analysis revealed that the energy on the order of 10 meV was sufficiently large to ionize excitons. The extracted values of average phonon energy ‹ħω›, activation energy of optical phonon E_{LO}, and characteristic loss channel E_a showed similar values, but whether or not optical phonons are fully responsible for quenching the PL emission is still arguable. More data need to be acquired to confirm the general trend.

The magnetic field and polarisation resolved spectroscopy uncovered 3 types of emitters. First, commonly observed doublets show peaks with unequal intensities, near-orthogonal phase shift, relatively large (~ 0.7 meV) FSS and relatively large (~8) g-factors. The reasons for both values to be so large are currently not fully understood, but the large FSS is likely to arise from strong Coulomb interactions present in the host material. In contrary, other categories of emitters exhibit extremely small g-factors and co-linearly polarized lines with more equal intensities. Further work is required to expose the physical reasons for these trends seen with magneto-optics measurements.

This chapter presented characterisation of optical properties of WSe_2 SQEs with numerous techniques. The results provided an insight into the nature of SQEs, exposing new aspects that require further study. Therefore, to expand our knowledge other techniques are required to be implemented as there are many questions yet to be answered. The major unknown concerns the emitter origin, perhaps closely connected to the crystal

quality or strain profiles. Another important aspect is emitter coherence, so far unreported. Moreover, the immediate environment of SQE plays a significant role in influencing the intrinsic properties of the 2D host as well as SQEs themselves, hence controlling the surroundings might become a robust way of eliminating sources of noise and tuning the optical properties of the emitters.

5.11 References

1. A. M. Jones *et al.*, Optical generation of excitonic valley coherence in monolayer WSe2. *Nature Nanotechnology* **8**, 634 (2013).

2. S. Tongay *et al.*, Defects activated photoluminescence in two-dimensional semiconductors: interplay between bound, charged, and free excitons. *Sci Rep* **3**, 2657 (2013).

3. K. He *et al.*, Tightly Bound Excitons in Monolayer WSe2. *Physical Review Letters* **113**, 026803 (2014).

4. C. Robert *et al.*, Exciton radiative lifetime in transition metal dichalcogenide monolayers. *Physical Review B* **93**, 205423 (2016).

5. F. Cadiz *et al.*, Excitonic Linewidth Approaching the Homogeneous Limit in MoS2-Based van der Waals Heterostructures. *Physical Review X* **7**, 021026 (2017).

6. A. A. Obafunso *et al.*, Approaching the intrinsic photoluminescence linewidth in transition metal dichalcogenide monolayers. *2D Materials* **4**, 031011 (2017).

7. J. Wierzbowski *et al.*, Direct exciton emission from atomically thin transition metal dichalcogenide heterostructures near the lifetime limit. *Scientific Reports* **7**, 12383 (2017).

8. G. Wang *et al.*, Exciton dynamics in WSe2 bilayers. *Applied Physics Letters* **105**, 182105 (2014).

9. P. Tonndorf *et al.*, Single-photon emission from localized excitons in an atomically thin semiconductor. *Optica* **2**, 347-352 (2015).

10. A. Srivastava *et al.*, Optically active quantum dots in monolayer WSe2. *Nat Nano* **10**, 491-496 (2015).

11. Y.-M. He *et al.*, Single quantum emitters in monolayer semiconductors. *Nat Nano* **10**, 497-502 (2015).

12. KoperskiM *et al.*, Single photon emitters in exfoliated WSe2 structures. *Nat Nano* **10**, 503-506 (2015).

13. C. Chakraborty, L. Kinnischtzke, K. M. Goodfellow, R. Beams, A. N. Vamivakas, Voltage-controlled quantum light from an atomically thin semiconductor. *Nat Nano* **10**, 507-511 (2015).

14. S. Kumar, A. Kaczmarczyk, B. D. Gerardot, Strain-Induced Spatial and Spectral Isolation of Quantum Emitters in Mono- and Bilayer WSe2. *Nano Letters* **15**, 7567-7573 (2015).

15. A. Branny, S. Kumar, R. Proux, B. D. Gerardot, Deterministic strain-induced arrays of quantum emitters in a two-dimensional semiconductor. *Nature Communications* **8**, 15053 (2017).

16. S. Kumar *et al.*, Resonant laser spectroscopy of localized excitons in monolayer WSe2. *Optica* **3**, 882-886 (2016).

17. M. Bayer *et al.*, Fine structure of neutral and charged excitons in self-assembled In(Ga)As/(Al)GaAs quantum dots. *Physical Review B* **65**, 195315 (2002).

18. S. Seidl *et al.*, Statistics of quantum dot exciton fine structure splittings and their polarization orientations. *Physica E: Low-dimensional Systems and Nanostructures* **40**, 2153-2155 (2008).

19. S. Kumar *et al.*, Anomalous anticrossing of neutral exciton states in GaAs/AlGaAs quantum dots. *Physical Review B* **89**, 115309 (2014).

20. J. J. Finley *et al.*, Fine structure of charged and neutral excitons in InAs-Al0.6 Ga0.4 As quantum dots. *Physical Review B* **66**, 153316 (2002).

21. C. F. Wang *et al.*, Optical properties of single InAs quantum dots in close proximity to surfaces. *Applied Physics Letters* **85**, 3423-3425 (2004).

22. M. Bayer, A. Forchel, Temperature dependence of the exciton homogeneous linewidth in In0.60Ga0.40As\GaAs self-assembled quantum dots. *Physical Review B* **65**, 041308 (2002).

23. K. P. O'Donnell, X. Chen, Temperature dependence of semiconductor band gaps. *Applied Physics Letters* **58**, 2924-2926 (1991).

24. Y.-M. He, S. Höfling, C. Schneider, Phonon induced line broadening and population of the dark exciton in a deeply trapped localized emitter in monolayer WSe2. *Opt. Express* **24**, 8066-8073 (2016).

Chapter 6 Localized emissions from monolayer $MoSe_2$

6.1 Introduction

The discovery of stable, bright and pure SQEs in monolayer WSe_2 encourages the question of if other 2D TMDs can host SQEs too. In fact, already a few 2D crystals such as hBN and mostly TMDs like GaSe, WS_2 were shown to host SQEs (which were outlined in Chapter 1, Section 1.3.5). This poses an interesting prospect of drawing a comparison between quantum emitters in order to understand which properties are inherited from their hosts and to uncover their nature. This chapter presents results on localised emissions from monolayer $MoSe_2$ which is fundamentally distinct to WSe_2. In contrary to WSe_2, the lowest energy transition of $MoSe_2$ monolayer is optically bright, strongly affecting carrier relaxation and recombination dynamics. Perhaps these features of the electronic dispersion can affect the qualities of localized emitters which are presented throughout the chapter.

6.2 Photoluminescence of monolayer $MoSe_2$

The low temperature PL (at 4K) spectrum of monolayer $MoSe_2$ mostly shows two bright and broad (typically 10 meV) peaks centred at 1.659 eV (747 nm) and 1.628 eV (761 nm) which correspond to the delocalised neutral exciton (2D-X0) and trion (2D-XT), respectively. This gives the value for the trion binding energy of 31 meV ($E_{2D\text{-}X0}$ -$E_{2D\text{-}XT}$). These emissions are brighter than their WSe_2 counterparts under similar conditions and are the brightest at low temperatures, a consequence of the bright, spin-allowed transition of the exciton ground state.

Intriguingly, energies of both peaks shift whether metal (gold) or insulating (SiO_2) substrate supports 1L $MoSe_2$ (Figure 6.2.1c). Although the peaks energies change, the trion binding energy display typical values. The finding that the optical bandgap is affected by the substrate is expected taking into consideration the reduced screening in monolayers and significant dielectric difference between gold ($\epsilon_1 = -20.15$) and SiO_2 ($\epsilon_1 = 2.17$ at 750 nm). In order to understand it fully, this feature requires further investigation as a part of engineering Coulomb interaction via adjusting dielectric environment [1]. The substrate also impacts significantly the relative intensities between the exciton and the trion introducing an artificial doping. Moreover, the PL spatial mapping often reveals that the intensity ratio is also locally altered between flakes from the same substrate (see Figure 6.2.1c, spectra no. 4-7) and even within a single flake with modulations spreading spatially over few microns, as shown in. Perhaps, these modulations could be caused by the polymer debris due to the all-dry transfer or due to

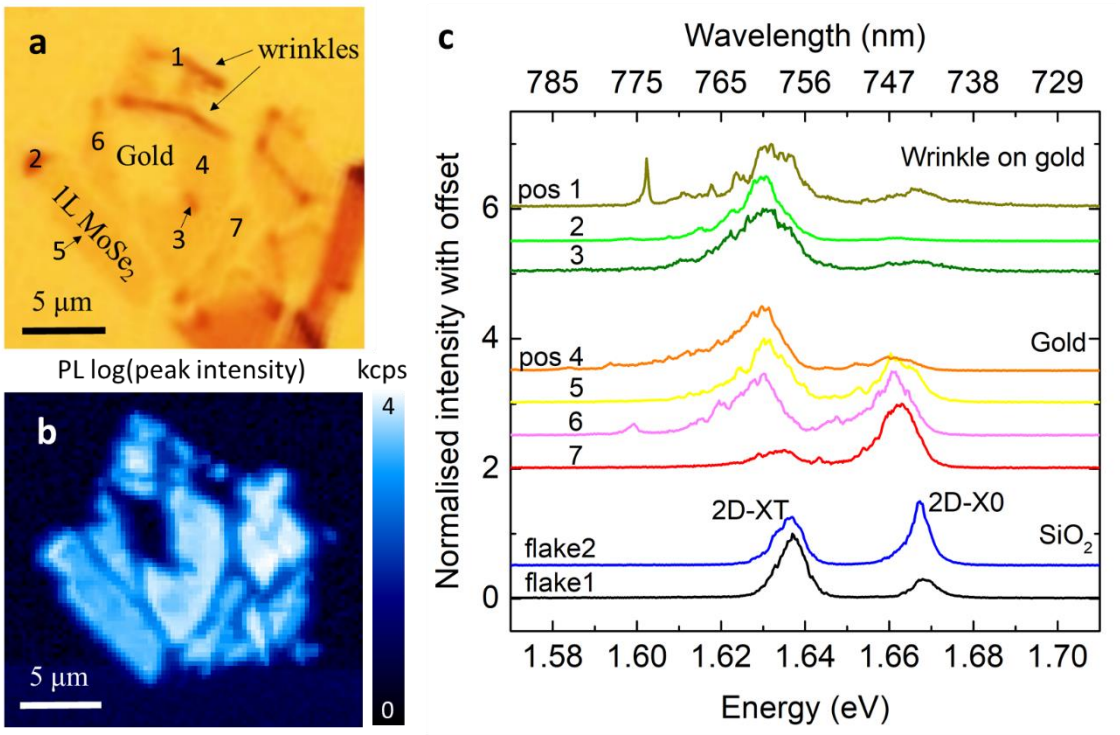

Figure 6.2.1 – **(a)** Optical micrograph of monolayer $MoSe_2$ transferred onto a gold substrate, showing numerous wrinkles which can be identified by increase in the contrast. Numbers correspond to spectra in **c**. **(b)** PL spatial map of peak intensity in logarithmic scale for spectral window between 720 – 800 nm, showing little influence of flake topography on PL emission. **(c)** Examples of spectra from 1L $MoSe_2$ on SiO_2 and gold substrate. Numbered spectra correspond to locations marked in **a**.

non-pristine substrate. Despite the variations, there are still areas of uniform and constant doping levels.

Distinctively, there are also other locations where the spectrum develops sharp emissions. These comb-like spectra feature discrete emission lines with linewidths typically between 150 – 400 µeV, which is broader than those in WSe_2 where sub-100 µeV linewidths are commonly seen. Alike in WSe_2, the sharp emissions from $MoSe_2$ are tightly localised (to the diffraction limit of 600 nm) and also appear below 2D-X0, indicating that they originate from the states inside the bandgap. Their emissions appear to spread continuously over a wide wavelength range reaching 822 nm, 150 meV below the 2D-X0 emission energy, suggesting a high concentration of deeply confined emitters. Further, their spatial distribution is not random but also linked to the flake's termination and locations of local strain (like wrinkles).

To demonstrate this correlation, a monolayer $MoSe_2$ shown in Figure 6.2.2a was mechanically exfoliated and transferred with all-dry technique onto a gold substrate for optical characterisation. During the transfer process, excess shear was deliberately applied to create a wrinkle, identified by the dark line penetrating the micrograph from

the top. The PL spatial raster scan of integrated intensity of the area, marked in Figure 6.2.2a by the black box, reveals the increase of intensity coinciding with the wrinkle. This observation is an indication of exciton diffusion towards the lower energy bandgap due to the strain. Figure 6.2.2b-d present result from hyperspectral analysis of PL maps. They provide information about the location of individual emitters which

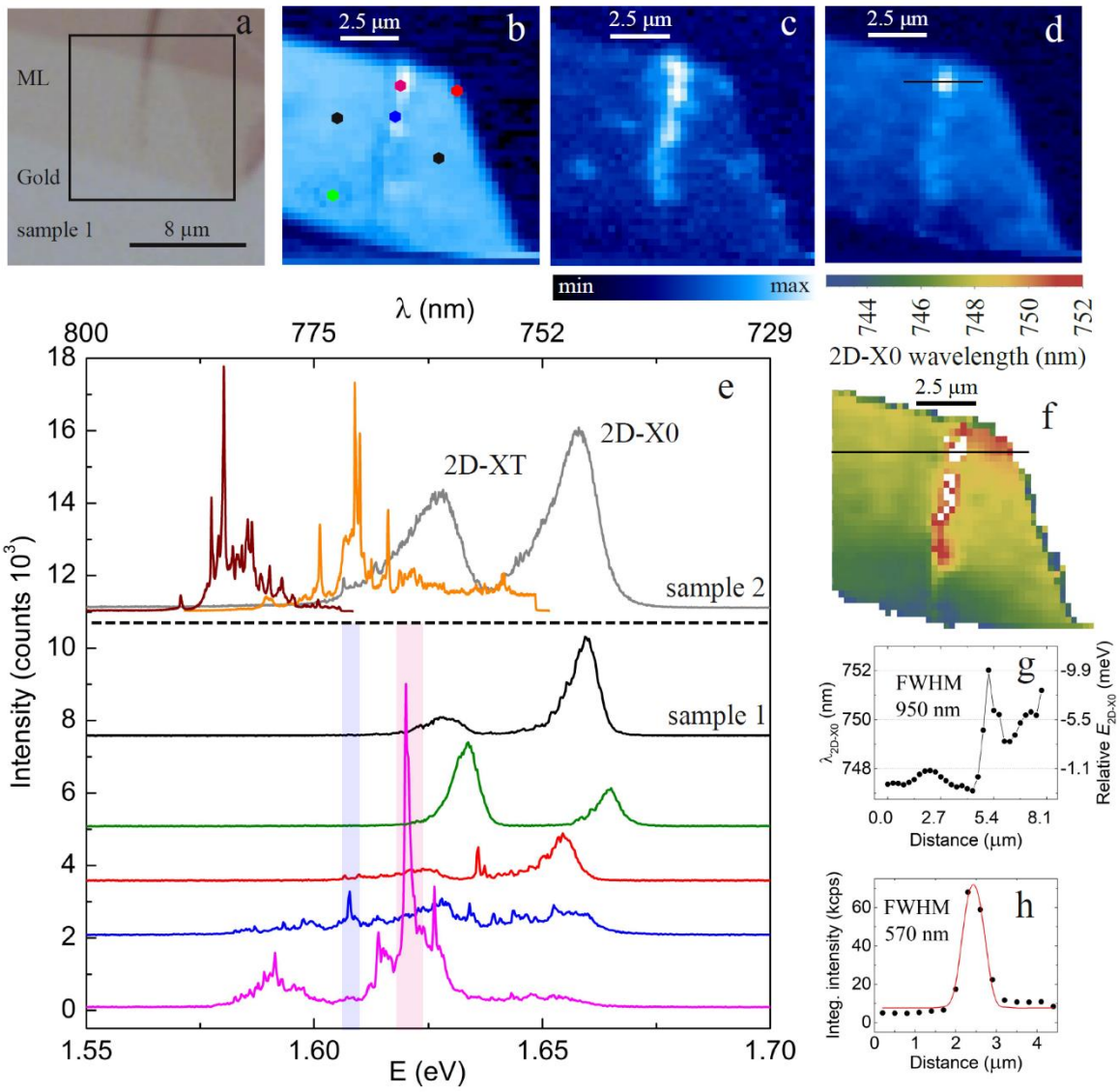

Figure 6.2.2 - **(a)** Micrograph of monolayer $MoSe_2$ placed on gold substrate where the flake formed a wrinkle seen as a line with darker colour. Photoluminescence intensity maps which cover **(b)** the entire spectral window between 683 - 855 nm, the window **(c)** between 770.56 - 771.91nm capturing sharp emission from blue spectrum **(d)** between 764.52 - 765.86 nm for emitter from the pink spectrum **(e)** Typical PL emission spectra for monolayer $MoSe_2$ (the grey and black) from the smooth and unstrained locations of the flake. In colour, examples of sharp, quantum dot-like emissions found at the edges and along the wrinkle. **(f)** Space map of fitted 2D-X0 wavelengths which shows a homogeneous emission apart from the rapid redshift of ~10 meV caused by the wrinkle. The solid includes the pink spectrum at the bottom from **e**. **(g)** Cross section in strain profile across the wrinkle marked in **f** showing 950 nm wide strain pocket. **(h)** Diffraction limited integrated intensity cross section from **d.**

appear as diffraction limited bright spots in the regions of enhanced intensity and at the flake edges. This can be seen in Figure 6.2.2b where these emitter positions were superimposed on the integrated intensity map. The corresponding spectra of marked emitters are presented in Figure 6.2.2e.

To confirm that the sharp emissions are induced by the steep and sudden local strain gradients, the PL map is converted into a strain map by extracting the emission energy of 2D-X0 as shown in Figure 6.2.2f. While the majority of the flake shows smooth modulation of 2D-X0 energy, the map with confined areas of highly red-shifted wavelengths resembles the shape of the wrinkle. The white points are where the strain was so large that emission from the 2D-X0 has vanished, ruling out a reliable fitting. The Figure 6.2.2g(h) show the cross-section along the solid line marked in Figure 6.2.2f(d). The cross-section in integrated intensity includes the pink (bottom) spectrum and confirms diffraction limited localisation length of 570 nm. Another cross-section in 2D-X0 energy provides dimensions and the magnitude of the strain modulation with total 2D X0 shift of 4.5 nm (~10 meV) relative to the average emission and with 950 nm FWHM. Therefore, it appears that sharp emissions from $MoSe_2$, similar to WSe_2, are localized by local strain perturbations of comparable magnitudes and dimensions.

However, the similarity between $MoSe_2$ and WSe_2 does not hold when emitter localisation is strain-induced by naturally occurring corrugations. Corrugations which would induce emitters in WSe_2 were not sufficient for $MoSe_2$. Figure 6.2.1a shows optical image of 1L $MoSe_2$ with several regions with wrinkles. Figure 6.2.1b presents PL map of peak intensity of discontinuous $MoSe_2$ monolayer on gold substrate which contains only a modest number of localized emissions (see Figure 6.2.1c, spectrum no. 1) despite a number of terminations and folds. In contrast, in WSe_2 these circumstances lead to appearance of SQEs. This suggests that in addition to local strain, the dielectric environment is also a decisive parameter in inducing localised emission in 2D $MoSe_2$.

Apart from larger linewidths than those in WSe_2, the optical quality of $MoSe_2$ emitters is further hindered by a densely populated spectrum, non-zero background, large spectral fluctuations (jitter), blinking and power-related deterioration. These unfortunate effects contributed to unsuccessful second order correlation measurement which is summarised by the Figure 6.2.3. The Figure 6.2.3a displays a comparison between $MoSe_2$ and WSe_2 emitters with representative examples. Spectra featuring emitters in $MoSe_2$ often contain several closely spaced lines and a considerable background, in contrast to the clean spectrum of commonly found background-free doublet with unequal intensities found in

WSe_2. Linewidths of $MoSe_2$ emitters are typically > 150 μeV, compared to WSe_2 for which Γ = sub-100 μeV is common. Moreover, contrary to WSe_2, 25-hour long time traces of emitters hosted by $MoSe_2$ that appear to be stable, disclose that, in fact, emitters degrade slowly in time under the influence of moderately low, 0.4 μW excitation powers as shown in Figure 6.2.3b. The Figure 6.2.3c displays spectra at several points in time showing the decay of the optical quality of the emitter.

In addition, as shown in Figure 6.2.3d-g, many emitters in $MoSe_2$ show sagnificant short-term spectral jitter and some even blinking. The spectral jitter is quantified with frequency

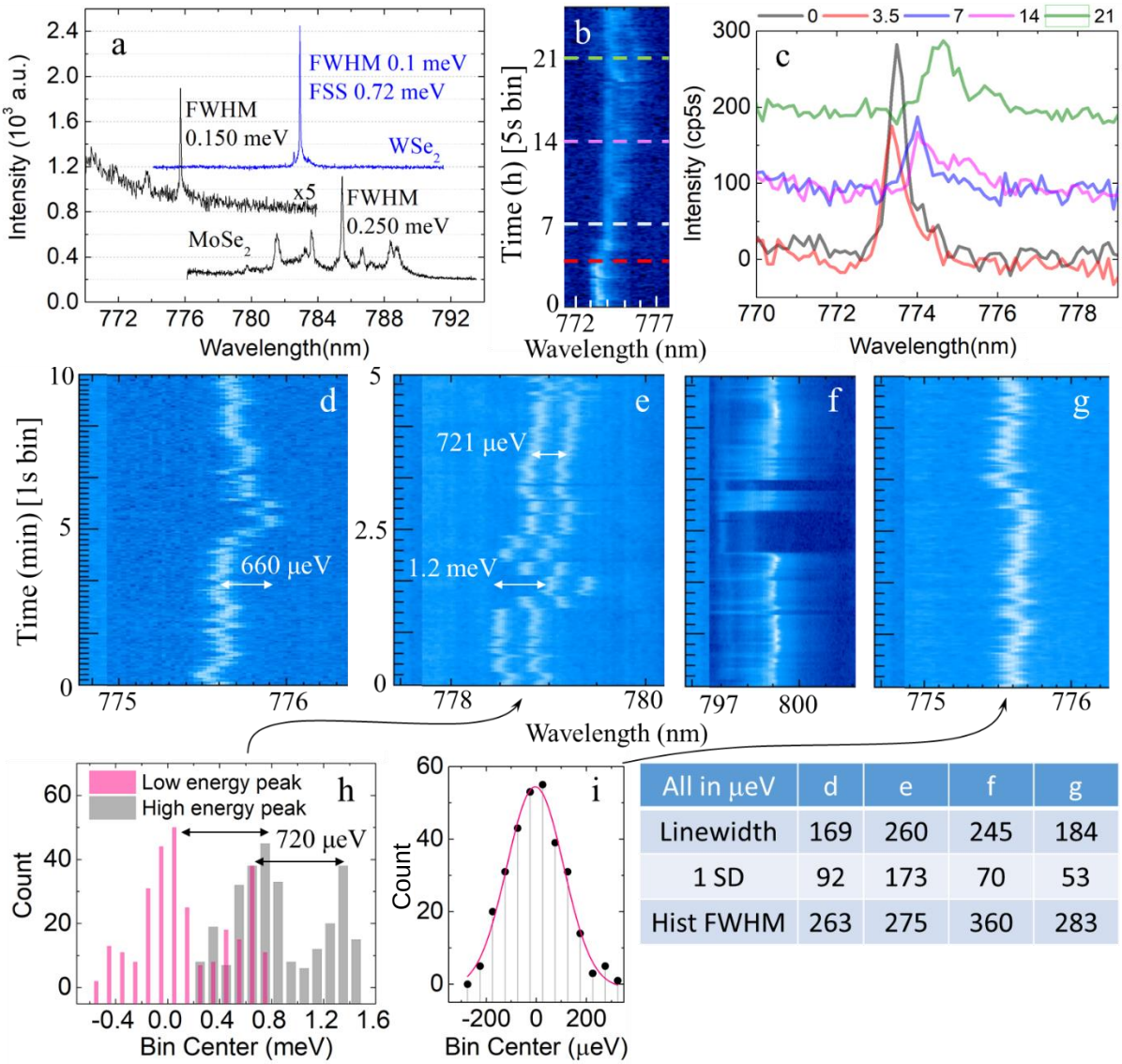

All in μeV	d	e	f	g
Linewidth	169	260	245	184
1 SD	92	173	70	53
Hist FWHM	263	275	360	283

Figure 6.2.3 – **(a)** In blue (black), high resolution, representative spectra of WSe_2 ($MoSe_2$) emitters with their linewidths. **(b)** 25-hour long time trace with 5 sec binning of an $MoSe_2$ emitter showing a slow degradation of the emission quality where color-coded dashed lines correspond to the cross-sections in **c**. **(c)** Spectra of an emitter with an offset at different times marked in **b**. **(d-g)** Emitter stability gauged by short-term time traces that exhibit significant, up to 1.2 meV spectral jitter and blinking. **(h,i)** Histograms of binned emission energy used to quantify the spectral fluctuations for emitters in **e** and **g**. Table outlines results of the jitter analysis for all emitters from **d-g**.

analysis of the time traces with examples displayed in Figure 6.2.3h,i while the table outlines linewidths and the magnitudes for the jitter. Fluctuations in the order of 0.5 meV were found, much larger than in WSe_2, and can be tentatively assigned to enhanced charge noise due to vicinity of the metal surface. It is possible, although hard, to find emitters experiencing small spectral wandering within few tens of micro eV. Ways to improve the optical the optical properties might involve controlling the environment by depleting residual charges with an electric field (in field-effect transistor), altering dielectric environment with hBN encapsulation, and perhaps improving quality of the crystal.

Despite these deficiencies, the post-selection allows to compute $g^{(2)}(\tau)$ with only these photons which contributed to the maximum counts while excluding uncorrelated background photons. However, even after the post-selection and with intensities of 3 kcps on each detector, the $g^{(2)}(\tau)$ still shows uncorrelated statistics which could be due to

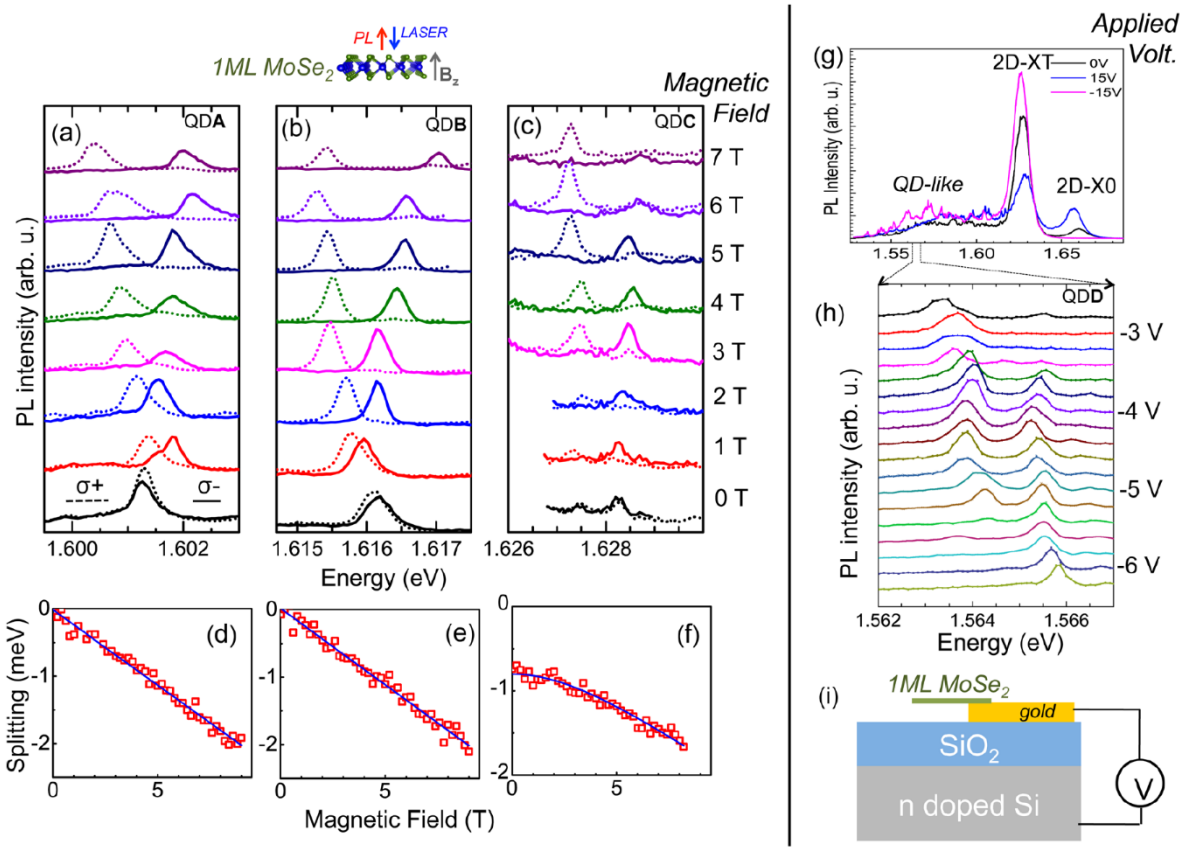

Figure 6.2.4 – **(a-c)** Spectra of localized emissions from $MoSe_2$ subjected to out-of-plane magnetic field and detected in two circular basis, σ^+ and σ^-. While emitters from **a** and **b** do not show measurable fine structure splitting at zero magnetic, the emitter in **c** does and is equal to 800 μeV which is comparable to emitters in WSe_2. **(d-f)** Zeeman splitting of corresponding emitters displayed in **a-c** shows g factors of −4 regardless to the magnitude of the FSS. **(g)** Results of the charge tuning where the emission is modulated by applying electric field. The ratio between 2D excitons is altered as well as discrete emissions. **(h)** Charge tuning of $MoSe_2$ localized emitter which exhibits a 2 meV jump as different voltage is applied **(i)** Schematics of the charge tuning device.

insufficient background to noise ratio or faster recombination dynamics then the time response of the correlating electronics of 300 ps. To this date, the quantum nature of localized emissions from $MoSe_2$ is still to be confirmed. However, there are hints supporting the case such as saturation behaviour which is characteristic to a 2 level system, random in-plane dipoles, disassociation of localized excitons at low temperatures indicating weakly bound states [2,3], magneto-optics behaviour and discrete charge tuning.

Applying a vertical magnetic field brings insight into the type of emitters inhibiting the $MoSe_2$ monolayer, as shown in Figure 6.2.4a-f. Interestingly, the majority of emitters do not show any measurable fine structure splitting at $B_z = 0T$ which is uncommon in WSe_2. There are a few emitters showing a splitting of 800 μeV signifying the strong Coulomb interactions in these materials. Regardless to the magnitude of the FSS, the Zeeman splitting follows g factors equal to −3.9. This value is very similar to the g-factors of delocalized neutral exciton and trion of the 2D $MoSe_2$ host. This similarity alludes to the physical connection between the localised states and the 2D-X0 formed at the K-point which still requires to be further investigated. The magnitudes of g-factors in $MoSe_2$ are considerably smaller to those from WSe_2 which show values between 6 and 13. The physical reasons for large and variable g factors in all 2D materials remain to be explained and uncovering more differences and similarities between hosts will contribute to our understanding about their origin and all deciding parameters.

Finally, the results of charge tuning are shown in the Figure 6.2.4g,h where the external bias controlling the resident carrier density modulated 2D-XT:2D-X0 intensity ratio and induced a discrete jump of localized emitter's energy. Two lines separated by 2 meV represent two distinct charge states. This charging behaviour resembles the one seen in self assembled III-V QDs, which is essential for optical and electrical manipulation of single spins [4].

6.3 Summary

Localized and discrete emitters hosted by monolayer $MoSe_2$ are legitimate members of newly emerging and promising quantum photonic platform based on 2D materials. Outstanding measurements which should provide further insights into the nature of the emitters involve resonant fluorescence, time-resolved PL and the second-order correlation. These experimental shortcomings boil down to the lack of reliable method of inducing emitters which is not as straight forward as in WSe_2. For now, localized emitters overlap spectrally with each other and with bright 2D excitons. Further, the intensity of

2D excitons remain significantly large relatively to the emitters which contributes to the background noise in the correlation measurements. Despite these difficulties, the strain might still be of resource combined with appropriate dielectric screening, for instance with an array of metal nanopillars. Unless this objective is delivered, $MoSe_2$ emitters will remain understudied, despite carrying the same benefits of 2D platform as WSe_2 and the differences that motivates scientific curiosity and future work.

6.4 References

1. A. Raja *et al.*, Coulomb engineering of the bandgap and excitons in two-dimensional materials. **8**, 15251 (2017).

2. A. Branny *et al.*, Discrete quantum dot like emitters in monolayer MoSe2: Spatial mapping, magneto-optics, and charge tuning. *Applied Physics Letters* **108**, 142101 (2016).

3. C. Chakraborty, K. M. Goodfellow, A. Nick Vamivakas, Localized emission from defects in MoSe2 layers. *Opt. Mater. Express* **6**, 2081-2087 (2016).

4. B. D. Gerardot *et al.*, Optical pumping of a single hole spin in a quantum dot. *Nature* **451**, 441 (2008).

Chapter 7 Summary and broad discussion

7.1 Novelty of the work

The main results presented in this thesis are the fabrication and optical characterisation of single quantum emitters in atomically thin WSe_2 and $MoSe_2$ that are spatially positioned and spectrally tuned using nanoscale strain engineering. The results can be also found in published papers [*1-4*].

In Chapter 3, fabrication methods to isolate and deterministically transfer monolayers were introduced. Although the mechanical exfoliation and all-dry transfer technique are well known fabrication procedures, this work presents them in a wider perspective (Sec. 3.1) with an in-depth discussion (Sec. 3.2, 3.4). A review of experimental techniques enabling monolayer identification presented the strengths and shortcomings of numerous equipment allowing for their direct comparison (Sec 3.3).

In Chapter 4, a correlation between localised strain perturbations and the localisation of mono- and bi-layer WSe_2 SQEs is demonstrated for the first time (Sec. 4.2). Steep local strain gradients were associated with naturally occurring, unintentionally induced corrugations such as wrinkles and folds. Further, the correlation between strain and SQEs was exploited to realise, for the first time, an array of deterministically induced, spatially and spectrally isolated SQEs in mono- and bi-layer WSe_2. Here lithographically defined nanopillars were used as a means of local strain engineering (Sec. 4.3). In addition to nanoscale precision, scalability and compatability with other 2D semiconductors (i.e. monolayer $MoSe_2$ presented in Chapter 6), local strain engineering paves the way for deterministic placement of emitters in custom structures (i.e. charge devices, cavities, waveguides) and are useful in revealing the precise nature of the emitters which will be discussed in the following section.

In Chapter 5, I investigated the optical properties of SQEs in WSe_2, primarily using confocal photoluminescence spectroscopy performed under various conditions (i.e. magnetic field, temperature) and Hanbury Brown Twiss interferometry to reveal emitters' intrinsic properties. This work demonstrates that WSe_2 SQEs are pure sources of single photons, showing $g^{(2)}(0) < 0.5\%$ (partly thanks to strain-induced spectral and spatial isolation) and lifetimes on the order of few ns (Sec. 5.3). With high resolution spectroscopy, sub-100 μeV linewidths are also observed, encouraging further work to reduce the linewidth towards the transform limit which currently is approximately 3 order of magnitude smaller. On the other hand, monitoring SQE emission over time reveals

long term stability (i.e. no blinking, no bleaching), but also spectral jitter occurring at longer time scales (> ~1sec) (Sec. 5.7). Both types of spectral fluctuations draw attention to the environment as a possible source of noise requiring further future consideration.

Due to anisotropic confinement, neutral excitons with relatively large fine-structure splitting (~0.7 meV) were observed (Sec. 5.4), as confirmed by polarisation measurements (Sec. 5.5) and magneto-optics (Sec. 5.6). An initial characterisation of the phonon sideband (Sec. 5.4) found it constitutes a significant part (~40%) of the total emission. A step towards understanding the SQE's interactions with phonons was made via temperature dependant PL (Sec. 5.9). Further, via polarisation and magnetic field measurements (Sec. 5.5-6), features such as unequal intensities and non-orthogonal phases of the FSS doublets and relatively large (~8) g factors were uncovered. Finally, the statistics of emitter emission energy exposed an inhomogeneous distribution spreading over a wide range (Sec. 5.8) due to relatively large variations in quantum confinement.

In Chapter 6, the first observation of quantum-dot like localised emissions from monolayer $MoSe_2$ was reported. A direct comparison between $MoSe_2$ and WSe_2 emitters was made. Although $MoSe_2$ emitters show similarities such as the impact of stain on emitter localisation, there are many differences that include poor stability in time and energy, and poor spectral isolation of emitters. Further, successfully demonstrating antibunching to confirm single photon emission remains a challenge to tackle. The negative antibunching results thus far encourages further investigation and raises important questions. Does the band alignment of the host (i.e. type I of $MoSe_2$, type II of WSe_2) have a crucial impact on single photon emission? And, what is the influence of dielectric screening in inducing emitters? The results show that $MoSe_2$ is a distinct and intriguing system to explore single photon emission and more broadly light-matter interactions.

The next section will explore possible explanations for the origin of the SQEs investigated in this thesis.

7.2 A broad discussion on the nature of emitters hosted by 2D semiconductors.

Since the early 1960s, the demonstration of quantum confinement of charge carriers became reliably reproducible thanks to epitaxially-grown GaAs-GaAlAs quantum wells (QW). This stimulated work to constrain additional degrees of freedoms and create one (quantum wires) and zero (quantum dots) dimensional systems. The progress of

introducing lateral confinements in a QW is described in reviews by Petroff[*5*] and Yoffe[*6*]. The knowledge of creating lateral confinement in these 2D systems is a valuable and relevant resource when trying to understand the physical origin of localised excitons hosted by 2D TMDs.

Although a range of schemes including local electrostatic and magnetic fields or self-assembly of epitaxial QDs to reduce the confinement and create a zero dimensional system are mentioned in the reviews, this chapter will focus on local strain engineering, atomic defects, and local fluctuations (disorder) as potential reasons for 3D confinement. Regardless of the approach, constructing a 0D system poses technological difficulties due the dimension requirement for the confining potential: it must be comparable with the Bohr radius of the particle under consideration. In monolayer TMDs, the Bohr radius of an exciton is on the order of a nm [*7*]. Further, it is compelling to search for the origin of exciton localisation in TMD monolayers after more than 50 years since thin TMDs (~40 nm MoS_2 [*8*] and ~1.3 nm, single unit cell of WSe_2 [*9*]) were observed to show a distinct excitonic absorption spectrum - a fingerprint of 2D delocalised excitons.

7.2.1 Nanopillar-strain-induced or strain-defined?

Creating quantum confinement via nanoscale strain engineering has been pursued in bulk semiconductors. There, local elastic strain was able to laterally confine carriers in quantum wells[*10-12*] and wires[*13*]. However, the strain-driven quantum confinement failed to isolate the carriers from harmful surface states. This was due to low elasticity of the host material and small vertical strain propagation distances as the structures were embedded inside the bulk[*14*]. Two-dimensional semiconductors with high elasticity[*15*] and direct access offer renewed opportunities to pursue nanoscale strain engineering of three-dimensional quantum confinement, one such example is array of quantum emitters presented in Chapter 4.

Figure 7.2.1a shows a sketch of the approach. Thanks to attractive van der Walls forces the flake conforms to the substrate's topography inducing elastic point-like strain at a nanopillar location[*16, 17*]. The biaxial strain, created at top the nanopillar, modulates locally the band-gap producing a new artificial potential landscape for the 2D excitons, now with a local minimum as shown in the Figure 7.2.1b. Owing to the funnelling effect, photogenerated excitons travel from unstrained regions with larger band-gap towards strained regions with smaller bandgap [*17-19*]. To accommodate for the presence of localised excitons and make the connection with strain-induced emitters (see orange spectrum in Figure 7.2.1c), Figure 7.2.1b also features a high density of randomly

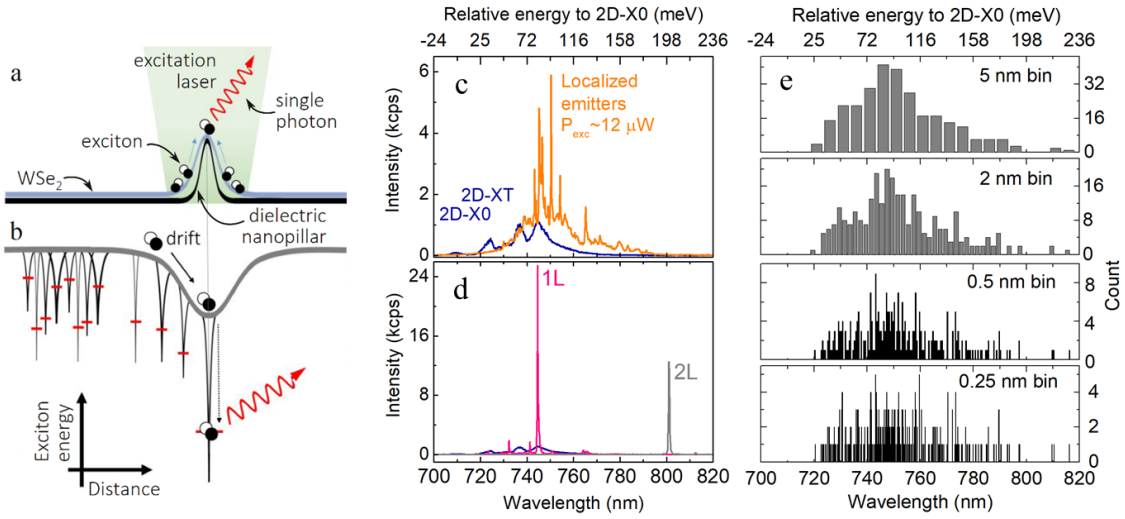

Figure 7.2.1 – **(a)** Deformed by a pillar, a layer of WSe_2 is subjected to a point-like elastic strain perturbation. **(b)** WSe_2 band-gap locally modulated by strain. Randomly distributed localized excitons with high density seen as traps with quantised energy levels. Photogenerated excitons funnel to an individual trap at the nanopillar centre creating a single highly efficient quantum emitter. **(c)** PL spectra from (un)strained region in (blue) orange showing (smooth) sharp PL emission peaks. **(d)** PL spectra of successful strain-induced post-selection of SQEs in mono(bi)layer WSe_2, as illustrated in **a** and **b**. **(e)** Emission energy histogram of strain-induced SQEs in 1L WSe_2 with 4 different bin sizes. All data from type (iv) sample (see Chapter 5).

distributed sharp perturbations which are seen as exciton traps with quantized energy levels. Their origin is the subject of this discussion. The sketch assumes that the localised excitons overlap spatially and spectrally in unstrained regions where exciton traps cannot be distinguished. This is to explain the fact that PL emission at longer wavelength than 2D-XT (see blue spectrum in Figure 7.2.1c,h), from unstrained regions, in all characterised flakes remains homogenous over entire flake's area (i.e. 25×100 μm) showing only little spatial fluctuations. This part of PL emission shows broad peaks at consistent energies regardless of crystal supplier or substrate (see appendix A), suggesting they are global features of the material. Nevertheless, a single quantum emitter can be isolated and 'post-selected' with the appropriate nanopillar dimensions and localized exciton density. In such case, an individual quantum emitter hosted by mono- or bi-layer WSe_2 will dominate the PL spectrum at low temperatures and low excitation power due to the efficient funnelling to the strained site (see Figure 7.2.1d).

At this stage one could ask: why local is the strain modulation induced by the nanopillar not sufficient to create quantized state so the description given above uses random perturbations to explain the 0D confinement. The evidence is presented in the following paragraphs.

Figure 7.2.1e displays the number of strained-induced emitters emitting at certain energies (from sample type (iv), data set from Ch.4). This statistic provides an insight to inhomogeneous distribution and density of emitters in ML WSe_2. Figure 7.2.1e displays relatively large range of confinement fluctuations (~200 meV). The local strain apparently then tunes the confinement of SQEs. The estimated amount of applied strain is much smaller (see Chapter 4 Figure 4.3.7) than this tuning range. This is the first indication that SQEs might stem from other sources than nanopillar-strain-induced local minima. However, at certain locations strain is greater than measured value due to averaging over a large spot size. Figure 7.2.1e also shows the same energy distribution with 4 different binning sizes (5, 2, 0.5 and 0.25 nm), revealing that as the binning size is reduced, the shape of distribution is conserved. The 0.25 nm binning size remains continuous, indicate a high density of exciton traps potentials. Such density can be associated with the random nature of mechanism that creates the confinement (i.e. random disorder). On contrary, if solely point defects or point-like strain field were trapping excitons, one could expect emission energies clustered at similar energies (unless also tuned broadly by strain), which is not the case. Perhaps, one could see clustered emission energies after post-selecting the statistics for nanopillars aspect ratio.

Figure 7.2.2a displays the energy histograms of emitters from different nanopillar aspect ratios (the row number, see Chapter 4, Fig. 4.3.6). Notably, nanopillars with higher aspect ratio led to a higher number of emitters (shown by color-coded dots in wavelength-dependent accumulations, where Row 2 has the lowest, Row 5 has the highest aspect ratio). Further, the Row number does not break the histogram continuity and does not favour a certain energy. If these nanopillars were able to trap excitons, one should observe common emission energies which are characteristic for each strain-created confinement. Instead, a progressive trend can be noticed. The number of emitters at higher wavelengths increases with increasing Row number. While Row 2 emitters occur and spread around 750 nm ($\Delta E_{2D\text{-}X0}$ ~95 meV) from which they evenly decay, Row 5 displays the biggest proportion of emitters emitting beyond 760 nm ($\Delta E_{2D\text{-}X0}$ ~115 meV). This is consistent with the increase of strain induced by each nanopillar type (see Chapter 4 for details) suggesting that local strain created by the nanopillar tunes the bandgap.

To further confirm the role of nanopillars in tuning SQEs, Figure 7.2.2b displays the accumulative wavelength-dependent emission statistics of all emitters (from Figure 7.2.1e, in black line) and emitters meeting post-selection Row criteria, as shown Figure 7.2.2a. When normalised, regardless to the post selected category, all lines follow a

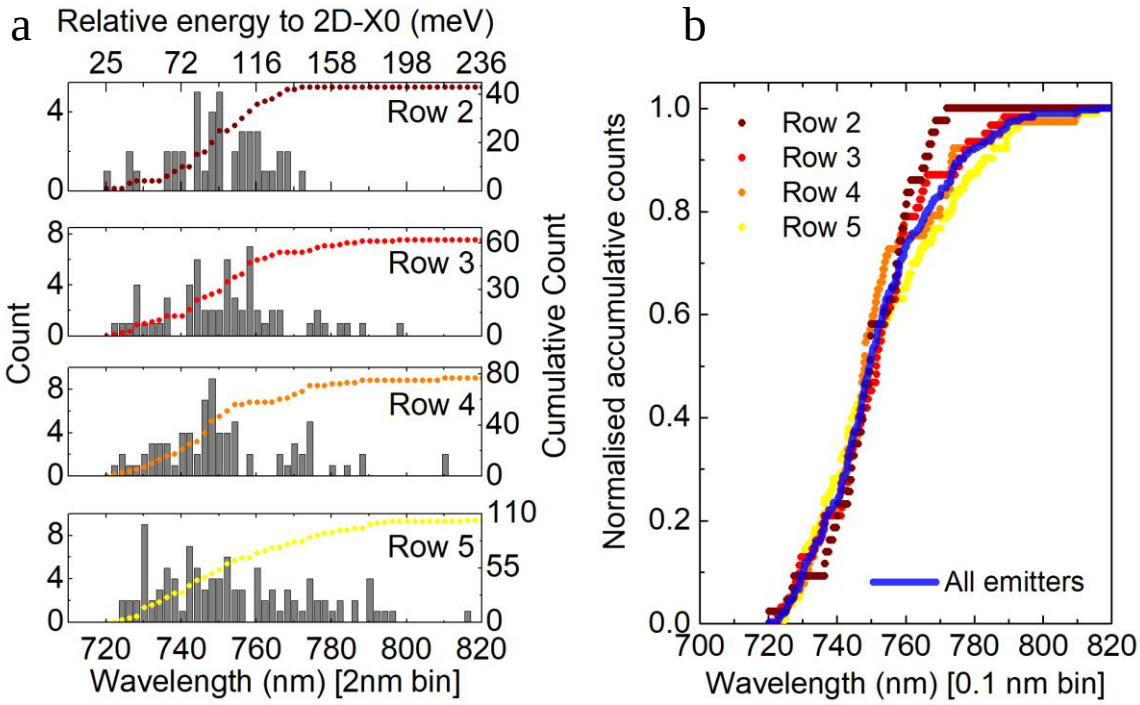

Figure 7.2.2 – **(a)** Post-selected emission energy histogram for nanopillar Row number / aspect ratio (where Row 2 has low and Row 5 has high aspect ratio (see Ch.4, Fig. 4.3.6)). **(b)** Normalised wavelength-dependent accumulations of post-selected emission energies categorised by Row number / aspect ratio and peak intensity. All data from type (iv) sample (see Ch. 4).

similar trend. These similarities indicate that there is an underlying and common density of quantised states in the material which is independent of the nanopillar.

There are two obvious choices which could explain the quantisation: atomic defects or local disorder.

7.2.2 Atomic defects

Atomic point defects are legitimate candidates to account for the quantum emissions seen in layered WSe_2, but their identification remains a challenging task because it is hindered by a high density of quantum states and its wide inhomogeneous distribution, as shown in Figure 7.2.1e. The example of the contrary is multi-layered hBN, where SQEs were observed and quickly identified as colour centres[*20-22*]. One could interpret this discrepancy as a hint that WSe_2 SQEs might arise from local disorder instead. On the other hand, scanning tunnelling microscopy (STM) finds high concentrations and high variety of defects in atomically thin TMDs, which is expected from calculations to create localised states within the bandgap[*23, 24*] (100-400 meV below depending on 2D material and the type of defect). For example, in mechanically exfoliated MoS_2 monolayers, the density of dominant defects (S vacancies with one (V_S) or two (V_{S2}) S atoms absent) were measured to be around 0.13 nm^{-2} [*25*] (~1 million per collection spot

of 0.5 μm). It was demonstrated that irradiation with MeV α particles and thermal annealing at sub-decomposition temperatures activates a new emission in PL spectrum ~100 meV below the optical bandgap, shown in Figure 7.2.3, which was assigned to the increase of dichalcogenide vacancies which were interacting with inert atmosphere (i.e. Nitrogen, Oxygen)[*23*]. When compared with the histogram (see Figure 7.2.3), the PL peak coincides with the tail of the inhomogeneous distribution. This might hint that at around these lower wavelengths, quantum emission arises from point defects. However, direct correlation between point defect sites and the single quantum emission is to be demonstrated. The FSS commonly observed in WSe_2 emitters does not necessarily exclude point defects as the cause for exciton trapping as some defects in other bulk materials exhibit FSS [*26*]. However, it is hard to justify such high density and wide inhomogeneous broadening of quantum states with possible configurations of atomic point defects.

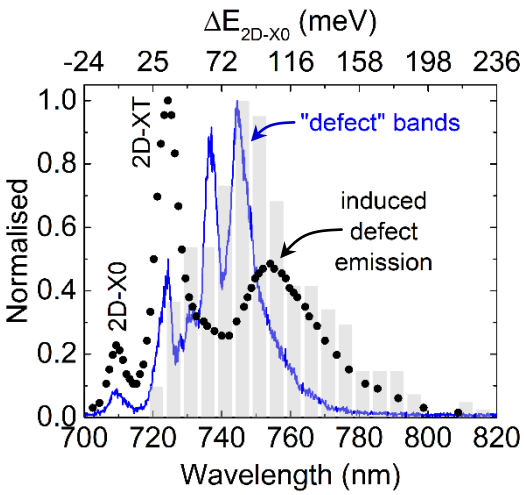

Figure 7.2.3 – Same as Figure 7.2.2, only with additional spectrum of induced defect PL emission (black dots), taken from [29], which matches the tail at longer wavelength of the histogram (gray columns). The wavelength of new dotted spectrum has been adjusted to the emission of 2D-X0 of blue spectrum.

7.2.3 Local disorder and band alignment near type I - type II crossover

There is a strong resemblance between the optical spectrum of SQEs in WSe_2 and so-called fluctuation quantum dots formed by monolayer fluctuations in the thickness of GaAs quantum wells at the AlAs barrier interface [*27-30*]. To illustrate this comparison, I reproduce the results from A. Zrenner *et al.* [*27*] (See Figure 7.2.4).

The band diagram of the active region of the QW system is shown in the inset of Figure 7.2.4a, the conduction band states E_0^{Γ} (E_0^{X}) originate from the GaAs QW (AlAs X-band) and facilitate a direct (indirect) transition with the valence band state HH_0. The relative energies of E_0^{Γ} and E_0^{X} can be tuned smoothly with electric field (V_B) such that the indirect E_0^{X} can be set to be the ground state. In this configuration, the PL spectrum exhibits two broad and smooth peaks, as shown in Figure 7.2.4b, but it develops sharp spectral lines at E_0^{X} when the collection spot diameter is reduced (see Figure 7.2.4c). This demonstrates that the PL of E_0^{X} is comprised of a high density of localised excitons with distinct spectra at different spatial positions. The discrete peaks arise from random

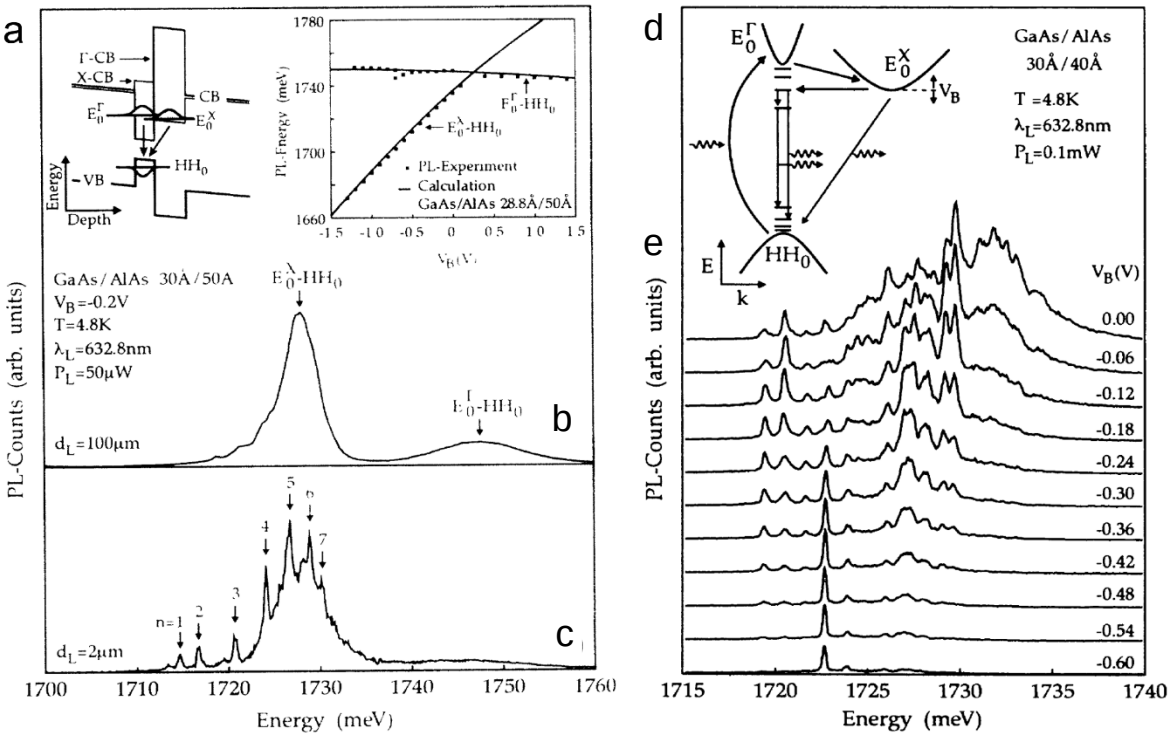

Figure 7.2.4 – **(a)** Schematic band diagram of the coupled double QW structure showing (in)direct (Γ) X band and its tuning capabilities, where each band can become the ground state at certain value of external electric field. **(b)** PL spectrum of QW structure in the indirect regime, where experimental parameters are listed on the left. **(c)** same as **b** but with higher spatial resolution (d_L = 2 μm). **(d)** Diagram of relaxation and recombination process. (e) Evolution of PL response as a function of V_B, where at the lowest bias only a single line with the deepest confinement remains visible. All figures were adapted from [27].

thickness fluctuations along the AlAs/GaAs QW interface creating a range of discrete states inside the nominal GaAs bandgap. Physically, localised width variations of 2 monolayers corresponds a 48 meV shift in energy). Quoting the authors: "*It can be further shown that a 100 nm wide Gaussian-shaped potential well with a depth of about 20 meV has an almost similar level spectrum as the one shown in"[27]*.

Figure 7.2.4d shows schematic of the process. Here electrons are excited from HH_0 to E_0^{Γ}. The electrons then scatter to find a global minimum which under a negative applied bias is in indirect momentum-dark E_0^{X} band. Due to the indirect nature of the E_0^{Γ}-HH_0 excitons, they have a long lifetime and a large carrier population can build-up over time. At select applied bias, carrier hopping from E_0^{X} to quantised states in E_0^{Γ} can occur. Deeply confined emitter can then be uncovered by varying the applied bias (see Figure 7.2.4e). The observation of localised emitters arising from local disorder in QWs was repeatedly reported [*28-30*]. In addition to local disorder, the radiative lifetimes of competing emissions (i.e. E_0^{Γ}, E_0^{X}, localised) and small energetic distance between E_0^{Γ} and E_0^{X} (near the type-I to type-II crossover) are key requirements in observing quantised

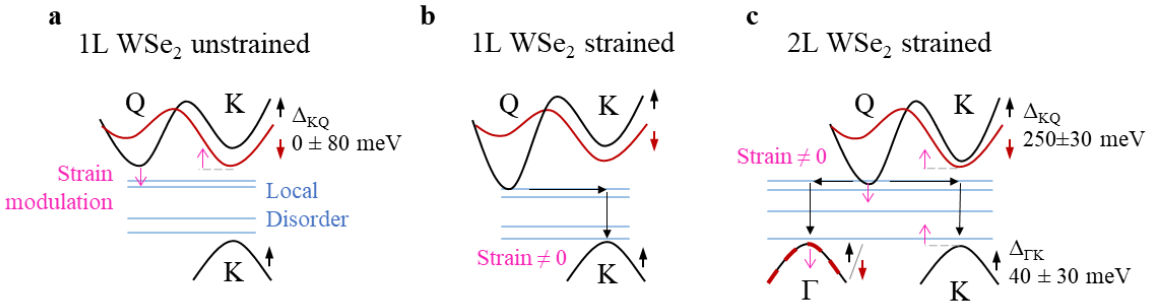

Figure 7.2.5 –Schematics band diagram of **(a)** unstrained 1L WSe_2 **(b)** strained 1L WSe_2, and **(c)** strained 2L WSe_2, showing relaxation and recombination process of SQEs. Figures feature Q, K and Γ valleys with color-coded spin character: spin up (down) is marked black (red), crucial in optical selection rules to recognise spin-dark/bright transitions. Localised exciton states arising from local disorder are located inside the optical bandgap and marked in blue. The directions of band strain modulation are noted with pink arrow. Thin and black arrows in **b** and **c** point recombination steps of the PL process.

light in these structures [*30*]. These conditions imply that the large portion of the carrier population is contained in momentum-dark, where excitons have the longest radiative lifetime. When the system is disturbed by a local disorder, electrons hop from a highly populated and long-lived pool of E_0^{Γ} states to localised states with much faster radiative recombination. If the relation: $\tau\_E_0^{\Gamma} >> \tau\_localised >> \tau\_hopping$ is satisfied, the emission from localised states dominates PL.

Now, to make the connection to mono- and bi-layer WSe_2, the first step is to recall their band structure (see Figure 1.4.2). In the conduction band (CB), calculated values of K-Q energy separation (ΔE_{CB_KQ}) for ML WSe_2 are on the order of several tens of meV [*31, 32*] while the experimental evidence [*33*] support this (within the experimental error ± 80 meV), as shown in Figure 7.2.5a. Note that the valence band at Q point is not considered because it significantly low in energy. In BL WSe_2 the situation is different because in the CB the ΔE_{CB_KQ} increases to 250 ± 30 meV [*33*] (measured value) making the band at Q the global minimum, while in the valence band (VB) K and Γ become almost degenerate ($\Delta E_{VB\_K\Gamma}$ = 40 ± 30 meV obtained from angle-resolved spectroscopy) [*34*], as illustrated in Figure 7.2.5c. Notably, the direct (indirect) character of excitons formed from electrons in the CB at K (Q) point in mono- and bi-layer WSe_2 is analogous to excitons involving electrons in E_0^{Γ} (E_0^{X}) states in the AlAs/GaAs QW structure. Also in mono- and bi-layer WSe_2, a large proportion of carrier population is contained in momentum-dark Q valley where excitons are expected to have long lifetimes. Therefore, I suggest the following interpretation for the origin of SQEs and their behaviour in WSe_2. It involves strain (i.e. of a nanopillar) shifting the Q (K) valley downwards (upwards)[*35*] to approximately match the energy of discrete states of localised excitons at lower

energies than the nominal bandgap arising from local disorder. This condition allows excitons to effectively hop and recombine at these sites. It is safe to assume that the hopping happens much faster than the recombination (few ns) and that carriers in Q valley are long enough lived to provide a sufficiently large population. Further, perhaps aided by strain-induced funnelling effect, a large pool of carriers in the Q valley could travel large distances in real space towards localised exciton sites with matching energy.

The recombination process does not differ between mono- and bi-layer WSe_2 apart from the fact that bilayer has additional Γ valley which might take active part in the final recombination. Note that in the bilayer, ΔE_{CB_KQ} is larger than in monolayer, placing the bilayer further away from type-I / type-II crossover, deeper into type-II regime were density of states is likely to be lower than near the optical bandgap. This might explain a difference (2 times) in inhomogeneous broadening observed in the emission energy histograms of mono- and bi-layer (see Figure 4.6.1).

Recently, an effort to understand the connection between momentum-indirect bands and the origin of quantum emitters in bilayer WSe_2 has been made[*36*]. There, statistics of the emission energy exhibited a sharp edge (at high energy) coinciding with the expected energy of $\Delta E_{Q\Gamma}$. A similar edge is also observed in 2L WSe_2 emission histogram (see Figure 4.6.1b), strengthening the interpretation that the momentum-dark bands are important ingredient in SQE recombination.

In stark contrast to WSe_2, the lowest energy transition of monolayer $MoSe_2$ is spin-allowed, creating a bright exciton with a fast lifetime due to the selection rules [*37*].Further, in $MoSe_2$ the Q valley is energetically far from the K and K' points, where the global minima are situated (type-I band alignment) [*38*]. Therefore, unlike monolayer WSe_2, the electronic dispersion of monolayer $MoSe_2$ does not facilitate a large population of indirect (momentum) excitons composed of long-lived carriers that can subsequently scatter into lower energy quantum confined states. Instead, in $MoSe_2$ the excitons recombine effectively via transitions at the K valleys. Note that in $MoSe_2$ and WSe_2, spin-allowed delocalised 2D excitons recombining at K valley have the a lifetime of ~ 2ps [*39*]. Hence, the proposed carrier relaxation and recombination scheme for WSe_2 is unlikely to be compatible with $MoSe_2$, providing a possible explanation as to why an observation of antibunching from $MoSe_2$ quantum emitters has proven elusive thus far [*3*, *40*].

Regardless of the carrier dynamics, the precise origin of the local disorder is still unknown in this scenario. While the local disorder in fluctuation quantum dots is caused by quantum well width fluctuations are width fluctuations, in few layer WSe_2 there are several possible causes which could create local disorder, including inhomogeneity in the dielectric screening, strain, or charge environment.

Dielectric screening is a powerful tuning parameter of intrinsic material properties as described in introduction Chapter 1, Section 1.4.5. In 2D TMDs screening effects are so strong that 2D excitons energy series deviates significantly from hydrogen Rydberg series[*41*]. Further, altering the dielectric environment alters the optical bandgap: a shift of few hundred meV has been observed [*42*]. It was also calculated that very small (~0.5 nm) air gaps between flake-substrate interfaces can enhance this change even further[*43*]. Recalling the fabrication process of 2D monolayers (that involves 'scotch-tape' exfoliation technique, polymer-based deterministic transfer, and solvent-cleaned substrates) which might introduce contamination, inhomogeneity in the dielectric screening is suited to explain disorder in WSe_2 flakes.

Local strain in a form of corrugation on the surface is a common feature of the topography of 2D-flakes, as can be observed with AFM (see Fig. 3.3.3) and SEM (see Fig. 4.3.3b). These corrugations (i.e. nanobubbles, folds, or wrinkles) have been shown to be correlated with localised emission [*1*, *44*]. Strain is able to modulate the bandgap up to hundred meV/% of biaxial strain (i.e. in 1L WSe_2, A peak shift = -66 meV/%[*45*]) which is large enough to create confinement if localised suitably. It might occur that larger scale which strain perturbations induce the exciton funnelling effect while more localised strain induces quantum confinement. Perhaps, strain can do both and a way to distinguish the crossover is the Bohr radius of the 2D exciton (~1 nm). Additionally, structural or bubbles expand vertically above the substrate surface leading to a changing dielectric environment, perhaps combining with strain to positively contribute to the overall confinement potential. All topography types are the outcome of polymer-based transfer and the roughness of the substrate. To reduce flake roughness, few-layer hBN is commonly used as a substrate [*46-49*], but with excess of pressure during the transfer nanobubbles still can form even on atomically smooth hBN (see suppl. inf. of [*50*]). Another approach is to transfer flakes with polymer at increased temperature which prevents formation of corrugated surfaces (i.e. nanobubbles and wrinkles) leading to surface roughness < 1nm [*44*]. It was also shown that this 'hot' transfer reduces PL with sharp comb-like emission to just few smooth peaks[*44*].

Electrostatic gates defined in quantum wells can lead to lateral quantum confinement with a high degree of tunability, enabling near ideal quantum dots with Coulomb blockade for single spin investigations (see [*51*] for an overview; see [*52*] (currently in press at Nature Nanotechnology) for 2D materials implementation). It is therefore natural to ask if electronic charge disorder might be a cause of exciton localization. Electronic charge disorder is a well-known mechanism to limit carrier mobilities in graphene [*53*]. Sub-micron charge 'puddles' often result from contaminants present between interfaces, a primary motivator for encapsulating graphene in h-BN with ultra-clean interfaces [*54*]. In general, quantum dots defined in two-dimensional electron gasses with a large Fermi wavelength (e.g. in MBE grown III-V structures) need to be sub-micron scale, but not exceptionally small. On the other hand, for exciton localization we expect nm-scale confinement is required, and how small naturally occurring charge puddles might be in the environment of layered WSe_2 remains an open question. If such charge puddles are the cause of exciton localization, one expects that h-BN encapsulation with ultra-clean interfaces should eliminate the localized excitons. So far experimental results are inconclusive in this direction.

7.3 Outlook

This thesis uncovered a facile method to scalably produce quantum emitters in 2D semiconductors and an initial characterisation of several of their intrinsic properties. However, much work remains to fully understand their properties and to potentially exploit them for future technologies. Based on the insights presented in this thesis and up-to-date literature, this section will present ideas and directions for further development.

To confirm the hypothesis that the broad 'defect' band is made of an ensemble of highly overlapping SQEs, one could reduce the area of collection far below the diffraction limit of the optical system (< 0.5 μm) with nanofabricated masks. As shown in [*27, 55*], if the hypothesis is correct, sharp spectral lines will emerge from the broad 'defect' peak. If PL emission only decreases in intensity, it comes from 2D delocalised excitons. The mask could consist of two layers. The first layer should be made of a thin but uniform transparent dielectric (i.e. SiO_2, Al_2O_3) to ensure a constant dielectric environment for the 2D crystal everywhere. The second layer, which contains nanosize pinholes, should be made of an opaque material (e.g. sufficiently thick metal).

If crystal defects cause TMD SQEs, approaches stemming from chemistry should be of a great resource to identify their origin. To 'repair' already exfoliated monolayers or bulk

crystal, one could anneal them and place them in a chalcogenide atmosphere to minimise the amount of point defects. Correlating defects in scanning tunnelling microscopy (STM) or transmission electron microscopy (TEM) and quantum emitters in PL would be a conclusive proof of their origin. To achieve this, the defect density typically found in STM or TEM measurements of 2D crystal would need to be reduced considerably.

Regardless of the SQE origin, neighbouring point defects can be a source of charge noise and general instability of the system, which is likely to negatively affect the optical qualities of emitters (i.e. its coherence and spectral jitter). Therefore, reducing their density is generally a good approach. For instance, it has been demonstrated that a superacid treatment significantly improves PL quantum yield of S-based TMD monolayers [*56*, *57*], but the analogous treatment for Se-based 2D materials is still to be discovered. This confirms that the surface chemistry is an important aspect which could benefit from further investigation.

Immediate opportunities rely on improving the device quality. Apart from improved quality of the 'mother' crystal, improved devices could also result from enhanced cleanliness of the heterostructure assembly process. Improving the assembly process involves two aspects. First, using an inert environment avoids interactions between the flake surface and the atmosphere (i.e. in a glove-box filled with Argon atmosphere [*58*], and perhaps even an ultra-high vacuum [*59*] is best). Second, the technique with which heterostructures are assembled plays a critical role to fabricate ultraclean samples (see the review [*60*]). Therefore, the current all-dry transfer procedure, introduced in Chapter 3, needs to be adapted to allow for hot pick and place scheme [*61*] which causes less contamination, as only the top most flake is in contact with a contaminating polymer.

Encapsulation combined with annealing has shown to improve the linewidth towards homogenous limit of 2D excitons in all 4 highly studied TMDs [*46-49*]. It is expected to do same for SQEs. It has been demonstrated that encapsulation and annealing force interface contaminants to migrate and aggregate in clusters, resulting in large regions of pristine quality [*62*]. Therefore, the impact of annealing and hBN encapsulation on PL emission of 'defect' peaks and SQEs is an exciting aspect to investigate.

Another approach is to use external means to reinforce a clean environment such as a charge tunable device. By pining the Fermi level and applying external an electric field across the sample, the device controls the charge carrier concentration and might deplete residual charge noise. This would lead to reduced charge noise translates into reduced

spectral jitter. Further, having the capacity of charge tenability and Coulomb blockade would pave the way to clean spectroscopy that is needed to perform other experiments. For instance, the charging behaviour of isolated SQE would certainly help in distinguishing its charge species which for now are elusive (with exception of neutral exciton[*1*] and biexciton [*63*]) and open the door into spin and valley investigations.

Once 2D flakes poses a pristine quality, measurements like resonance fluorescence and two-photon interference should become experimentally accessible. Both can measure the SQE coherence, the former by observing the Rabi oscillations and the latter via Hong-Ou Mandel interference visibility.

Assuming TMD SQEs are caused by local disorder, obtaining ultra-clean (disorder-free) pristine devices would open the door to creating artificial confinement (via electrostatic gating or nanoscale dielectric or strain engineering). These new types of QDs would be externally induced and controlled, so they could have very different properties to those investigated in the thesis.

Finally, deterministic strain-induced localisation of SQEs in 2D semiconductor platform which can be transferred easily offering instant integration of SQEs into any custom architecture, a unique advantage over quantum emitters in bulk materials. Once found and characterised, emitters embedded in bulk materials require nanofabrication process to be performed around them, whereas WSe_2 TMDs can be induced in custom-built devices with deterministic polymer transfer. Integration into waveguides and cavities should be a straightforward step, opening the door to cavity quantum electrodynamics and on-chip quantum photonics. Subsequent work on GaSe [*64, 65*] and hBN [*22, 66*] are the examples of these capabilities, showing applicability and universality of local strain engineering in 2D quantum photonic platform. (In GaSe, strain-induced emitter localisation was observed [*64*] and emitter coupling to waveguide mode was demonstrated[*65*]. In hBN, emitter strain tuning[*22*] and emitter array[*66*] were achieved).

7.4 Summary

In this chapter, the first section described the novelty of the thesis, which is based on 4 published papers [*1-4*] with additional in-depth emphasis on the fabrication process of 2D monolayers.

The next section provided a broad discussion about the origin of SQEs. Although the discussion does not conclusively exclude competing interpretations (i.e. point defects,

local strain, and local disorder), it presented carrier hopping from the momentum-dark Q valley to localised excitons arising from local disorder as a plausible mechanism of the recombination process in WSe_2 SQEs. Similarities with previously studied QW systems (i.e. band alignment at near type-I type-II crossover; an indirect exciton at the lowest energy creates a large population of long-lived carriers; PL spectra with a high density of localised quantum emitters; an exponential tail in PL at longer wavelengths; and the timescale relationship: $\tau_Q > \tau_{localised} > \tau_{hopping}$ is satisfied).

In the final section, I presented just a fraction of possible directions and exciting vistas for exploration. Single quantum emitters in 2D crystals are full of potential to become a successful quantum photonic platform, and the journey has just begun.

7.5 References

1. S. Kumar, A. Kaczmarczyk, B. D. Gerardot, Strain-Induced Spatial and Spectral Isolation of Quantum Emitters in Mono- and Bilayer WSe2. *Nano Letters* **15**, 7567-7573 (2015).

2. S. Kumar *et al.*, Resonant laser spectroscopy of localized excitons in monolayer WSe2. *Optica* **3**, 882-886 (2016).

3. A. Branny *et al.*, Discrete quantum dot like emitters in monolayer MoSe2: Spatial mapping, magneto-optics, and charge tuning. *Applied Physics Letters* **108**, 142101 (2016).

4. A. Branny, S. Kumar, R. Proux, B. D. Gerardot, Deterministic strain-induced arrays of quantum emitters in a two-dimensional semiconductor. *Nature Communications* **8**, 15053 (2017).

5. P. M. Petroff, in *Physics of Quantum Electron Devices*, F. Capasso, Ed. (Springer Berlin Heidelberg, Berlin, Heidelberg, 1990), pp. 353-366.

6. A. D. Yoffe, Low-dimensional systems: Quantum size effects and electronic properties of semiconductor microcrystallites (zero-dimensional systems) and some quasi-two-dimensional systems. *Advances in Physics* **51**, 799-890 (2002).

7. G. Moody *et al.*, Intrinsic homogeneous linewidth and broadening mechanisms of excitons in monolayer transition metal dichalcogenides. *Nature Communications* **6**, 8315 (2015).

8. B. L. Evans, P. A. Young, Delocalized excitons in thin anisotropic crystals. *physica status solidi (b)* **25**, 417-425 (1968).

9. F. Consadori, R. F. Frindt, Crystal Size Effects on the Exciton Absorption Spectrum of WSe2. *Physical Review B* **2**, 4893-4896 (1970).

10. K. Kash *et al.*, Strain-induced confinement of carriers to quantum wires and dots within an InGaAs-InP quantum well. *Applied Physics Letters* **55**, 681-683 (1989).

11. C. Obermüller *et al.*, Pauli-blocking imaging of single strain-induced semiconductor quantum dots. *Applied Physics Letters* **74**, 3200-3202 (1999).

12. F. J. R. Schülein *et al.*, Cascaded exciton emission of an individual strain-induced quantum dot. *Applied Physics Letters* **95**, 083122 (2009).

13. D. Gershoni *et al.*, Optical transitions in quantum wires with strain-induced lateral confinement. *Physical Review Letters* **65**, 1631-1634 (1990).

14. S. Adachi, GaAs, AlAs, and AlxGa1−xAs: Material parameters for use in research and device applications. *Journal of Applied Physics* **58**, R1-R29 (1985).

15. S. Bertolazzi, J. Brivio, A. Kis, Stretching and Breaking of Ultrathin MoS2. *ACS Nano* **5**, 9703-9709 (2011).

16. A. Reserbat-Plantey *et al.*, Strain Superlattices and Macroscale Suspension of Graphene Induced by Corrugated Substrates. *Nano Letters* **14**, 5044-5051 (2014).

17. H. Li *et al.*, Optoelectronic crystal of artificial atoms in strain-textured molybdenum disulphide. **6**, 7381 (2015).

18. J. Feng, X. Qian, C.-W. Huang, J. Li, Strain-engineered artificial atom as a broad-spectrum solar energy funnel. *Nat Photon* **6**, 866-872 (2012).

19. A. Castellanos-Gomez *et al.*, Local Strain Engineering in Atomically Thin MoS2. *Nano Letters* **13**, 5361-5366 (2013).

20. T. T. Tran, K. Bray, M. J. Ford, M. Toth, I. Aharonovich, Quantum emission from hexagonal boron nitride monolayers. *Nat Nano* **11**, 37-41 (2016).

21. A. L. Exarhos, D. A. Hopper, R. R. Grote, A. Alkauskas, L. C. Bassett, Optical Signatures of Quantum Emitters in Suspended Hexagonal Boron Nitride. *ACS Nano* **11**, 3328-3336 (2017).

22. G. Grosso *et al.*, Tunable and high-purity room temperature single-photon emission from atomic defects in hexagonal boron nitride. *Nature Communications* **8**, 705 (2017).

23. S. Tongay *et al.*, Defects activated photoluminescence in two-dimensional semiconductors: interplay between bound, charged, and free excitons. *Scientific Reports* **3**, 2657 (2013).

24. V. Carozo *et al.*, Optical identification of sulfur vacancies: Bound excitons at the edges of monolayer tungsten disulfide. *Science Advances* **3**, (2017).

25. J. Hong *et al.*, Exploring atomic defects in molybdenum disulphide monolayers. **6**, 6293 (2015).

26. D. Simin *et al.*, All-Optical dc Nanotesla Magnetometry Using Silicon Vacancy Fine Structure in Isotopically Purified Silicon Carbide. *Physical Review X* **6**, 031014 (2016).

27. A. Zrenner *et al.*, Quantum dots formed by interface fluctuations in AlAs/GaAs coupled quantum well structures. *Physical Review Letters* **72**, 3382-3385 (1994).

28. D. Gammon, E. S. Snow, B. V. Shanabrook, D. S. Katzer, D. Park, Fine Structure Splitting in the Optical Spectra of Single GaAs Quantum Dots. *Physical Review Letters* **76**, 3005-3008 (1996).

29. W. Langbein, D. Lüer\Sen, H. Kalt, W. Braun, K. Ploog, Anisotropic quantum boxes in corrugated superlattices. *Physical Review B* **53**, 15473-15476 (1996).

30. W. Langbein, H. Kalt, J. M. Hvam, Luminescence dynamics in type-II GaAs/AlAs superlattices near the type-I to type-II crossover. *Physical Review B* **54**, 14589-14594 (1996).

31. Z. Jin, X. Li, J. T. Mullen, K. W. Kim, Intrinsic transport properties of electrons and holes in monolayer transition-metal dichalcogenides. *Physical Review B* **90**, 045422 (2014).

32. K. Andor *et al.*, k · p theory for two-dimensional transition metal dichalcogenide semiconductors. *2D Materials* **2**, 022001 (2015).

33. C. Zhang *et al.*, Probing Critical Point Energies of Transition Metal Dichalcogenides: Surprising Indirect Gap of Single Layer WSe2. *Nano Letters* **15**, 6494-6500 (2015).

34. N. R. Wilson *et al.*, Determination of band offsets, hybridization, and exciton binding in 2D semiconductor heterostructures. *Science Advances* **3**, (2017).

35. S. B. Desai *et al.*, Strain-Induced Indirect to Direct Bandgap Transition in Multilayer WSe2. *Nano Letters* **14**, 4592-4597 (2014).

36. J. Lindlau *et al.*, The role of momentum-dark excitons in the elementary optical response of bilayer WSe2. *ArXiv e-prints*. 2017.

37. G. Wang *et al.*, In-Plane Propagation of Light in Transition Metal Dichalcogenide Monolayers: Optical Selection Rules. *Physical Review Letters* **119**, 047401 (2017).

38. J. S. Ross *et al.*, Electrical control of neutral and charged excitons in a monolayer semiconductor. *Nature Communications* **4**, 1474 (2013).

39. C. Robert *et al.*, Exciton radiative lifetime in transition metal dichalcogenide monolayers. *Physical Review B* **93**, 205423 (2016).

40. C. Chakraborty, K. M. Goodfellow, A. Nick Vamivakas, Localized emission from defects in MoSe2 layers. *Opt. Mater. Express* **6**, 2081-2087 (2016).

41. A. Chernikov *et al.*, Exciton Binding Energy and Nonhydrogenic Rydberg Series in Monolayer WS2. *Physical Review Letters* **113**, 076802 (2014).

42. A. Raja *et al.*, Coulomb engineering of the bandgap and excitons in two-dimensional materials. **8**, 15251 (2017).

43. M. Florian *et al.*, The dielectric impact of layer distances on exciton and trion binding energies in van der Waals heterostructures. *ArXiv e-prints*. 2017.

44. D. S. Gabriella *et al.*, Nanobubble induced formation of quantum emitters in monolayer semiconductors. *2D Materials* **4**, 021019 (2017).

45. R. Frisenda *et al.*, Biaxial strain tuning of the optical properties of single-layer transition metal dichalcogenides. *npj 2D Materials and Applications* **1**, 10 (2017).

46. J. Wierzbowski *et al.*, Direct exciton emission from atomically thin transition metal dichalcogenide heterostructures near the lifetime limit. *Scientific Reports* **7**, 12383 (2017).

47. L. Wang *et al.*, One-Dimensional Electrical Contact to a Two-Dimensional Material. *Science* **342**, 614-617 (2013).

48. F. Cadiz *et al.*, Excitonic Linewidth Approaching the Homogeneous Limit in MoS2-Based van der Waals Heterostructures. *Physical Review X* **7**, 021026 (2017).

49. A. A. Obafunso *et al.*, Approaching the intrinsic photoluminescence linewidth in transition metal dichalcogenide monolayers. *2D Materials* **4**, 031011 (2017).

50. C.-G. Andres *et al.*, Deterministic transfer of two-dimensional materials by all-dry viscoelastic stamping. *2D Materials* **1**, 011002 (2014).

51. R. Hanson, L. P. Kouwenhoven, J. R. Petta, S. Tarucha, L. M. K. Vandersypen, Spins in few-electron quantum dots. *Reviews of Modern Physics* **79**, 1217-1265 (2007).

52. K. Wang, T. Taniguchi, K. Watanabe, P. Kim, Engineering Quantum Confinement in Semiconducting van der Waals Heterostructure. *ArXiv e-prints*. 2016.

53. A. V. Kretinin *et al.*, Electronic Properties of Graphene Encapsulated with Different Two-Dimensional Atomic Crystals. *Nano Letters* **14**, 3270-3276 (2014).

54. F. Pizzocchero *et al.*, The hot pick-up technique for batch assembly of van der Waals heterostructures. **7**, 11894 (2016).

55. J. Cibert *et al.*, Optically detected carrier confinement to one and zero dimension in GaAs quantum well wires and boxes. *Applied Physics Letters* **49**, 1275-1277 (1986).

56. F. Cadiz *et al.*, Well separated trion and neutral excitons on superacid treated MoS2 monolayers. *Applied Physics Letters* **108**, 251106 (2016).

57. H. Kim, D.-H. Lien, M. Amani, J. W. Ager, A. Javey, Highly Stable Near-Unity Photoluminescence Yield in Monolayer MoS2 by Fluoropolymer Encapsulation and Superacid Treatment. *ACS Nano* **11**, 5179-5185 (2017).

58. A. P. Rooney *et al.*, Observing Imperfection in Atomic Interfaces for van der Waals Heterostructures. *Nano Letters* **17**, 5222-5228 (2017).

59. K. Kang *et al.*, Layer-by-layer assembly of two-dimensional materials into wafer-scale heterostructures. *Nature* **550**, 229 (2017).

60. R. Frisenda *et al.*, Recent progress in the assembly of nanodevices and van der Waals heterostructures by deterministic placement of 2D materials. *Chemical Society Reviews* **47**, 53-68 (2018).

61. F. Pizzocchero *et al.*, The hot pick-up technique for batch assembly of van der Waals heterostructures. *Nature Communications* **7**, 11894 (2016).

62. S. J. Haigh *et al.*, Cross-sectional imaging of individual layers and buried interfaces of graphene-based heterostructures and superlattices. *Nature Materials* **11**, 764 (2012).

63. Y.-M. He *et al.*, Cascaded emission of single photons from the biexciton in monolayered WSe2. **7**, 13409 (2016).

64. T. Philipp *et al.*, Single-photon emitters in GaSe. *2D Materials* **4**, 021010 (2017).

65. P. Tonndorf *et al.*, On-Chip Waveguide Coupling of a Layered Semiconductor Single-Photon Source. *Nano Letters* **17**, 5446-5451 (2017).

66. N. V. Proscia *et al.*, Near-deterministic activation of room temperature quantum emitters in hexagonal boron nitride. *ArXiv e-prints*. 2017.

Appendix A PL emission of 'defect' peaks in monolayer WSe_2

The appendix compares PL emissions from monolayers WSe_2 which were derived from bulk materials supplied from different companies. The comparison focuses on the emission energies of so-called 'defect' peaks which appear below 2D-XT and become noticeable under relatively high non-resonant excitation powers on the order of tens of μW. The aim of the comparison is to answer whether defect peak emissions are unique or global feature of the flake.

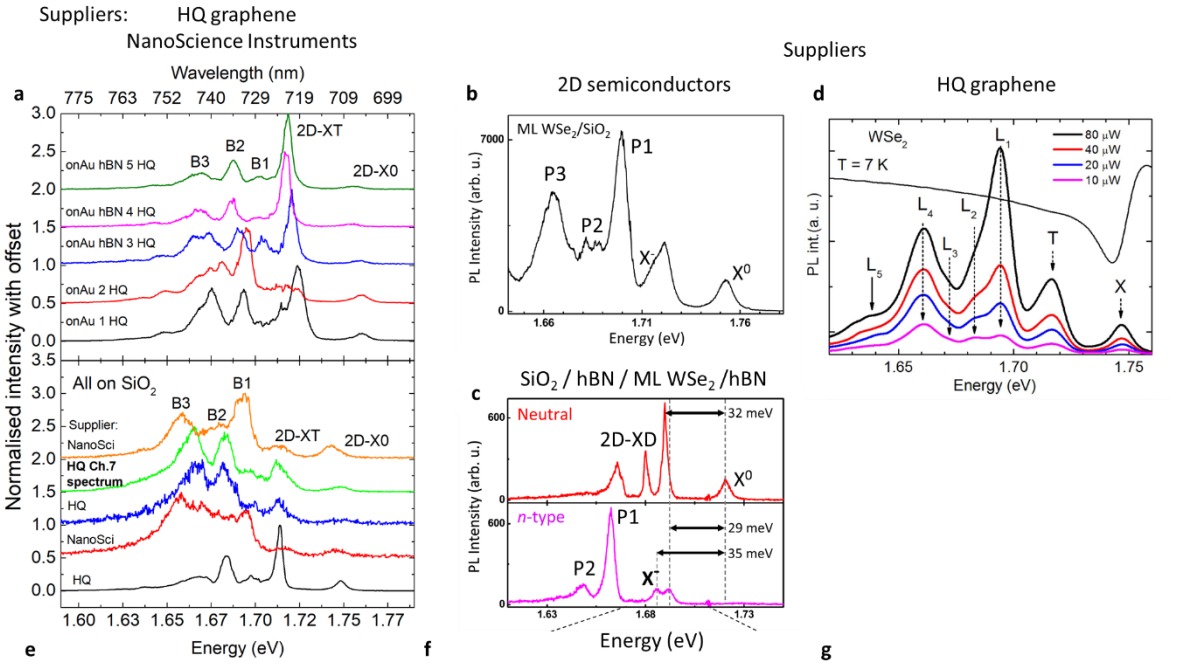

e

On SiO_2	λ (nm)	E (eV)	ΔE 2D-X0 (meV)
2D-X0	709.7	1.747	
2D-XT	723.8	1.713	34
B1	730.5	1.697	50
B2	736.6	1.683	64
B3	745.5	1.663	84
On Au / hBN			
2D-X0	706.1	1.756	
2D-XT	721.8	1.718	38
B1	728.1	1.703	53
B2	734.6	1.688	68
B3	743.4	1.668	88
B4	755.2	1.642	114

f

On SiO_2	λ (nm)	E (eV)	ΔE 2D-X0 (meV)
2D-X0	707.6	1.752	
2D-XT	720.2	1.722	31
P1	729.5	1.700	53
P2	736.3	1.684	68
P3	745.0	1.664	88
On SiO_2 / hBN / WSe_2 / hBN			
2D-X0	720.7	1.720	
2D-XT	733.8	1.690	31
2D-XD	738.2	1.680	41
P1	745.2	1.664	56
P2	752.3	1.648	72

g

On SiO_2	λ (nm)	E (eV)	ΔE 2D-X0 (meV)
2D-X0	710.0	1.746	
2D-XT	722.4	1.716	30
L1	731.9	1.694	52
L2	736.7	1.683	63
L3	741.5	1.672	74
L4	746.6	1.661	86
L5	755.7	1.641	106

Figure 7.6 - Representative PL spectra from monolayer WSe_2 exfoliated from bulk crystal supplied from different companies as labelled above each graph. **(a)** PL of monolayers from HQ graphene and Science Intr. bulk material on SiO_2, gold, and hBN substrates. So-called 'defect' peaks are labelled B1-3 and their energies are listed right below in **e**. **(b,f)** and **(d,g)** same as **a,e** but for monolayers from 2D semiconductors and HQ graphene bulks respectively. Graphs in **b,c** and **d** were adapted from [1] and [2] respectively. **(e-g)** Tables containing emission energies of peaks observed in PL (above) and their relative energy to the 2D-X0 emission revealing matching emissions (color-coded in red, blue and pink).

Figure 7.6 presents PL spectra from monolayer WSe_2 exfoliated from bulk material supplied from 3 companies, including HQ graphene, Science Instruments, and 2D semiconductors. Figure 7.6 also shows spectra from monolayers in different dielectric environment, such as on top of SiO_2, gold or hBN substrates and fully encapsulated in hBN. Both categories are clearly labelled in Figure 7.6. Figure 7.6b,c shows data from [1] and Figure 7.6d from [2]. While Figure 7.6a-d show PL spectra from 2D samples, tables in Figure 7.6e-g display energies of individual peaks (B1-3, P1-3, and L1-5) and their relative energy to 2D-X0 emission, accounting for the bandgap shift due to different dielectric screening. Notably, although relative intensities of peaks vary significantly their energies remain consistent, indifferent to dielectric environment. Further, 3 common bands can be distinguished, at around $\Delta E_{2D\text{-}X0}$ ~55 meV, ~68 meV, and ~88 meV (as color-coded in Figure 7.6e-g). Interestingly, due to full hBN encapsulation (see Figure 7.6c), P3 is absent and the intensity of P2 and P1 can be tuned with electric field.

The comparison confirms that 'defect' PL emission is a global feature of the flake. Interestingly, the emission can be altered by creating a cleaner environment with hBN encapsulation. Although the origin of defect emission requires further investigation, the fact that some defect peaks can be supressed solely with full hBN encapsulation suggests they might originate from local disorder, as discussed in Section 7.2.

A.1 References

1. E. Courtade et al., Charged excitons in monolayer WSe2: Experiment and theory. Physical Review B 96, 085302 (2017).
2. J. Jadczak et al., Probing of free and localized excitons and trions in atomically thin WSe 2 , WS 2 , MoSe 2 and MoS 2 in photoluminescence and reflectivity experiments. Nanotechnology 28, 395702 (2017).